

# **The Silver, Copper and Silicon(110) Surfaces in Ambient Environments**

Thesis submitted in accordance with the requirements of the University of  
Liverpool for the degree of Doctor in Philosophy by

Elizabeth Emily Barritt



Department of Physics

June 2013

# The Silver, Copper and Silicon(110) Surfaces in Ambient Environments

Elizabeth Emily Barritt

## Abstract

The results presented in this thesis were part of a research programme that utilised the surface sensitive technique reflection anisotropy spectroscopy (RAS) to study the silver, copper and silicon (110) surfaces under ambient conditions.

It has been shown that although the preparation of these surfaces can be less precise in ambient conditions, than when prepared in an ultra high vacuum (UHV) environment, the main features observed are similar. The features observed in the RA spectrum for the Si(110) surface in ambient conditions show good agreement with previous data performed in a UHV environment. The experiments performed using the Ag(110) surface show that when the Ag(110) crystal is heated to higher temperatures, when the oxide present will have dissociated off the surface, the ambient RA spectrum shows good agreement with experiments performed in UHV. However, the transition between surface states observed in UHV was not seen in the RA spectrum in ambient conditions. These experiments were performed using the  $Re\left(\frac{\Delta r}{r}\right)$  part of the RA spectra. However, to examine the surfaces further the  $Im\left(\frac{\Delta r}{r}\right)$  part of the RA spectra was also presented along with the azimuthal dependence of the RA spectrum.

The Cu(110) surface was investigated under ambient conditions and electrochemically. It was found the surface is not stable in ambient conditions but can be stabilised electrochemically using HCl. The adsorption and desorption of  $Cl^-$  was studied and the research focused on when the  $Cl^-$  was desorbed from the surface leaving clean Cu(110). Under these conditions the transition between surface states at 2.10 eV in UHV was observed at a slightly higher energy of 2.20 eV in an electrochemical environment.

# Acknowledgements

I would like to begin by thanking Peter Weightman for his constant support and enthusiasm over the past four years. His knowledge of the subject and many areas surrounding it has provided me with a continuous standard to strive to reach and further progress my own knowledge. I would also like to thank Trevor Farrell, his increased support and guidance over the last two years have been vital and without it this thesis would not have been possible. It has been an honour to work alongside many distinguished scientists in our research group, Caroline Smith, Paul Harrison and Andrew Bowfield and also the past and present PhD students, Gareth Holder, James Convery and Tim Craig who have provided friendship and support over many tea breaks!

I would also like to thank my current work colleagues, Caroline Shenton-Taylor, Doug Blackie, Wayne Harrison, Joe Watson and Kelly Vaughan for their support and friendship since I started work.

Finally I would like to thank my friends and family. I would like to thank Naomi Sisson, going through this PhD experience together has proved how vital friendship is and the many long lunches we had will never be forgotten. I would also like to thank Miffy Borland whose stories from CERN brightened up dull Liverpool days! A special thank you goes to Sam and Ben Elliot whose long distance friendship has provided many fun weekends and I am very grateful for your support, although I am much happier we are now all 'southerners' together! I would like to thank Eilish and Noel, Paul and Eileen and Sean and Sarah, for making me feel part of your family, it has been very special having your support from both sides of the Irish Sea. Finally I would like to thank my family, thank you to Steven, Vicky and Sophie who never fail to put a smile on my face. To my Auntie Leslie and Uncle Wilf who have not only supported me during my PhD but for their love and encouragement throughout my life I thank you. A special thank you to Brian, I have been a

nightmare to live with these past few months (years...) but you have been amazing allowing me to go through the motions of thesis writing! I would not have got to this stage without you. To Jonny, I could not have wished for a more supportive brother and to have you back in Liverpool the past year has been a very special experience. Although I think it is your turn to buy the donuts next time! Finally a very special thank you to my mum and dad, there are not enough nice words to say, your continued love is a very special feeling and your encouragement, generosity and support throughout my life has helped me to where I am now.

# Acronyms

ADRAS	Azimuth Dependent Reflection Anisotropy Spectroscopy
AFM	Atomic Force Microscopy
BZ	Brillouin Zone
CD	Circular Dichroism
DVM	Digital Voltmeter
ERS	Electroreflectance Spectroscopy
FCC	Face Centred Cubic
FFT	Fast Fourier Transform
IHP	Inner Helmholtz Plane
IR	Infra-Red
LED	Light Emitting Diode
LEED	Low Energy Electron Diffraction
OHP	Outer Helmholtz Plane
PEM	Photoelastic Modulator
PMT	Photomultiplier Tube
PZC	Potential of Zero Charge
RAS	Reflection Anisotropy Spectroscopy
RDS	Reflection Difference Spectroscopy
SBZ	Surface Brillouin Zone
SCE	Standard Calomel Electrode
SDA	Surface Dielectric Anisotropy
SE	Spectroscopic Ellipsometry
SLFE	Surface Local Field Effect
SPR	Surface Plasmon Resonance
STM	Scanning Tunnelling Microscopy
SXS	Surface X-ray Scattering
UHV	Ultra High Vacuum

UV	Ultra Violet
XPS	X-Ray Photoelectron Spectroscopy
XRD	X-Ray Diffraction

# Contents

## Chapter 1

<b>Introduction</b>	1
1.1 Introduction	2
1.2 Surface Science outside Ultra High Vacuum	3
1.3 Thesis Aims	4
1.4 Thesis Structure	4
1.5 References	6

## Chapter 2

<b>Theory</b>	8
2.1 Crystal Structure	9
2.1.1 The Reciprocal Lattice and Brillouin Zones	10
2.2 Band Structure	11
2.2.1 Free Electron Fermi Gas	12
2.2.2 Electronic Band Structure of Solids	13
2.2.3 Band Structure in Metals	15
2.2.4 Semiconductor Band Structure	16
2.3 Surfaces	17
2.3.1 Surface Phase Transitions	17
2.3.2 Transitions between Surface States	18
2.3.3 Surface Brillouin Zone	19
2.3.4 Optical Response of Surfaces	20
2.3.5 Plasma Frequency	22
2.4 The Three Phase Model	25
2.5 References	27

## Chapter 3

<b>Experimental Set Up</b>	28
3.1 Reflection Anisotropy Spectroscopy	29
3.1.1 The RA Spectrometer and its Components	30
3.2 Propagation of Light through the System	35
3.2.1 Errors	44
3.3 Azimuthal Dependent Reflection Anisotropy Spectroscopy	45

3.4	Electrochemistry	49
3.4.1	Measuring Electrode Potential	52
3.4.2	The Electrochemical Cell	53
3.4.3	Cyclic Voltammetry	54
3.5	Crystal Preparation	55
3.6	Low Energy Electron Diffraction and X-ray Photoelectron Spectroscopy	57
3.6.1	Low Energy Electron Diffraction	58
3.6.2	X-ray Photoelectron Spectroscopy	58
3.7	References	60

## Chapter 4

<b>The Si(110) Surface</b>		63
4.1	Introduction	64
4.2	The Physical Structure of Silicon	64
4.3	The Electronic Structure of Silicon	65
4.3.1	The Electronic Structure of Si(110)	68
4.4	Interband Transitions	69
4.4.1	Temperature Dependence of Interband Transitions	72
4.5	The Reflection Anisotropy Spectroscopy of the Si(110) Surface	76
4.5.1	The $Re\left(\frac{\Delta r}{r}\right)$ part of the RA Spectra as a function of temperature	76
4.5.2	The $Im\left(\frac{\Delta r}{r}\right)$ part of the RA Spectra as a function of temperature	80
4.6	The Complex Anisotropic Surface Dielectric Function of Si(110)	84
4.7	Summary	91
4.8	References	92

## Chapter 5

<b>The Ag(110) Surface</b>	95
5.1 Introduction	96
5.2 Ellingham Diagram for Silver	96
5.3 The Ag(110) Surface	99



5.3.1	The Electronic Structure of the Ag(110) Surface	99
5.3.2	Reflection Anisotropy Spectroscopy of the Ag(110) Surface in UHV	100
5.3.3	The Temperature Dependence of the Ag(110) Surface	103
	The Azimuthal Dependent Reflection	
5.3.4	Anisotropy Spectroscopy of the Ag(110) Surface	104
5.4	The Reflection Anisotropy Spectroscopy of the Ag(110) Surface	109
5.4.1	The $Re\left(\frac{\Delta r}{r}\right)$ part of the RA Spectra	109
5.4.2	The $Re\left(\frac{\Delta r}{r}\right)$ part of the RA Spectra as a function of temperature	111
5.4.3	The $Im\left(\frac{\Delta r}{r}\right)$ part of the RA Spectra as a function of temperature	116
5.5	Azimuthal Dependence of the Ag(110) Surface	120
5.6	Summary	124
5.7	References	126

## Chapter 6

<b>The Cu(110) Surface</b>		128
6.1	Introduction	129
6.2	The Physical Structure of the Cu(110) Surface	129
6.3	The Electronic Structure of Copper	131
6.3.1	The Electronic Structure of the Cu(110) Surface	132
6.4	Reflection Anisotropy Spectroscopy of the Cu(110) Surface	134
6.4.1	Reflection Anisotropy Spectroscopy as a Monitor of Surface States	137
6.5	The Metal/Liquid Interface	141
6.5.1	Surface States at the Metal/Liquid Interface	142
6.5.2	Reflection Anisotropy Spectroscopy of the Metal/Liquid Interface	142
6.6	The Cu(110)/Liquid Interface	143
6.6.1	The Cu(110)/Liquid Interface using H <sub>2</sub> O or	144

	H <sub>2</sub> SO <sub>4</sub> solutions	
6.6.2	The Cu(110)/Liquid Interface using 5 mM H <sub>2</sub> SO <sub>4</sub> + 10 mM KBr solution	146
6.6.3	The Cu(110)/Liquid Interface using 10 mM HCl solution	148
6.6.4	Kinetic Spectra of the Cu(110) Surface using 10 mM HCl solution	154
6.7	Azimuthal Dependence Reflection Anisotropy Spectroscopy of the Cu(110)/HCl Interface	157
6.8	Summary	160
6.9	References	162

## **Chapter 7**

### **Conclusions** 167

7.1	Conclusions	168
7.1.1	Conclusions on Si(110)	168
7.1.2	Conclusions on Ag(110)	169
7.1.3	Conclusions on Cu(110)	170
7.2	Future Work	171

### **Publications** 174

# **Chapter 1**

## **Introduction**

## 1.1 Introduction

For centuries, mankind has pushed the boundaries of science to invent, to discover and to create, some of the most pioneering advancements that are often taken for granted in the 21<sup>st</sup> century. From Galileo's initial understanding of gravity in the late 16<sup>th</sup> century to the discovery of penicillin by Fleming in the 1920's there is an underlying trend spanning throughout the centuries, that of human curiosity. Although many of these advancements have had a huge practical impact on the current world, such as the inventions of the steam engine or telephone, they all begin with an idea, a natural impulse to push the limits of human understanding into the realms of impossibility. The last two centuries provided some of the great industrial advances along with domestic luxuries such as the television, the computer and the electric washing machine, present in almost every home. Moving forward into the current century and the emphasis has been on upgrading, screens with ever increasing definition to give one example. Accessibility of information has also been improved with Ofcom [1] stating that smart phone intake has risen to 39 % in 2012 compared to 27 % in 2011. This high rate of increase in household electronics is a result of electric components, such as transistors, decreasing in size and the research is progressing further to investigate single molecule electronics [2]. However, advancing into this area requires interdisciplinary collaborations which are becoming the norm across all scientific research groups.

The range of tools which scientists use to probe systems have also been increasing at a fast rate, with desktop spectrometers and particle accelerators not only raising the energies at which they can be used but also improving their sensitivity. Furthermore, scientists can now probe biological molecules using some techniques without risk of damaging their structure. Generally to study biological molecules the molecules first need to be adsorbed to a substrate [3,4]. Therefore to correctly identify the molecules' properties it is also vital to have a thorough understanding of the substrate surface. Currently many substrate surfaces have been studied extensively in ultra high vacuum (UHV) environments [5] and only recently has the

Au(110) surface been well understood at the solid/liquid interface [6]. However, it would be useful to have a more complete knowledge of the surface outside a UHV environment and to observe if the surface retains all the same properties outside the UHV chamber.

## **1.2 Surface Science outside Ultra High Vacuum**

The development of surface science, and crystallography in general, increased rapidly through the mid to late 20<sup>th</sup> century [7-9] partly due to the ability to maintain the pressures required inside the UHV chamber at a constant level. This aided the development of many techniques, such as LEED [10], STM [11] and XPS [12], which capitalised on the lack of contaminants present in the chamber by using electrons and x-rays to probe the surface structure of many materials. However, to probe the surfaces in a non-UHV environment other techniques are utilised, in particular those which use photons to probe the surface, which are more suitable to be used in atmosphere. For example, the experimental technique reflection anisotropy spectroscopy (RAS) has been used to study materials in both UHV and non-UHV environments and it also has the ability to study the metal/liquid interface. This, combined with the ability of RAS to monitor changes on the surface, such as when a molecule has been adsorbed, makes it a very useful technique when studying surfaces outside UHV whilst being able to compare results with the same surface studied inside UHV.

When studying clean surfaces in a non-UHV environment their possible oxidation needs to be taken into account. With some surfaces this can be done by heating the surface so the oxide layer dissociates from the surface. However, with others this process needs to be performed electrochemically.

Electrochemistry is a branch of chemistry that has been used successfully alongside traditional physics techniques to further enhance the understanding of the optical response of surfaces [13] in both a UHV environment [14] and in an ambient environment [15]. In particular, the interface between the electrode and

electrolyte is the site of many crucial interactions which will aid both scientific development and industrial research.

### **1.3 Thesis Aims**

The research presented in this thesis will show the results from experiments performed in a non-UHV environment, either in air or at the solid/liquid interface. This thesis uses the Si(110), Ag(110) and Cu(110) surfaces which are all well understood in UHV environments so the RAS results obtained in non-UHV environments can be compared with previous results. Understanding how the surfaces behave in non-UHV environments will further the understanding of surface science research and could aid in the development of practical applications.

### **1.4 Thesis Structure**

This thesis will begin with a brief background discussion on some of the main scientific theories and concepts which will provide a basis for the rest of the research before moving on to describe the experimental set up. This chapter will detail the RA spectrometer, explaining all the individual components, which will then proceed to describe how the light propagates through the entire system.

The thesis will then go on to investigate the results obtained from the three surfaces studied. The following three chapters will be self-contained and therefore each one will begin with a description of the material and its properties before going on to present the results.

Initially the research will focus on the Si(110) surface studied in air. This chapter will centre around the dependence on the main features in the RA spectrum with increasing temperature. These features coincide with particular transitions in the electronic band structure of silicon.

The second results chapter goes on to present the results from the Ag(110) surface. For this metal the Ag(110) surface can be heated to remove the oxide layer present

on the surface in an atmospheric environment. The main feature in the RA spectrum coincides with the plasmon resonance energy and the azimuthal dependence of the surface at the plasmon resonance energy is different from that observed at other energies within the RA spectrum. Although this dependence is seen clearly in the experiments from a UHV environment, when studied in air, this dependence is not observed. However, evidence presented in this thesis suggests the Ag(110) surface behaves in a similar way as in UHV.

The final results chapter moves away from atmospheric conditions and focuses on the Cu(110)/electrolyte interface. This experiment involves an electropolishing technique to prepare the surface followed by electrochemistry to manipulate the adsorption and desorption of molecules present in the electrolyte. Therefore, it is possible to observe the clean Cu(110) surface and compare with the well understood Cu(110) surface in UHV. The results presented show good agreement with the UHV data, in particular a surface state observed in UHV on the Cu(110) surface is also present on the Cu(110) surface in an electrolyte, although it has been shifted to slightly higher energy.

Finally the thesis will conclude with a brief overview of the results obtained and the conclusions that have been made before finishing with a section discussing any future work that would further this research.

## 1.5 References

- [1] Ofcom 2012. 'Communications Market Report 2012' [online] available at:  
[http://stakeholders.ofcom.org.uk/binaries/research/cmr/cmr12/CMR\\_UK\\_2012.pdf](http://stakeholders.ofcom.org.uk/binaries/research/cmr/cmr12/CMR_UK_2012.pdf)  
Date accessed 12/04/2013
- [2] Joachim, C., Gimzewski, J. K. and Aviram, A., *Nature* **408** (2000) 541
- [3] Smith, C. I., Bowfield, A., Dolan, G. J., Cuquerella, M. C., Mansley, C. P., Fernig, D. G., Edwards, C. and Weightman, P., *J. Chem. Phys.* **130** (2009) 044702
- [4] Convery, J. H., Smith, C. I., Khara, B., Scrutton, N. S., Harrison, P., Farrell, T., Martin, D. S. and Weightman, P., *Phys. Rev. E* **86** (2012) 011903
- [5] Weightman, P., Martin, D. S., Cole, R. J. and Farrell, T., *Rep. Prog. Phys.* **68** (2005) 1251
- [6] Smith, C. I., Harrison, P., Farrell, T. and Weightman, P., *J. Phys: Condens. Matter* **24** (2012) 482002
- [7] McGilp, J. F. *Prog. Surf. Sci.* **49** (1995) 1
- [8] Woodruff, D. P., *Surf. Sci.* **500** (2002) 147
- [9] Hodeau, J. L. and Guinebretiere, R. *Appl. Phys. A-Mater.* **89** (2007) 813
- [10] Jona, F., Strozier, J. A. and Yang, W. S., *Rep. Prog. Phys.* **45** (1982) 527
- [11] Binning, G., Rohrer, H., Gerber, Ch. and Weibel, E., *Phys. Rev. Lett.* **49** (1982) 57
- [12] Barr, T. L., *Crit. Rev. Anal. Chem.* **22** (1991) 229



- [13] Bockris, J. O'M. And Khan, S. U. M., Surface Electrochemistry: A molecular level approach. (Springer, New York) 1993
- [14] Soriaga, M. P., *Prog. Surf. Sci.* **39** (1992) 325
- [15] Kolb, D. M., *Angewandte Chemie, International Ed.* **40** (2001) 1162

# **Chapter 2**

## **Theory**

## 2.1 Crystal Structure

To understand the fundamental properties of materials such as silicon, silver and copper which this research focuses on, it is important to know the basic crystal structure of the material. Crystals are made up of identical building blocks arranged in a three dimension array. These building blocks can be either atoms or small identical groups which are located on a set of mathematical points called the lattice which then give the crystal structure. In three dimensions there are 14 different lattice types which are called Bravais lattices which are allocated to subgroups depending on the cell axes and angles. This research focuses on the cubic group in which all the cell axes are of equal length ( $a_1 = a_2 = a_3$ ) and all angles between them are equal to  $90^\circ$  shown in figure 2.1. The three lattice types within the cubic group are simple cubic (sc), body centred cubic (bcc) and face centred cubic (fcc) of which the latter is the one this research focuses on.

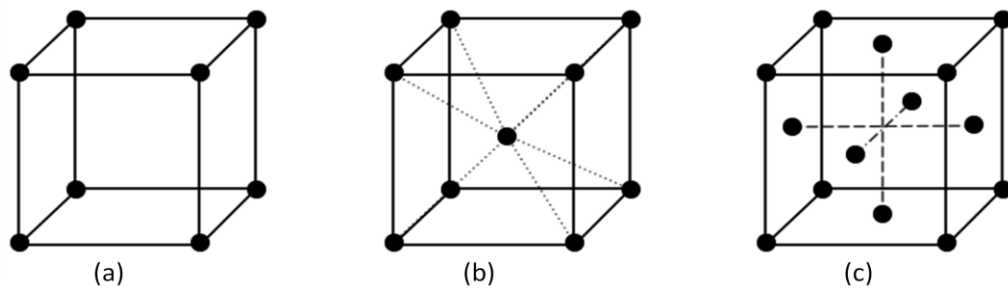


**Figure 2.1: The cubic lattice group with (a) the simple cubic, (b) the body centred cubic and (c) the face centred cubic.**

The Miller indices (or  $(hkl)$  values) are used to describe the orientation of the crystal planes at the surface. In this research the technique used is reflection anisotropy spectroscopy (RAS) hence it is vital that an orientation is used which is anisotropic. Therefore the  $(110)$  orientation is always used since the surface is anisotropic however the cubic nature of the bulk will mean the technique is surface sensitive. This will be more thoroughly discussed, along with the experimental set up, later on.

### 2.1.1 The Reciprocal Lattice and Brillouin Zones

The reciprocal lattice is the Fourier transform of the real space initial lattice and is used to further describe the crystal structure. It also allows the introduction of Brillouin zones which are defined as Wigner-Seitz primitive cells in reciprocal space. It is important to have an understanding of Brillouin zones since they play an important role when discussing the electronic band structure of crystals [1]. The zone boundaries are specified by planes bisecting the lines joining neighbouring lattice points. These planes satisfy the equation for Bragg's law:

$$n\lambda = 2d \sin \theta \quad (2.1)$$

Hence the construction of a Brillouin zone exhibits all the wavevectors which can be Bragg reflected. The construction is shown in figure 2.2.

This text box is where the unabridged thesis included the following third copyright material:

Kittel, C., Introduction to Solid State Physics, Eighth Edition.  
(John Wiley & Sons Inc, Hoboken) 2005

**Figure 2.2: A square reciprocal lattice with the black lines representing reciprocal lattice vectors, white lines show the perpendicular bisectors of the reciprocal lattice vectors. The shaded central square shows the Wigner-Seitz cell of the reciprocal lattice called the first Brillouin zone [1].**

As shown in figure 2.2 the first Brillouin zone is the shaded central square but there are also higher orders of Brillouin zones further away from the origin. The higher order Brillouin zones are shown more clearly in figure 2.3 without the extra construction lines. The first Brillouin boundary occurs at:

$$k = \pm \frac{\pi}{a} \quad (2.2)$$

where  $k$  is the wavevector and  $a$  is the spacing between the planes.

This text box is where the unabridged thesis included the following third copyright material:

Hummel, R. E., Electronic Properties of Materials, Fourth Edition. (Springer, New York) 2011

**Figure 2.3: Schematic of the first four Brillouin zones. The first Brillouin zone has boundaries at  $\pm \pi/a$  [2].**

The Brillouin zones are expanded into three dimensions for a three dimensional lattice, although the illustrations of them become more difficult as seen in figure 2.4 for a fcc lattice. The letters shown in figure 2.4 are the high symmetry points of the Brillouin zone with  $\Gamma$  generally shown as the centre.

This text box is where the unabridged thesis included the following third copyright material:

Myers, H. P., Introductory Solid State Physics, Second Edition. (Taylor & Francis, London) 1997

**Figure 2.4: First Brillouin zone for a fcc lattice [3].**

## 2.2 Band Structure

Until now the discussion has focused on the crystal lattice but another important factor is the movement of electrons through the lattice. To begin with the free electron model is introduced, which describes the motion of electrons in free

space, and then the discussion will focus on how it has been adapted to give a more realistic view of the electron motion. This will then facilitate how band structures have been understood in the context of specific materials.

### 2.2.1 Free Electron Fermi Gas

The free electron gas is a simple model used to describe the kinetic properties of electrons. The Schrodinger equation that describes a free particle in three dimensions is given by:

$$-\frac{\hbar^2}{2m} \left( \frac{\partial^2}{\partial x^2} + \frac{\partial^2}{\partial y^2} + \frac{\partial^2}{\partial z^2} \right) \psi_k(r) = \epsilon_k \psi_k(r) \quad (2.3)$$

where  $\hbar$  is the reduced Planck's constant,  $m$  is the mass of the electron,  $\psi_k(r)$  is a wavefunction with wavevector  $k$  and  $\epsilon_k$  is the energy of the electron in the orbital. If the electrons are confined within a cube with length  $L$  then the wavefunctions which satisfy equation 2.3 are given by a travelling plane wave since the wavefunction must be periodic in all three dimensions with period  $L$ :

$$\psi_k(r) = e^{(ik \cdot r)} \quad (2.4)$$

provided the x, y and z components for  $k$  satisfy:

$$k_{x,y,z} = 0; \quad \pm \frac{2\pi}{L}; \quad \pm \frac{4\pi}{L}; \quad \dots \quad (2.5)$$

Since the wavefunction,  $\psi_k(r)$ , represents a travelling wave this means they will also carry momentum which is given by:

$$p = \hbar k \quad (2.6)$$

The energy,  $\epsilon_k$ , can be found by substituting the wavefunction in equation 2.4 into the Schrodinger equation in equation 2.3:

$$\epsilon_k = \frac{\hbar^2}{2m} k^2 \quad (2.7)$$

where  $k$  is the wavevector in all three dimensions. The Fermi energy can then be related to equation 2.7 since for  $N$  electrons in the ground state the occupied orbitals can be described as points within a sphere in  $k$  space. This sphere will have a radius equal to the wavevector,  $k_F$ , and so the energy at the Fermi surface will be given by:

$$\epsilon_F = \frac{\hbar^2}{2m} k_F^2 \quad (2.8)$$

The Fermi surface is the surface at constant energy,  $\epsilon_F$ , in  $\mathbf{k}$  space and it is important when discussing the electrical properties of metals since it describes the changes of occupancy of states near the Fermi surface.

### 2.2.2 Electronic Band Structure of Solids

As mentioned the free electron Fermi gas is just a model and in reality the assumptions of a one-electron system are too simplistic. For example the free electron model does not provide information into the differences between metals, semiconductors and insulators. To understand further the model needs to be expanded for a solid where the atoms will be more closely packed together. By adding the periodic lattice of the solid, the free electron model becomes the nearly free electron model. Since Bragg reflection occurs in a crystal lattice by monitoring where the reflection takes place, energy gaps are observed. The information gained from energy gaps can then be used to determine the differences between a metal, insulator and semiconductor. The first energy gap occurs at the first Bragg reflection and at integer values thereafter, giving:

$$k = \pm \frac{n\pi}{a} \quad (2.9)$$

This is equal to the boundary conditions for the first Brillouin zone when  $n = 1$  as shown in equation 2.2 although energy gaps will occur at integer values of  $n$ . The differences in the free electron model and when the lattice potential has been added are shown in figure 2.5. As seen in the diagram the relationship between the

energy and wavevector in the free electron case is a parabola whereas the case when the electron is not free shows band gaps. The band gaps occur because as the wavevector approaches the condition in equation 2.9 reflected waves will appear and when the condition is reached there will be equal forward and backward components of the wavefunction leading to standing waves. The two standing waves which are formed are:

$$\psi_+ = e^{i\pi\frac{x}{a}} + e^{-i\pi\frac{x}{a}} = 2 \cos\left(\pi\frac{x}{a}\right), \quad (2.10)$$

$$\psi_- = e^{i\pi\frac{x}{a}} - e^{-i\pi\frac{x}{a}} = 2i \sin\left(\pi\frac{x}{a}\right) \quad (2.11)$$

where  $e^{i\pi\frac{x}{a}}$  and  $e^{-i\pi\frac{x}{a}}$  are the two travelling waves. Since it is not possible to construct a wavefunction which represents an electron state with an energy between the energies of the electron states associated with the wavefunctions in equations 2.10 and 2.11 there will be a gap in the allowed electron states. Hence the energy gap,  $E_g$ , will be the difference in energies of  $\psi_+$  and  $\psi_-$ . Just below the energy gap the wavefunction will be  $\psi_+$  whereas above the wavefunction will be  $\psi_-$ . [4] as shown in figure 2.5.

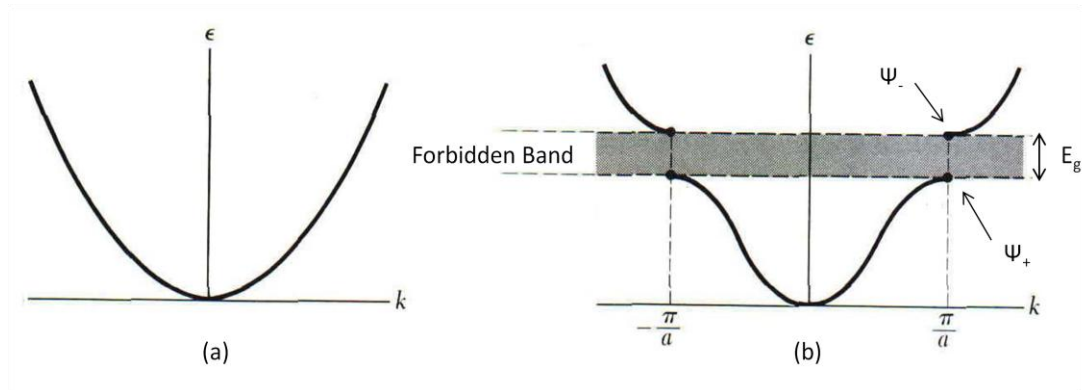


**Figure 2.5: Plot of energy,  $\epsilon$ , against wavevector,  $k$ , for (a) a free electron and for (b) a nearly free electron with lattice constant,  $a$ .**

The first Brillouin zone occurs between  $-\pi/a$  and  $+\pi/a$  and this region is generally called the reduced zone scheme when  $\epsilon$  is plotted as a multi-valued function within



this region. The extended zone scheme is only applicable for the free electron case and  $\epsilon$  is plotted as a single value function from minus to plus infinity. The reduced zone scheme is then set up using Fourier expansions and solving the Schrodinger equation in  $k$  space. This would result in multiple solutions for  $\epsilon$  with  $k$  in the first zone and in the second zone the solutions would have all the same  $\epsilon$  values repeated. Therefore it is concluded that the first zone would give all the information required.

### 2.2.3 Band Structure in Metals

The relative differences in electron occupancy of the energy states allowed in metals, semiconductors and insulators are shown in figure 2.6. The Fermi energy is not shown since it occurs at the boundary of the occupied and unoccupied states for the metal. For the insulator it would occur in the band gap between the occupied and unoccupied energy bands. The semiconductor is a little more complicated since there is more free movement of electrons between the two mainly occupied or mainly unoccupied energy bands but the Fermi energy would again lie in the band gap between these two zones.

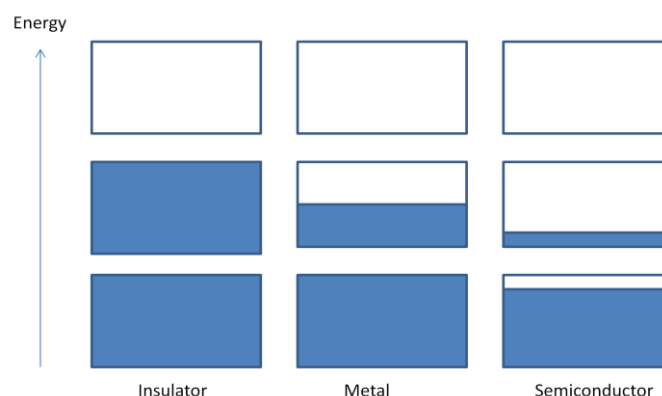


**Figure 2.6: Schematic diagram of the allowed energy bands of an insulator, metal and semiconductor. The shaded regions are filled with electrons whereas the white areas are not.**

As can be seen in the diagram, an insulator has no overlap in the occupied and unoccupied bands whereas the metal and semiconductors do and so these materials exhibit electrical conductivity. It is also important to notice the band gaps

in figure 2.6 where no electron states occur. However, in the band there will be delocalised electron states which show translational invariance. Felix Bloch in 1928 proved that within the periodicity of a crystal lattice the wavefunction for a periodic potential will be the product of a plane wave with another function with the periodicity of the lattice:

$$\psi_{\mathbf{k}}(\mathbf{r}) = u_{\mathbf{k}}(\mathbf{r})e^{i\mathbf{k}\cdot\mathbf{r}} \quad (2.12)$$

Transitions between band states are possible if selection rules allow it.

#### 2.2.4 Semiconductor Band Structure

Semiconductors are vitally important in many applications such as photovoltaic cells, transistors and light emitting diodes (LED's). Therefore understanding their structure and behaviour is the aim of many scientific studies. In general semiconductors have an electrical resistivity in the range of  $10^{-2}$  to  $10^9 \Omega\text{cm}$  and this is temperature dependent. Semiconductors can be pure elements, such as germanium and silicon, be binary compounds such as gallium arsenide, or even organic materials. An intrinsic semiconductor is one which has not been doped with a foreign species so the conductivity, or number of charge carriers, relate to the material properties itself rather than impurities of another material. The electrical resistivity of semiconductors is temperature dependent and when at absolute zero they will generally be insulators and the conduction band will be empty of electrons. The gap between the conduction band and valence band is called the band gap and is material specific. Once the temperature is increased electrons can move from the valence to the conduction band due to the thermal excitation leaving behind holes (unoccupied states). It is this basic principle which explains why the resistivity of semiconductors is highly temperature dependent. The ability for valence electrons to move across the band gap depends not only on the size of the band gap but also the temperature. This can be expressed as a ratio which determines the carrier concentration:

$$\frac{E_g}{k_B T} \quad (2.13)$$

where  $k_B$  is Boltzmann's constant. If this ratio is small, the carrier concentration in the conduction band will be large and so will the conductivity. These band gaps can also be direct or indirect which means either the maxima of the valence band and minima of the conduction band occur at the same value of  $k$  or at different values of  $k$ . In this research silicon is used and this has an indirect band gap with a band gap energy of 1.17 eV at 0 K or 1.11 eV at 300 K [1].

## 2.3 Surfaces

The previous analysis has focused on the general properties of solids and the bulk structure of the material. However, the main aspect of this research is concerned with the surface behaviour of materials which will now be covered in more detail.

Surfaces are different to the bulk material since there is not the three dimensional periodicity that is found within the bulk. There is a smaller interatomic spacing for the topmost three layers of atoms (approximately) which can cause the surface layer to 'relax' although often keeping the same symmetry of the projection of the bulk on to the surface. However, if the surface of the material is compatible with different primitive cells to the bulk then the surface may have reconstructed to a more energetically favourable structure. For example, under UHV conditions, Au(110) has a (1x2) reconstruction on the surface whereas Cu(110) and Ag(110) maintain a (1x1) structure. The stabilisation of the (1x2) structure of the Au(110) surface is thought to be due to the need to lower the kinetic energy of the electrons in the  $s$  and  $p$  electron orbitals at the surface by delocalisation.

### 2.3.1 Surface Phase Transitions

Phase transitions are present in many systems and can be classified as either first or second order transitions. First order transitions include the solid/liquid/gas transitions which involve a latent heat. Second order transitions are continuous

transitions that at thermodynamic equilibrium (at constant temperature and volume) minimise their free energy,  $F$ .

$$F = U - TS \quad (2.14)$$

where  $U$  is the internal energy,  $T$  is the temperature and  $S$  is the entropy of the system. These second order transitions will occur at specific temperatures when the free energy,  $F$ , can be divided between the internal energy,  $U$ , and the entropy,  $S$ . When a transition takes place there will be a change of order in the system and 'order parameters' are defined when the transition temperature,  $T_C$ , is reached. The order parameter changes with  $(T - T_C)^\beta$ , where  $\beta$  is the critical exponent and only depends on the dimensionality of the order parameter, the dimensionality of space and the symmetry of the system.

### 2.3.2 Transitions between Surface States

There are two types of electronic states which are associated with the surface atoms [7], surface resonances and surface states. Surface resonances are located mainly at the surface although there can be some interaction with the bulk since their energies overlap with the bulk bands. Surface states are localised at the surface and have energies within in the bulk energy gap. Figure 2.7 shows the projected bulk band structure at the surface of a metal where  $k_{\parallel}$  is a two dimensional wavevector. The  $k_{\parallel}$  vector characterises a surface Brillouin zone which is similar to the bulk Brillouin zone but on the surface and so the  $k_{\perp}$  rod then extends into the bulk Brillouin zone. The two lines in the band gaps represent where surface states could be present on the surface but not present in the bulk. Since these surface states (resonances) are present for a number of  $k_{\parallel}$  values the states look like a band of states. When this band of states interacts with the projected bulk of the material this bulk state will possess a large amplitude on the surface resulting in a surface resonance.

This text box is where the unabridged thesis included the following third copyright material:

Zangwill, A., *Physics at Surfaces*.  
(Cambridge University Press,  
Cambridge) 1988

**Figure 2.7: Schematic diagram of the bulk band structure at the surface of a metal [8].**

### 2.3.3 Surface Brillouin Zone

As mentioned the surface Brillouin zone will be the projection of the bulk states onto the surface. Figure 2.4 shows a three dimensional fcc Brillouin zone and if a cross sectional slice is taken through it the corresponding surface Brillouin zones can be observed as shown in figure 2.8.

This text box is where the unabridged thesis included the following third copyright material:

Goldmann, A., Dose, V. and  
Borstel, G., *Phys. Rev. B* **32**  
(1985) 1971

**Figure 2.8: Cross section through an fcc bulk Brillouin zones and the projections onto surfaces [9].**

Where the notation of letters are determined by the high symmetry points of the bulk Brillouin zone, as mentioned earlier, but the lines above the letters

representing the surface Brillouin zones denote that these have a two dimensional character.

#### 2.3.4 Optical Response of Surfaces

The dielectric function  $\varepsilon(\omega, k)$ , describes the interaction of light, or electromagnetic radiation in general, with a material. It is an important property which is strongly influenced by the crystal structure since it is very sensitive to changes in the band structure. This means that the study of how the dielectric function changes, can yield insight into the band structure of a material. However, the dielectric function cannot be measured directly so techniques such as reflectivity measurements are used. Although the dielectric function depends on the frequency,  $\omega$ , and the wavevector,  $k$ , of the radiation, during the infrared, visible and ultraviolet regions of the electromagnetic scale the wavevector is very small compared to the frequency and can be treated as zero. The dielectric function,  $\varepsilon(\omega)$  is a complex function and so will have the form as shown in equation 2.15.

$$\varepsilon(\omega) = \varepsilon'(\omega) - i\varepsilon''(\omega) \quad (2.15)$$

Throughout the rest of this thesis the dielectric function will be written just as  $\varepsilon$ , with the real and imaginary parts written as  $\varepsilon'$  and  $\varepsilon''$  respectively. Similarly, equation 2.15 can also be written as a subtraction between the real and imaginary parts of the dielectric function although the notation throughout this thesis will be the addition of these two terms.

This research focuses on electromagnetic radiation in the visible spectrum and under relatively low intensities so the induced electric polarisation in the material is given by:

$$P = \varepsilon_0 \chi^{(1)} E \quad (2.16)$$

where  $\varepsilon_0$  is the dielectric permittivity of free space and  $\chi^{(1)}$  is the first order susceptibility.  $\chi^{(1)}$  measures the degree of polarisation from an incoming electric field and is given by:

$$\chi^{(1)} = \varepsilon - 1 \quad (2.17)$$

where  $\varepsilon$  is the complex dielectric function shown in equation 2.15.

The complex dielectric function,  $\varepsilon$ , cannot be measured directly but using functions such as the reflectance,  $R$ , the refractive index,  $n$ , and the extinction coefficient,  $K$ , information can be obtained. One of the best experimental techniques to obtain information of the dielectric function is to use reflectivity from a surface at normal incidence. The reflectivity coefficient,  $r$ , is the ratio of reflected light,  $E_{ref}$ , with incident light,  $E_{inc}$  as shown below:

$$r = \frac{E_{ref}}{E_{inc}} \quad (2.18)$$

where  $r$  will also be a complex function which will depend on the refractive index,  $n$ , and extinction coefficient,  $K$ , at normal incidence shown in equation 2.19.

$$r = \frac{n - iK - 1}{n - iK + 1} \quad (2.19)$$

This is related to the dielectric function using:

$$\sqrt{\varepsilon} = \sqrt{\varepsilon' - i\varepsilon''} = n - iK = N \quad (2.20)$$

here  $N$  is the complex refractive index and is frequency dependent, explaining the absorption of light as it penetrates into the material.

Equation 2.20 can be solved for  $\varepsilon'$  and  $\varepsilon''$  to give:

$$\varepsilon' = n^2 - k^2 \quad (2.21)$$

$$\varepsilon'' = 2nk \quad (2.22)$$

If the medium is weakly absorbing,  $K$  will be small so  $n \approx \sqrt{\varepsilon_1}$ . The reflectivity,  $R$ , is then given by:

$$R = rr = \left| \frac{N - 1}{N + 1} \right|^2 \quad (2.23)$$

As mentioned earlier, this research uses a technique called reflection anisotropy spectroscopy (RAS) which is discussed in detail in chapter three but uses visible light reflection at near normal incidence and measures the fractional anisotropy in the reflectivity of a surface. Usually denoted as  $\Delta r/r$  where  $\Delta r$  is the difference in reflectance between two orthogonal directions,  $\Delta r = r_x - r_y$ , and  $r$  is the mean reflectance.

### 2.3.5 Plasma Frequency

The induced electric polarisation in the material shown in equation 2.16 can also be written in terms of the displacement,  $\mathbf{D}$ :

$$\mathbf{D} = \varepsilon_0 \mathbf{E} + \mathbf{P} = \varepsilon_0 \varepsilon \mathbf{E} \quad (2.24)$$

since the susceptibility,  $\chi$ , is related to the dielectric function,  $\varepsilon$ , from equation 2.17.

When the number of fixed positive ions and free electrons are equal the solid can be treated like a plasma. In this system the free electrons are best described using a free electron gas model. For a displacement,  $x$ , the equation of motion of the electron is given by:

$$m \frac{d^2 x}{dt^2} = -e \mathbf{E} \quad (2.25)$$

where  $x$  and  $\mathbf{E}$  have a time dependence of the form  $e^{i\omega t}$  where  $\omega$  is the frequency of the light. Substituting this into equation 2.25 gives:

$$-\omega^2 m x = -e \mathbf{E} \quad (2.26)$$

Therefore:

$$x = -\frac{e \mathbf{E}}{\omega^2 m} \quad (2.27)$$

The single electron dipole moment is given by:



$$-ex = -\frac{e^2 \mathbf{E}}{\omega^2 m} \quad (2.28)$$

The polarisation can be defined as the dipole moment per unit volume which is written as:

$$\mathbf{P} = -nex = -\frac{ne^2 \mathbf{E}}{\omega^2 m} \quad (2.29)$$

where  $n$  is the number of electrons per unit volume.

Furthermore, equation 2.24 can be rearranged to give:

$$\varepsilon = \frac{\mathbf{D}}{\mathbf{E}\varepsilon_0} = 1 + \frac{\mathbf{P}}{\mathbf{E}\varepsilon_0} \quad (2.30)$$

which, by substituting equation 2.29 into equation 2.30 gives:

$$\varepsilon = 1 - \frac{ne^2}{\varepsilon_0 \omega^2 m} \quad (2.31)$$

This is the equation for the dielectric function of the free electron gas. If the plasma frequency is then defined as:

$$\omega_p = \sqrt{\frac{ne^2}{\varepsilon_0 m}} \quad (2.32)$$

then equation 2.31 can be rewritten as:

$$\varepsilon = 1 - \frac{\omega_p^2}{\omega^2} \quad (2.33)$$

The plasma frequency is a major determinant of the optical activity, absorbing or reflecting, of a material. Equation 2.20 shows how the complex refractive index,  $N$ , is related to the complex dielectric function,  $\varepsilon$ . Hence, when  $\omega < \omega_p$ ,  $\varepsilon < 0$ ,  $N$  will be imaginary whereas when  $\omega > \omega_p$ ,  $\varepsilon > 0$ ,  $N$  will be real and finally when  $\omega_p = \omega$ ,  $\varepsilon = 0$ . From equation 2.23 for the reflectivity,  $R$ , when  $\omega \leq \omega_p$ ,  $R$  will be unity.  $R$  will decrease when  $\omega > \omega_p$  and then approach zero when  $\omega = \infty$ . Therefore, up

to the plasma frequency, the reflectivity of a gas of free electrons will be at a maximum whereas after the plasma frequency the gas will absorb incident light.

When the dielectric function equals zero there are longitudinal frequencies of oscillation,  $\omega_L$  caused by a displacement,  $u$ , of the entire electron gas with respect to the fixed positive ions. A schematic of this process is shown in figure 2.9. At position (1) the free electron gas is around the fixed positive ions. However, if the entire gas is displaced the positive ions will exert a restoring force to oppose the displacement (2). Position (3) shows the 'overshoot' of the electron gas in the opposite direction resulting in a longitudinal oscillation. These oscillations are called the plasma oscillations where quantised oscillations are known as plasmons.

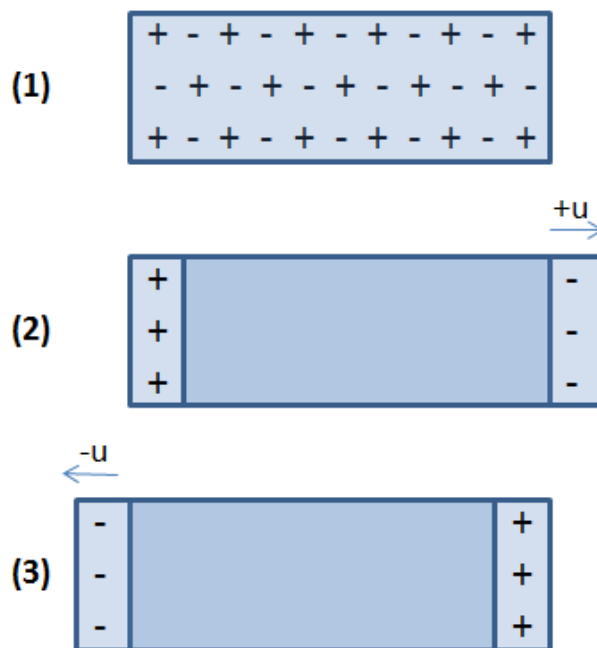


**Figure 2.9: Schematic diagram showing the plasma oscillation with displacement  $u$ .**

A plasmon may be excited by an electron passing through a metallic thin film or reflecting an electron or photon from a film. Although the above has been concerned with metals, plasma oscillations can be excited in dielectrics such as silicon in the same way with the valence electron gas oscillating with respect to the positive ion cores.

## 2.4 The Three Phase Model

Later, chapter three will describe the path of polarised light through the experimental RAS instrument. Here a three phase model is introduced to describe the changes in polarisation as the light is reflected from the surface. McIntyre and Aspnes [10] introduced a linear approximation that can be used for reflectivity calculations and developed the theory of the three layer model which was then progressed further by Cole *et al* [11]. This is shown schematically in figure 2.10.

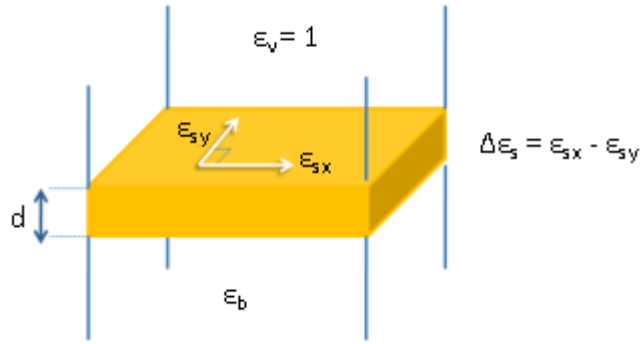


**Figure 2.10: Schematic diagram of the three phase model.**

As shown in figure 2.10 the model is based on an anisotropic surface in between an isotropic semi-infinite bulk and an ambient/vacuum layer each with their own dielectric constants. The dielectric function of the anisotropic surface is split into two orthogonal directions,  $\epsilon_{sx}$  and  $\epsilon_{sy}$ . Due to the surface anisotropy these two values may not be equal so  $\Delta\epsilon_s$  is referred to as the surface dielectric anisotropy (SDA). If it is assumed that the dielectric function of the ambient or vacuum is equal to one and the thin film approximation that  $d \ll \lambda$ , the fractional anisotropy of the surface ( $\Delta r/r$ ) can be given by equation 2.34 [10]. This will be a complex function as it is determined using the dielectric functions of the surface and bulk which are both complex quantities, as shown by the schematic diagram in figure 2.11.

$$\frac{\Delta r}{r} = \Re - i\Im = \frac{4\pi id}{\lambda} \left[ \frac{\Delta\epsilon_s}{\epsilon_b - 1} \right] \quad (2.34)$$

However the bulk and surface dielectric functions are complex quantities as shown in figure 2.10 and by equations 2.35 and 2.36.

$$\Delta\epsilon_s = \Delta\epsilon'_s - i\Delta\epsilon''_s \quad (2.35)$$

$$\epsilon_b = \epsilon'_b - i\epsilon''_b \quad (2.36)$$

where  $\Delta\epsilon'_s = \epsilon'_{sx} - \epsilon'_{sy}$  and  $\Delta\epsilon''_s = \epsilon''_{sx} - \epsilon''_{sy}$ . So equation 2.34 can be written in terms of its real and imaginary parts:

$$Re\left(\frac{\Delta r}{r}\right) = \frac{4\pi d}{\lambda[(\epsilon'_b - 1)^2 + \epsilon''_b{}^2]} \{(\epsilon'_b - 1)\Delta\epsilon''_s - \epsilon''_b\Delta\epsilon'_s\} \quad (2.37)$$

$$Im\left(\frac{\Delta r}{r}\right) = \frac{4\pi d}{\lambda[(\epsilon'_b - 1)^2 + \epsilon''_b{}^2]} \{(\epsilon'_b - 1)\Delta\epsilon'_s - \epsilon''_b\Delta\epsilon''_s\} \quad (2.38)$$

Although most studies using RAS have focused on the real part of the function, in this research some studies have been conducted using the imaginary part and the changes in the experimental set up will be discussed later.

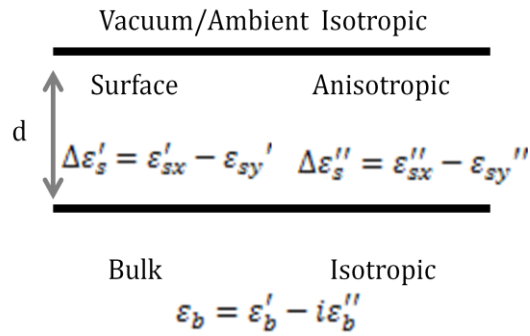


Figure 2.11: Schematic diagram to show the complex dielectric functions.

## 2.5 References

- [1] Kittel, C., Introduction to Solid State Physics, Eighth Edition. (John Wiley & Sons Inc, Hoboken) 2005
- [2] Hummel, R. E., Electronic Properties of Materials, Fourth Edition. (Springer, New York) 2011
- [3] Myers, H. P., Introductory Solid State Physics, Second Edition. (Taylor & Francis, London) 1997
- [4] Ibach, H. and Lüth, H., Solid State Physics, An Introduction to Principles of Materials Science, Fourth Edition. (Springer-Verlag, Berlin Heidelberg) 2009
- [5] Alloul, H., Introduction to the Physics of Electrons in Solids. (Springer-Verlag, Berlin Heidelberg) 2011
- [6] Ho, K. -M. and Bohnen, K. P., *Phys. Rev. Lett.* **59** (1987) 1833
- [7] Kolasinski K. W., Surface Science: Foundations of Catalysis and Nanoscience, Third Edition. (John Wiley & Sons Inc, Chichester) 2012
- [8] Zangwill, A., Physics at Surfaces. (Cambridge University Press, Cambridge) 1988
- [9] Goldmann, A., Dose, V. and Borstel, G., *Phys. Rev. B* **32** (1985) 1971
- [10] McIntyre, J. D. E. and Aspnes, D. E., *Surf. Sci.* **24** (1971) 417
- [11] Cole, R. J., Frederick, B. G. and Weightman, P., *J. Vac. Sci. Technol. A* **16** (1998) 3088

## **Chapter 3**

### **Experimental Set Up**

### 3.1 Reflection Anisotropy Spectroscopy

Reflection anisotropy spectroscopy (RAS) is a surface sensitive, non-destructive optical probe developed from spectroscopic ellipsometry (SE) [1,2]. The technique provides surface sensitive information by exploiting the anisotropy found at the surfaces of some cubic crystals. In many optical probes, the signal is dominated by contributions from the bulk since light can have a penetration depth of many tens of nanometres. In ultra high vacuum (UHV) systems sensitivity is obtained by exploiting the mean free path of electrons which can be up to  $10^5$  km in pressures of around  $10^{-14}$  Pa compared to just 68 nm at ambient pressures. This corresponds to electron escape depths of 13 Å – 83 Å for energies in the region of 320 eV to 3.6 keV [3]. However, these techniques cannot be employed in ambient conditions due to the much shorter mean free path of electrons compared to UHV. RAS can be employed in ambient conditions and if the surface of a cubic crystal is anisotropic, reflectance will occur solely from the surface as the optical response from the bulk will be isotropic. This information is obtained by measuring the difference in reflectance ( $\Delta r$ ) of normal incidence plane polarised light between two orthogonal directions in the surface plane, ( $x, y$ ) then normalised to the mean reflectance ( $r$ ):

$$\frac{\Delta r}{r} = \frac{2(r_x - r_y)}{r_x + r_y} \quad (3.1)$$

where  $r_x$  and  $r_y$  are the complex Fresnel reflection coefficients of the two surface directions respectively.

Thus not only does RAS have the advantage of being non-destructive and surface sensitive, the technique can also be used under a wide range of environments providing they are optically transparent. This enables some of the limitations found in a UHV system to be overcome by expanding investigations of RAS to the solid/liquid interface and hence applications for electrode surfaces in electrochemical environments.

### 3.1.1 The RA Spectrometer and its Components

RAS shares some similarities with SE but there are differences which make RAS individual. Whereas in SE a sample is illuminated using linearly polarised light incident on the surface close the Brewster angle [4], RAS uses linearly polarised light to illuminate the sample at near normal incidence ( $\leq 5^\circ$ ). The potential of RAS was developed in the 1980's with the name reflection difference spectroscopy (RDS) by Aspnes and his co-workers [5] where studies focused on the growth of III-V semiconductors in near atmospheric pressures [6]. The further development of RAS progressed quickly through the following decades and has since been used to study surfaces in UHV and air [7], the metal/liquid interface in an electrochemical environment [8] and, more recently, has led to the study of the adsorption of biological molecules on the electrode surface [9-13]. A schematic diagram of the set up of the RA spectrometer is shown in figure 3.1 and the individual components are described in the order in that the light travels through them. Mirrors are not displayed in the schematic in figure 3.1 but are positioned before the polariser and after the analyser to facilitate focusing the light on the sample and then to ensure the maximum amount of light will progress into the detector..

This text box is where the unabridged thesis included the following third copyright material:

Weightman, P., Martin, D. S.,  
Cole, R. J. and Farrell, T., *Rep.*  
*Prog. Phys.* **68** (2005) 1251

**Figure 3.1: Schematic of the basic components of the RA Spectrometer [7].**



## **Xenon Lamp**

A Xenon lamp is used as the high intensity light source. Specifically it is a Hamamatsu 75 Watt Super-Quiet 9 Xenon arc discharge lamp, used in combination with a stabilised power supply (Hamamatsu C4621-02) which minimises fluctuations from the mains supply. The light radiated from the lamp is generated from an arc discharge when high voltages are applied across the anode to a high performance cathode within a xenon gas environment. Ideally, RAS needs a light source which has a sustainable output between the infrared (IR) and ultraviolet (UV) range (1.5-5.5 eV) of the electromagnetic spectrum which this lamp provides. Initially, when the lamp is switched on the xenon gas pressure can fluctuate preventing thermal equilibrium and hence maximum intensity from being reached. Experiments should only be performed after an hour as the lamp will then have reached a maximal and constant flux.

## **Mirrors**

The mirror before the polariser, after the lamp, collects the light and focuses it on the sample. Then another mirror is placed after the analyser to ensure that as much light as possible is incident on the detector by introducing an astigmatism. This shapes the light beam into a narrow ellipse focused into the narrow entrance slit of the monochromator positioned immediately before the detector. The mirrors used in this set up are front coated UV enhanced aluminium on glass, with a thin silica coating to prevent mechanical abrasion.

## **Polariser**

As seen in equation 3.1, RAS measures the difference in the reflections,  $r_x$  and  $r_y$ , in the  $x$  and  $y$  directions respectively which is generally very small. Hence the polariser and analyser require a high extinction ratio (larger than  $10^5$ ). Prism polarisers are used for this and there are two types that meet the necessary requirements for the RA spectrometer. Rochon and Wollaston prisms split the

beam of light since they consist of two adjacent quartz prisms that separate the ordinary and extraordinary polarised beams which are polarised perpendicular to each other. By contrast Glan prism polarisers use total internal reflection to separate the polarised beams so only a single light beam emerges. This single beam set up is generally preferred in UHV experiments as the equipment can be kept more compact since there are no restrictions on the location of components in the optical layout. However, in this research Rochon prism polarisers are preferred as they are more efficient when transmitting light in the UV region. In this set up two beams emerge from the polariser so care must be taken to ensure the beams do not overlap.

### **Low Strain Window**

The low strain window is used in electrochemical environments primarily due to the presence of the electrolyte solution in which the sample is fully submerged. The window will possess a small inhomogeneous birefringence and so there will be a small contribution from the window in the RAS signal. This can be removed by subtracting a corresponding spectrum from the experimental data. If an electrochemical set up is not being used and the light emerging from the polariser is directly incident on the sample there is no need for the window. There will still be a contribution to the RAS signal from the optical components in the set up not being 100% optically efficient so a corresponding spectrum should still be subtracted from the raw experimental data. The subtraction spectrum used was the difference spectrum between the initial spectrum and when the sample has been rotated by 90°. Although this has a small effect when measuring the real part of the RA spectrum this subtraction is much more significant when measuring the imaginary part to enable the observation of all the features.

### **Photoelastic Modulator**

The photoelastic modulator (PEM) is effectively a tuneable waveplate which modulates the polarisation ellipse of the light reflected from the surface of the

sample by manipulating the property of stress induced birefringence. By applying an electric field to a piezoelectric crystal coupled to an appropriate transparent media, the PEM (specifically a Hinds Instruments Inc, PEM Quartz 90) induces an oscillating birefringence to the optical element which only affects the light linearly polarised parallel to the modulation. Hence leaving the light linearly polarised perpendicular to the modulation unchanged.

Here the transparent media used is fused silica. As the silica is compressed the light parallel to the modulation axis travels faster than the perpendicular component and vice-a-versa when the silica is stretched. This phase difference is called the retardation ( $I$ ) and to achieve significant retardation the crystal is driven at its resonant frequency of 50 kHz, which also allows sequential resolution at the microsecond timescale to be obtained. Since the PEM modulates the phase this enables both the real and imaginary parts of the RA spectra to be measured.

### **Analyser**

The analyser converts the phase modulated signal from the PEM into an amplitude modulated signal which can then be detected. It is of the same design as the polariser and so uses Rochon type prisms although in order to produce a modulated signal which switches between two linearly polarised states it must be orientated at 45 ° with respect to the polariser.

### **Monochromator**

Once the light has passed through the analyser it then travels through a monochromator as its position here will ease the optical alignment of the system. A monochromator is required so the light can be split into discrete wavelengths before detection. In this system a Jobin Yvon (H10) monochromator is used with a holographic grating with 1200 grooves  $\text{mm}^{-1}$  which is suited for an energy range of 1.5-6.2 eV.

## **Detector**

Directly behind the monochromator, to ensure the maximum amount of light enters, is a Hamamatsu (PMT Hamamatsu R955) multi-alkali cathode photomultiplier tube (PMT). The PMT is designed to measure the intensity of the incoming light and then converts the intensity modulated waveform into a current. Since the current is typically of the order of nanoamps the signal needs to be amplified before being converted into a voltage relative to the initial intensity of the light. The signal is made up of both an AC and a DC component. The AC component is related to the surface anisotropy and is superimposed onto a DC offset which is related to the reflectivity. To analyse these two components they are separated by a lock-in amplifier.

Other types of detector can be used, such as silicon photodiodes which are optimised for longer wavelengths, so in the UV range they perform poorly. To improve the performance in the UV range an appropriate coating can be applied which converts UV photons for detection within the visible spectrum. However, this coating reduces the sensitivity and so for this set up the PMT detector is used.

## **Lock-In Amplifier**

In order to analyse the AC and DC components of the voltage signals separately a lock-in amplifier is used. The instrument used in this work uses an EG&G 5210 (dual-phase) lock-in amplifier manufactured by Perkin Elmer Instruments running at a frequency range of 0-120 kHz. By measuring the Fourier coefficients of the 1<sup>st</sup> and 2<sup>nd</sup> harmonics of the signal, the real and imaginary parts of the RA signal can be determined. By using a lock-in amplifier as described, signals at very specific frequencies can be detected which would otherwise be obscured by noise, which is necessary for the detection of the RA signal.

To produce accurate measurements and correct identification of the signal a reference voltage is supplied to the lock-in of the same frequency and phase

relationship as the signal. Hence, any differences between the frequencies of the signal of interest compared to this locked-in signal can be tracked. To achieve this, the locked-in reference signal is taken from the PEM.

### 3.2 Propagation of Light through the System

This section will explain how the light emitted from the Xenon lamp propagates through the instrument.

To understand the RA signal accurately a comprehensive method which can determine the state of polarisation of the light reflected from the surface of the sample is required. To begin with, the electric field vector,  $E$ , of a light wave that can be represented as the superposition of two orthogonal states is defined:

$$E(z, t) = E_{\hat{x}}(z, t) + E_{\hat{y}}(z, t) \quad (3.2)$$

where,

$$E_{\hat{x}}(z, t) = E_{0x} \cos(kz - \omega t + \varphi_x) \quad (3.3)$$

and,

$$E_{\hat{y}}(z, t) = E_{0y} \cos(kz - \omega t + \varphi_y) \quad (3.4)$$

The resulting wave,  $E$ , is therefore the vector sum of components:

$$E(z, t) = \hat{x}E_{0x} \cos(kz - \omega t) + \hat{y}E_{0y} \cos(kz - \omega t + \delta) \quad (3.5)$$

Where  $E_{0x}$  and  $E_{0y}$  are the amplitudes of the waves in the  $x$  and  $y$  directions respectively,  $k$  is the wavenumber,  $z$  is the position in space,  $\omega$  is the angular frequency and  $t$  is time. Also  $\delta = \varphi_x - \varphi_y$  and is the relative phase between the two components  $\varphi_x$  and  $\varphi_y$  which themselves are the phases of the  $x$  and  $y$  waves respectively.

The direction of polarisation of the resultant wave depends on its relative projection along each axis and also on  $\delta$ . So when  $\delta = m\pi$  for  $m = 0, \pm 1, \pm 2 \dots$  the

wave is linearly polarised as it is confined to one plane. For  $E_{0y} = 0$  or  $E_{0x} = 0$  the wave is then limited to vibrations along the x or y axis respectively. Hence, for non zero magnitudes, the linearly polarised light is inclined at an angle,  $\alpha$ , to the x axis, shown in figure 3.2 along with their corresponding Jones vector representations.

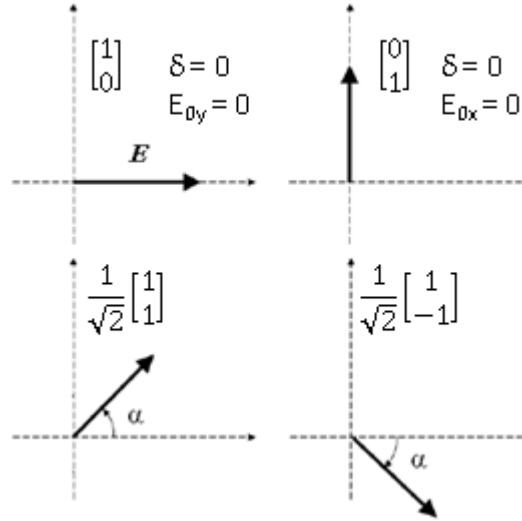


**Figure 3.2: The common linear polarisation states.**

To develop the theory further, the Jones vector notation needs to be introduced. The Jones vector notation was devised by Robert Clark Jones in 1941. It describes the state of polarisation of light in terms of the electric field vector and here it is used to discuss the propagation of light through the RA spectrometer. This notation is only valid for polarised light and although the light emitted from the Xenon lamp is unpolarised, once the light has progressed through the polariser it is observed in a definable polarisation state throughout the rest of the experimental system. Written in the notation of the Jones vector, the resulting wave  $\mathbf{E}$  is:

$$\mathbf{E}(z, t) = \begin{bmatrix} E_{0x}e^{i\delta x} \\ E_{0y}e^{i\delta y} \end{bmatrix} \quad (3.6)$$

where  $\delta_x$  and  $\delta_y$  are the appropriate phases and  $E_{0x}$  and  $E_{0y}$  are again the amplitudes of the waves in the x and y directions. Circular polarisation occurs if the magnitudes are equal,  $E_{0x} = E_{0y}$ , and out of phase by  $\pm \pi/2$ . Although the magnitude

remains constant in this state, the direction of  $\mathbf{E}$  changes with time following a circular path with angular frequency  $\omega$ . This is shown in figure 3.3:

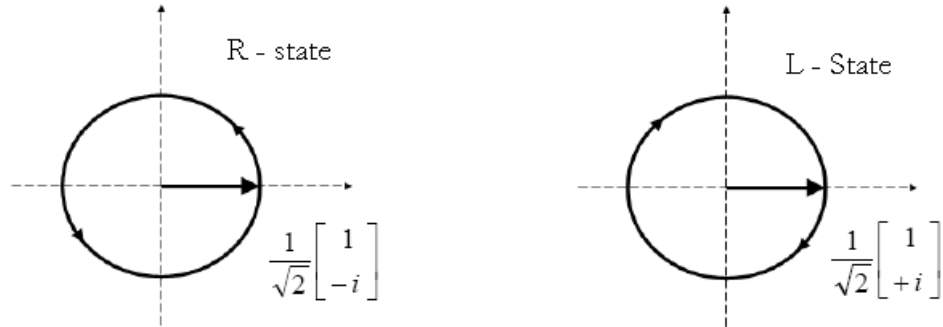


**Figure 3.3: Circular polarisation states.**

If the resultant vector also experiences a change in magnitude the result is a state of elliptical polarisation. Hence, when  $E_{0x} \neq E_{0y}$  and the phase difference,  $\delta$ , is a multiple of  $\pm \pi/2$ , or it also occurs when  $E_{0x} = E_{0y}$  but the phase difference is an arbitrary angle. The elliptically polarised states are shown in figure 3.4 with (a) when  $\delta = \pm \pi/2$  and  $E_{0x} \neq E_{0y}$  and (b) when  $\delta \neq \pm \pi/2$  and  $E_{0x} = E_{0y}$ .

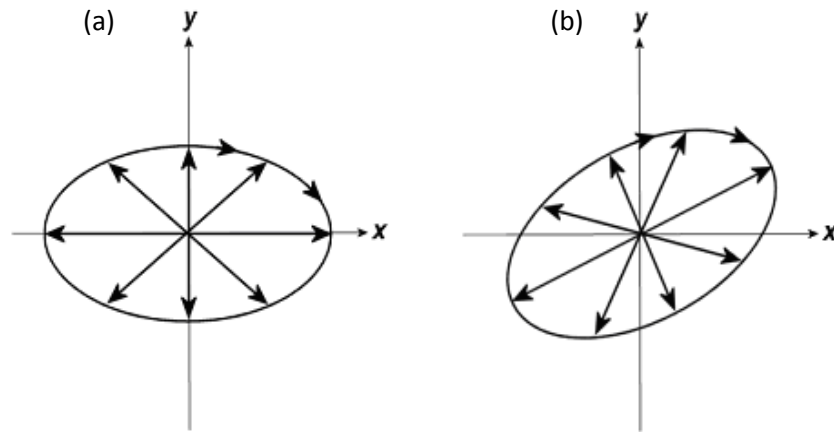


**Figure 3.4: Elliptically polarised states.**

The light which is directed onto the sample is initially linearly polarised. However once it is reflected off the sample surface the light will have an elliptical polarisation due to the surface anisotropy which will induce an elliptical polarisation state. Once the light is reflected from the sample it then passes

through the PEM. The elliptically polarised light which arises from the surface of the sample has a retardation induced from the PEM in different directions. Since this retardation only affects the elliptically polarised light, it is possible to extract harmonics from the amplitude modulation giving information which only derives from the surface anisotropy.

By implementing the Jones vector,  $M$ , the polarisation state of the light can be described from the polarisation state incident to the system,  $E_i$ , to the final polarisation,  $E_f$ , which arrives at the detector, including the effect of all the optical components:

$$E_f = ME_i \quad (3.7)$$

The Jones matrix,  $M$ , is formed by combining the (2x2) matrices which describe the polarisation effect of each optical component in sequence. Each optical component in the system has its own set of optical axes which, for notation purposes, it is necessary to describe. The polariser and analyser have a transmission axis,  $t$ , and an extinction axis,  $e$ , while the PEM has a fast axis,  $f$ , and a slow axis,  $s$ . The sample axes ( $x,y$ ) are taken to be in the  $[1\bar{1}0]$  and  $[001]$  surface directions of the (110) face of a cubic crystal which define the reference frame for each component. To convert the Jones matrix which represents the polarisation state of light to those of the optical component with which it is interacting a rotation matrix,  $R$ , is used:

$$R(\theta) = \begin{bmatrix} \cos(\theta) & -\sin(\theta) \\ \sin(\theta) & \cos(\theta) \end{bmatrix} \quad (3.8)$$

The orientations of the reference frames of the polariser, modulator and analyser are specified by azimuth angles  $P$ ,  $M$  and  $A$  respectively which corresponds to the transmission axes for the polariser and analyser and the fast axis of the modulator. These azimuths are measured from the  $x$  direction of the sample and are characterised as positive for anticlockwise rotation.



Although initially the light from the lamp cannot be assigned a Jones matrix since it is unpolarised, once it has passed through the polariser it is assigned the Jones matrix  $T_p^{te}$  since it is in the reference frame of the polariser:

$$T_p^{te} = \begin{bmatrix} 1 & 0 \\ 0 & 0 \end{bmatrix} \quad (3.9)$$

which is then multiplied by the rotation matrix  $R(P)$  so it is in the  $xy$  plane of the sample:

$$R(P)T_p^{te} = \begin{bmatrix} \cos P & \sin P \\ -\sin P & \cos P \end{bmatrix} \begin{bmatrix} 1 & 0 \\ 0 & 0 \end{bmatrix} = \begin{bmatrix} \cos P & 0 \\ -\sin P & 0 \end{bmatrix} \quad (3.10)$$

If the system is set up for an electrochemical environment the light will enter the electrochemical cell via a strain-free window. The orientation of the window axes are unknown and so are assumed to be equal with that of the  $xy$  frame of the sample. However the window will have some birefringence (fast and slow axes) and hence some retardation of the incident light beam will occur. This is represented by:

$$T_{WI}^{xy} = \begin{bmatrix} 1 & 0 \\ 0 & e^{i\delta_{WI}} \end{bmatrix} \quad (3.11)$$

where  $\delta_{WI}$  is the retardation of the incident beam by the window.  $\delta$  is defined by:

$$\delta = \frac{4\pi d}{\lambda} (n_e - n_o) \quad (3.12)$$

where  $d$  is the thickness of the material,  $\lambda$  is the wavelength of the light and  $n_e, n_o$  are the refractive indices of the extraordinary and ordinary directions of the material respectively. After reflection off the surface the light will exit via the window but by a different part of the window with an associated retardation  $\delta_{WO}$ . The Jones matrix from the surface is:

$$T_s^{xy} = \begin{bmatrix} r_x & 0 \\ 0 & r_y \end{bmatrix} \quad (3.13)$$

The next component the light will pass through is the PEM. Again the reference frame of the light needs to be changed from that of the surface to that of the PEM. This is achieved with the rotation matrix:

$$\begin{aligned} T_M^{fs} R(M) &= \begin{bmatrix} 1 & 0 \\ 0 & e^{i\delta_M} \end{bmatrix} \begin{bmatrix} \cos M & -\sin M \\ \sin M & \cos M \end{bmatrix} \\ &= \begin{bmatrix} \cos M & -\sin M \\ (e^{i\delta_M} \sin M) & (e^{i\delta_M} \cos M) \end{bmatrix} \end{aligned} \quad (3.14)$$

When the light reaches the analyser it is converted to an amplitude modulated signal which requires the same matrix as that applied for the polariser along with the rotation matrix:

$$\begin{aligned} T_A^{te} R(A - M) &= \begin{bmatrix} 1 & 0 \\ 0 & 0 \end{bmatrix} \begin{bmatrix} \cos(A - M) & -\sin(A - M) \\ \sin(A - M) & \cos(A - M) \end{bmatrix} \\ &= \begin{bmatrix} \cos(A - M) & -\sin(A - M) \\ 0 & 0 \end{bmatrix} \end{aligned} \quad (3.15)$$

To form a complete matrix,  $M$ , for the polarisation state for the fully propagated light the matrices for each individual element are combined in the order in which the light interacts. Combining equations 3.10, 3.11, 3.13, 3.14 and 3.15 as follows:

$$M = T_A^{te} R(A - M) T_M^{fs} R(M) T_{WO}^{xy} T_S^{xy} T_{WI}^{xy} R(P) T_P^{te} \quad (3.16)$$

Evaluating the equation above gives:

$$M = \begin{bmatrix} a_{11} & 0 \\ 0 & 0 \end{bmatrix} \quad (3.17)$$

where:

$$\begin{aligned} a_{11} &= (\cos(A - M) \cos M - \sin(A - M)(e^{i\delta_M} \sin M))(r_x \cos P) \\ &\quad - (-\cos(A - M) \sin M \\ &\quad - \sin(A - M)(A - M)(e^{i\delta_M} \cos M))(r_y e^{i\delta_{WO}} e^{i\delta_{WI}} \sin P) \end{aligned} \quad (3.18)$$

The values of the angles  $P$ ,  $A$  and  $M$  used are  $-45^\circ$ ,  $0^\circ$  and  $45^\circ$  respectively. Thus:

$$\sin(\pm 45^\circ) = \pm \frac{1}{\sqrt{2}}, \quad \cos(\pm 45^\circ) = \frac{1}{\sqrt{2}} \quad (3.19)$$

$$\sin(0^\circ) = 0, \quad \cos(0^\circ) = 1$$

Inputting these values into equation 3.18 gives:

$$a_{11} = \frac{r_x}{2\sqrt{2}}(1 + e^{i\delta_M}) + \frac{r_y e^{i\delta_{WO}} e^{i\delta_{WI}}}{2\sqrt{2}}(e^{i\delta_M} - 1) \quad (3.20)$$

Since  $a_{11}$  is the only term in the matrix,  $M$ , to be non zero, the initial equation 3.7 becomes:

$$E_f = \begin{bmatrix} a_{11} & 0 \\ 0 & 0 \end{bmatrix} \begin{bmatrix} 1 \\ 0 \end{bmatrix} = \begin{pmatrix} a_{11} \\ 0 \end{pmatrix} \quad (3.21)$$

The window terms can also be simplified to:

$$e^{i\delta_{WO}} e^{i\delta_{WI}} = e^{i(\delta_{WO} + \delta_{WI})} = e^{i\delta_W} \quad (3.22)$$

Since the total retardation induced by the window, although finite, is small so it is possible to expand the exponential in terms of a power series:

$$e^{i\delta_W} = 1 + i\delta_W + \frac{(i\delta_W)^2}{2!} + \frac{(i\delta_W)^3}{3!} + \dots \approx 1 + i\delta_W \quad (3.23)$$

so equation 3.20 becomes:

$$a_{11} = \frac{1}{2\sqrt{2}} [(r_x - r_y) + (r_x - r_y)e^{i\delta_M} - i\delta_W r_y (1 - e^{i\delta_M})] \quad (3.24)$$

The Fresnel coefficients  $r_x$  and  $r_y$  in the above equation are complex quantities and so can be written in terms of their real and imaginary components:

$$r_x = a + ib, \quad r_y = c + id \quad (3.25)$$

De Moivre's theorem can also be applied to express the term relating to the retardation of the modulator:

$$e^{i\delta_M} = \cos(\delta_M) + i \sin(\delta_M) \quad (3.26)$$

Then after further manipulation  $a_{11}$  becomes:

$$(2\sqrt{2})a_{11} = \alpha + i\beta \quad (3.27)$$

Where  $\alpha$  and  $\beta$  are the real and imaginary parts of  $a_{11}$ . If it is assumed the detector and monochromator are polarisation independent, then once the light has passed through the analyser it is no longer altered so only the time-dependent intensity, at each wavelength, is measured by the detector. The measured time-dependent intensity,  $I$ , is proportional to the square modulus of  $E_f$ , which depends on  $a_{11}$ , hence:

$$I \propto |(2\sqrt{2})a_{11}|^2 = \alpha^2 + \beta^2 \quad (3.28)$$

After some extensive algebraic manipulation the above equation becomes:

$$\begin{aligned} I \propto |a_{11}|^2 &= \frac{1}{4} [(a^2 + b^2) + (c^2 + d^2) + (c^2 + d^2)\delta_W^2] \\ &+ \frac{1}{4} [(a^2 + b^2) - (c^2 - d^2) - (c^2 + d^2)\delta_W^2] \cos(\delta_M) \\ &+ \frac{1}{2} [(ad - dc) - (ac + bd)\delta_W] \sin(\delta_M) \end{aligned} \quad (3.29)$$

which can also be written as:

$$I = I_{dc} + I_\omega \sin(\delta_M) + I_{2\omega} \cos(\delta_M) \quad (3.30)$$

The retardation,  $\delta_M$ , induced by the PEM, varied sinusoidally, hence:

$$\delta_M = \alpha(\lambda) \sin(\omega t) \quad (3.31)$$

Where  $\omega$  is the resonant angular frequency of the modulator and  $\alpha(\lambda)$  is the modulation amplitude which is proportional to the applied excitation voltage and is a function of the wavelength of light. Fourier expansions of  $\cos(\delta_M)$  and  $\sin(\delta_M)$  terms determine the frequency components of the signal, introducing Bessel functions,  $J$ , of argument  $\alpha$  and order  $n$ :

$$\cos(\alpha \sin(\omega t)) = J_0(\alpha) + 2 \sum_{n=1}^{\infty} J_{2n}(\alpha) \cos(2n\omega t) \quad (3.32)$$

$$\sin(\alpha \sin(\omega t)) = 2 \sum_{n=1}^{\infty} J_{2n-1}(\alpha) \sin((2n-1)\omega t) \quad (3.33)$$

When  $J_0(\alpha) = 0$ , which can be achieved by adjusting the voltage applied to the PEM, equation 3.30 becomes:

$$I = I_{dc} + I_{\omega} 2J_1\alpha \sin(\omega t) + I_{2\omega} 2J_2\alpha \cos(2\omega t) + \dots \quad (3.34)$$

The first term of equation 3.29 is time independent, so can be thought of as a DC term. Then by comparing this equation along with equation 3.30 the intensity coefficients are determined. Using the assumption that for small surface anisotropies  $r_x \sim r_y$  for additive terms and by considering only the first order window strain terms, the normalised frequency terms are found to be:

$$I_{dc} \sim \frac{(|r_x|^2 + |r_y|^2)}{2} = R \quad (3.35)$$

$$\frac{I_{\omega}}{I_{dc}} \sim \text{Im}\left(\frac{\Delta r}{r}\right) - \delta_w \quad (3.36)$$

$$\frac{I_{2\omega}}{I_{dc}} \sim \text{Re}\left(\frac{\Delta r}{r}\right) \quad (3.37)$$

Therefore the  $I_{dc}$  term is a measure of the reflectivity of the material. The imaginary part of  $\left(\frac{\Delta r}{r}\right)$  is measured at frequency,  $\omega$ , and is dependent on the first order window strain term whereas the signal at  $2\omega$  measures the real part of  $\left(\frac{\Delta r}{r}\right)$  and is only sensitive to the second order window strain term. Since the window strain effects were substantial for the imaginary measurements, which made conclusions more complicated, the majority of published RAS measurements are from the real part of the RA profile. This research will observe both the real and imaginary measurements as the constant updating of equipment has enabled the window

strain to become negligible. Re-writing equations 3.36 and 3.37 in terms of their Bessel functions gives:

$$\frac{I_{\omega}}{I_{dc}} = 2J_1(\delta_0)Im\left(\frac{\Delta r}{r}\right) \quad (3.38)$$

$$\frac{I_{2\omega}}{I_{dc}} = 2J_2(\delta_0)Re\left(\frac{\Delta r}{r}\right) \quad (3.39)$$

This makes it obvious that the real and imaginary parts are separated by their frequency dependence. Figure 3.5 shows the Bessel functions for the first 5 integers. To measure the real part of the signal the retardation is set so that it coincides to where  $J_2(x)$  is a maximum, at 3.054, therefore set the retardation to 3.054 radians. To change this for the imaginary part the retardation is set to where  $J_1(x)$  is a maximum, at 1.854 radians.

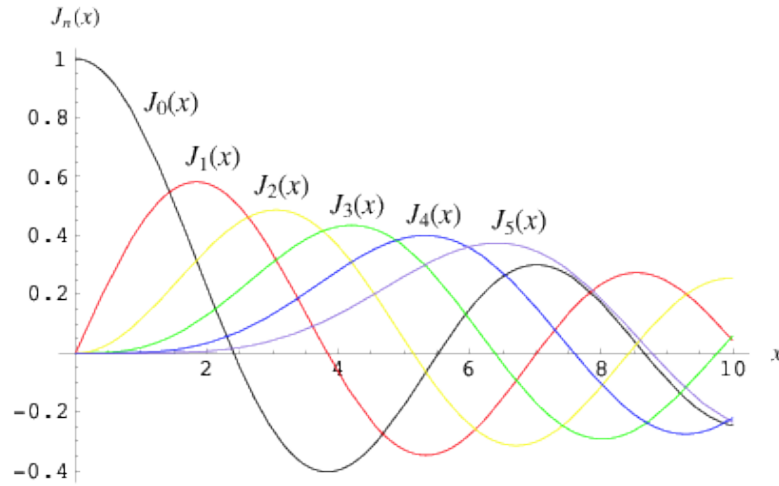


Figure 3.5: Plot of Bessel functions.

### 3.2.1 Errors

The major sources of errors in the experimental set up are the possible misalignment of the optical components and the sample. Any misalignment of the polarisation dependent components will result in an offset of the measured  $Re\left(\frac{\Delta r}{r}\right)$  which although does not introduce new features it will create problems

when quoting absolute values of  $Re\left(\frac{\Delta r}{r}\right)$ . However, variations in line-shape between measured spectra can be investigated more accurately. These effects of misalignment have been studied in detail [14] which found the relationship between the polariser and modulator is very sensitive to misalignment but an analyser misalignment has less of an impact.

### **3.3 Azimuthal Dependent Reflection Anisotropy Spectroscopy**

So far RAS has been considered as an optical probe of surfaces using light of near normal incidence on a stationary sample. However, if the sample is rotated in the plane of the surface, in the 'azimuthal' angle, a more thorough understanding of the surface can be obtained. This is called azimuthal dependent reflection anisotropy spectroscopy (ADRAS). For example, ADRAS can gain information on the optical anisotropy of adsorbed species on a surface [7,15,16,17] but also understand how clean surfaces behave as they are rotated.

To perform ADRAS experiments the sample surface is orientated to ensure the principle axes of the surface are 45 ° to the plane of polarisation of the incident light as this will produce the maximum intensity of the RA response. An example of an ADRAS spectra is given in figure 3.6 and shows the results obtained from a Au(110) surface rotated through an azimuthal angle,  $\vartheta$ , of 180 ° away from the initial 45 ° position as shown in figure 3.7.

This text box is where the unabridged thesis included the following third copyright material:

Mansley, C., Ph. D. Thesis. The University of Liverpool (2010)

**Figure 3.6: RA spectra of Au(110) as a function of angular rotation,  $\vartheta$ , from 0° to 90° at 0.0 V vs SCE and pH 7.1 [18].**

The Au(110) surface is in an electrochemical environment of a phosphate buffer at 0.0 V which ensures the surface is stable and suitable for electrochemistry studies as will be discussed in the next section. At  $\vartheta = 0^\circ$  the RA spectrum is at a maxima however as  $\vartheta$  tends towards  $45^\circ$  the intensity decreases until at  $\vartheta = 45^\circ$  the RA spectrum is featureless. This is due to the loss of anisotropy in the reflected light since the polarisation direction of the incident light is parallel to one of the optical axes of the surface and orthogonal to the other. As  $\vartheta$  increases towards  $90^\circ$  the RA spectrum will tend towards a maxima but of opposite sign. At  $\vartheta = 90^\circ$  the RA spectrum is a mirror image of that at  $\vartheta = 0^\circ$ . This is due to the anisotropic response which arises from  $r_{[001]} - r_{[1\bar{1}0]}$  rather than  $r_{[1\bar{1}0]} - r_{[001]}$ . Increasing  $\vartheta$  further will result in another featureless RA spectrum at  $\vartheta = 135^\circ$  before increasing back to its initial position at  $\vartheta = 180^\circ$ . Hence the Au(110) surface shows a  $\cos 2\vartheta$  dependence.



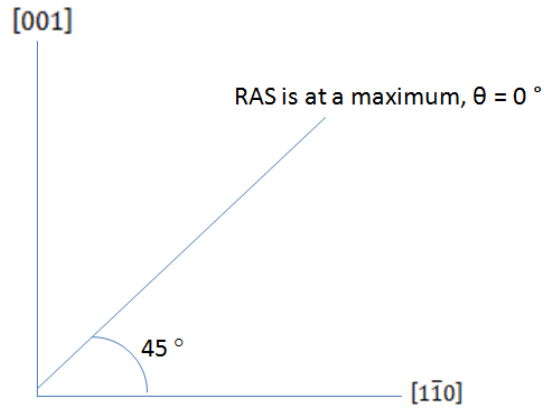


**Figure 3.7: Schematic diagram showing how the sample is initially aligned at 45° with respect to the principal crystallographic directions for the maximum RA signal to be produced.**

The loss in anisotropy of reflected light as the incident light is parallel to one of the principal crystallographic directions is explained by aligning the sample to an angle  $\delta$  with respect to the crystallographic directions, in this case, x and y as shown in figure 3.8. If the PEM flips the polarisation by  $\pm 45^\circ$  then if  $\delta = 45^\circ$ ,  $\Delta r = r_y - r_x$ .

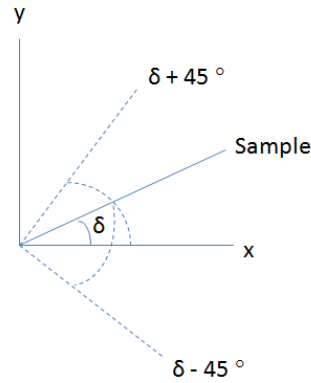


**Figure 3.8: Schematic diagram showing the angles involved when the PEM flips the polarisation by  $\pm 45^\circ$  with respect to the sample.**

By applying rotation matrices to the sample matrix, given in equation 3.13, and by focusing only on the terms which coincide with  $r_x$  and  $r_y$ , the reflection coefficients are:

$$r_{\delta+45} = r_{xx} \cos^2(\delta + 45) + r_{yy} \sin^2(\delta + 45) \quad (3.40)$$

$$r_{\delta-45} = r_{xx} \cos^2(\delta - 45) + r_{yy} \sin^2(\delta - 45) \quad (3.41)$$

therefore:

$$\Delta r = (r_{\delta+45} - r_{\delta-45}) \quad (3.42)$$

By inputting equations 3.40 and 3.41 into equation 3.42 gives:

$$\Delta r = r_{xx}a + r_{yy}b \quad (3.43)$$

where:

$$a = \cos^2(\delta + 45) - \cos^2(\delta - 45) \quad (3.44)$$

$$b = \sin^2(\delta + 45) - \sin^2(\delta - 45) \quad (3.45)$$

Focusing on  $a$  initially and by expanding the squared terms gives:

$$a = [\cos(\delta + 45) + \cos(\delta - 45)][\cos(\delta + 45) - \cos(\delta - 45)] \quad (3.46)$$

Then following some algebra this gives:

$$a = (2 \cos \delta \cos 45)(-2 \sin \delta \sin 45) = -2 \sin \delta \cos \delta \quad (3.47)$$

and by using a trigonometric identity allows  $a$  to become:

$$a = -\sin 2\delta \quad (3.48)$$

If the same process is followed for the calculation of  $b$ , this gives:

$$b = \sin 2\delta \quad (3.49)$$

Therefore substituting these values into equation 3.43:

$$\Delta r = -r_{xx} \sin 2\delta + r_{yy} \sin 2\delta \quad (3.50)$$

Hence at  $\delta = 0^\circ$ ,  $\Delta r = 0$  and so there is no anisotropy whereas when  $\delta = 45^\circ$ ,  $\Delta r = r_{yy} - r_{xx}$ .

Once the ADRAS data has been obtained for the clean surfaces it is then possible to determine how adsorbed species are aligned or ordered on the surface [17]. This is made possible by fitting the angular variation at a specific dipole transition energy to an equation of the form;

$$Re\left(\frac{\Delta r}{r}\right) = C + D \cos(2\theta + \phi) \quad (3.51)$$

Where  $C$  and  $D$  are constants with  $D$  measuring the optical response,  $\phi$  is the phase angle between the direction of the dipole projected onto the surface and the optical axes of the surface and  $\theta$  is the azimuthal angle [19] as shown in figure 3.9. In the schematic diagram the  $x$  and  $y$  axis represent the crystallographic directions,  $[001]$  and  $[1\bar{1}0]$  respectively. If  $\phi$  for the adsorbed species is different to that of the substrate then it is not aligned with the substrate transition [15,16,17]. Equation 3.51 is only valid for RA spectra which have a  $\cos 2\theta$  dependence.

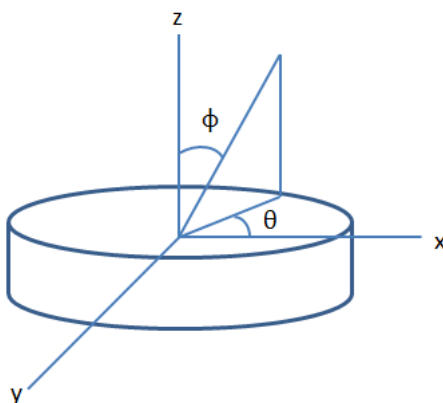


Figure 3.9: Schematic diagram of the geometry of the angles involved in equation 3.51.

### 3.4 Electrochemistry

Electrochemistry is the study of chemical reactions which take place at the interface of an electrode and a chemical species in solution. This involves the transfer of electrical charge, specifically the transfer of electrons, across this interface. A potential gradient exists at the electrode surface which drives this electron transfer. However, since the distance between the electrode and the

solution is so small the potential gradient can be in the order of  $10^{10} \text{ Vm}^{-1}$  [20]. To have a full understanding of the interfacial region, the core of electrochemistry, requires thorough knowledge of the movement of charged ions in solution attracted to the electrode surface, the structure of the adsorbed species and the effect the potential field has in this region.

One of the earliest models proposed to describe the interfacial region was suggested by Hermann Von Helmholtz in 1853 [21] who coined the term 'electric double layer'. His model assumes there is no electron transfer in the interface between the electrode and the solution; hence, the interface must be neutral overall. The charge on the electrode is balanced by an equal and opposite charge of the solution which arises from the redistribution of the electrolyte ions to the surface of the electrode, called the 'electric double layer'. This model described by Helmholtz is similar to a molecular scale parallel plate capacitor with a linear potential drop separating two plates of equal and opposite charge. Here one plate represents the electrode surface whilst the other plate is thought of as the plate which passes through the solvated ions at their closest approach. This is known as the Outer Helmholtz plane (OHP).

This model has been modified and improved, initially by Gouy [22,23] and Chapman [24], who considered that charge is free to move and also subject to thermal motion. So the largest concentration of counter ions is found close to the electrode with excess charge dispersing away from the electrode into a diffuse layer with decreasing concentration until a homogeneous distribution of ions within the bulk electrolyte is reached [25]. This theory was again improved by Stern [26] who stated there must be a plane of closest approach, as in the Helmholtz model, since ions have a finite size. The final model, by Grahame in 1947 [27], which is accepted as the current acknowledged model, explains that two planes of closest approach are required, one for specifically adsorbed ions and one for non-specifically adsorbed ions. Although the inner layer would be mostly occupied by solvent molecules, Grahame suggested some ions or molecules which had lost their

weakly bound solvation shells could form a chemical bond to the electrode surface. This adsorption is only possible for certain molecules with certain electrodes, hence are referred to as specifically adsorbed. This introduces a plane through the centre of the specifically adsorbed ions called the Inner Helmholtz plane (IHP). The full model is shown in figure 3.10:

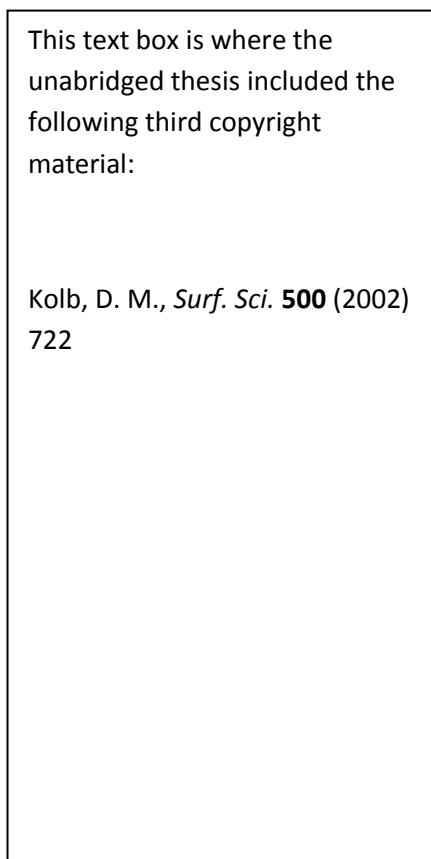


**Figure 3.10: Schematic diagram of the interfacial region showing a graph of the potential drop across the interface [28].**

From figure 3.10, it can be seen the specifically adsorbed molecules at the IHP show a steep potential drop (purple curve) followed by an overshooting of the potential with respect to the bulk electrolyte value. In contrast, non specifically adsorbed molecules show a linear drop in potential (red curve) across the interface. The potentials  $\varphi_m$ ,  $\varphi_s$ ,  $\varphi_1$  and  $\varphi_2$  correspond to the potentials inside the metal, the electrolyte, the IHP at  $Z_1$  and the OHP at  $Z_2$  respectively.

When a potential is applied to an electrode in an electrolyte its surface will become more charged, the value of which is dependent on the electrode material, the electrolyte used and the potential applied. If the applied potential is made more negative the electrons will flow into the electrode surface resulting in a negatively shifting surface charge and, conversely, if the potential is made more positive, electrons will move from the surface and the charge will become less negative and eventually positive.

### 3.4.1 Measuring Electrode Potential

During electrochemical investigations the majority of reactions of interest occur at the working electrode. It is therefore essential to have an accurate method of measuring the potential drop across the electrode and the solution since direct measurement of the electrode potential is not possible. For example, if the measurement of the potential drop is attempted using a standard digital voltmeter (DVM) there will be no electrical contact and so will not work since the free-electrons will not pass from the DVM probe to the solution. By introducing a second electrode, indirect measurement is possible by measuring the potential difference between the two electrodes.

The reference electrode provides a fixed potential throughout the experiment [25], hence any change in the applied potential is across the working electrode and solution which can be measured. This potential control is performed with an Autolab PGSTAT30 potentiostat. The final measurement is written as the difference of two metal/solution potential drops:

$$\Delta\phi = (\phi_{(metalA)} - \phi_{(solution)}) - (\phi_{(metalB)} - \phi_{(solution)}) \quad (3.52)$$

$$\Delta\phi = \phi_{(metalA)} - \phi_{(metalB)} \quad (3.53)$$

Since, as we have mentioned one of the electrodes in a two electrode set up represents a reference electrode, the other will represent a test system so we can write this as:

$$\Delta\phi = (\phi_{(test)} - \phi_{(solution)}) - (\phi_{(reference)} - \phi_{(solution)}) \quad (3.54)$$

Since the potential drop across the reference electrode/solution is constant, this can be rewritten as:

$$\Delta\phi = \phi_{(test)} - \phi_{(solution)} - k \quad (3.55)$$

where  $k$  is a constant.

Although it is still not possible to directly probe the value of  $\phi_{(test)} - \phi_{(solution)}$  the changes in this value can be determined.

The electrochemical experiments conducted in this research use large currents which means the two electrode set up cannot be used. This is because the large currents can alter the ionic concentration so the difference between the reference electrode and measured potential will no longer be constant. By introducing a 'counter electrode' this problem is overcome since it allows the passage of current between it and the working electrode, so preventing current flowing between the reference electrode and working electrode.

In this research a silver/silver halide electrode acts as the reference electrode submerged in a halide solution, the working electrode is a Cu(110) crystal and the counter electrode is a platinum wire. All potentials quoted in this research are quoted versus the silver/silver halide electrode.

### 3.4.2 The Electrochemical Cell

The electrochemical cell used is a 3-electrode cell designed and built by Klaus Wandelt and co-workers [29], a diagram is shown in figure 3.11:

This text box is where the unabridged thesis included the following third copyright material:

Wilms, M., Kruft, M., Bermes, G. and Wandelt, K., *Rev. Sci. Instrum.* **70** (1999) 3641

**Figure 3.11: Schematic diagram of the electrochemical cell from [29]. a) top view and b) cross section.**

In figure 3.11 the working (generator) electrode is shown as being wrapped around the sample. This is achieved by using contact pins which make contact at the back of the copper sample, ensuring it acts as the working electrode. This cell is then placed under an argon chamber to avoid oxygen contamination with a quartz low strain window to ensure the light can illuminate the sample and then be reflected back.

### **3.4.3 Cyclic Voltammetry**

Cyclic Voltammetry (CV) is a very common technique used to study electrochemical reactions. CV monitors the current between two electrodes as a function of applied potentials. The potential is varied using a potentiostat at a precise sweep rate given by  $dV/dT$ . The potentiostat acts in a similar way to a feedback current based on an operational amplifier since it ensures zero current flow through the reference electrodes. The CV profiles taken are known as cyclic voltammograms and peaks in the spectra can arise from electron transfer dependent reactions including formation or breaking of bonds and ionic adsorption or desorption on the surface.



The range of the applied voltage 'sweeps' chosen is dependent on the electrodes and electrolytes used and is generally performed to try and observe a specific electrode reaction. The scan can then be reversed to determine if the products of electron transfer are stable, intermediates or electroactive. CVs are only a measurement of electron transfer and structural or chemical information cannot be measured directly. Hence, CVs are generally used alongside other techniques such as RAS.

### **3.5 Crystal Preparation**

During the research presented there were three materials used, silicon, silver and copper. The Si(110) wafers used are 99.999 % purity with a thickness of 100  $\mu\text{m}$ . The wafers were rinsed using acetone before being dried and transferred to a heating stage, since these experiments are designed to investigate the temperature dependence of silicon.

The Ag(110) crystals used were single crystals with 99.999 % purity in the form of discs of diameter 10.00 mm and thickness 1.00 mm with an orientation accuracy of  $< 0.1^\circ$ . These crystals were also involved in temperature dependence experiments so were again rinsed in acetone and left to dry before being transferred to the heating stage.

Finally the Cu(110) crystals were single crystals of 99.999 % purity, in the form of discs with a diameter of 8.00 mm and a thickness of 3.00 mm with an orientation accuracy of  $0.1^\circ$ . In this research there were two main ways in which the Cu(110) crystals were prepared for the experiments; ion bombardment and annealed in UHV or electropolishing.

For UHV preparation the Cu(110) sample was positioned on a heating stage in a UHV chamber with a base pressure of  $\sim 1 \times 10^{-9}$  mbar. Cleaning of the Cu(110) surface is performed using cycles of argon ion sputtering ( $8 \mu\text{A}/\text{cm}^2$ , 500 eV for 20 minutes at 300 K) followed by annealing to 860 K for 30 minutes. Generally around

10 cycles were performed for a good surface to be obtained. A Low Energy Electron Diffraction (LEED) pattern or X-ray Photoelectron Spectroscopy (XPS) spectrum was taken to check the surface is clean Cu(110).

The second method to prepare the Cu(110) surfaces is electropolishing. The electropolishing technique uses a 50 % solution of phosphoric acid ( $\text{H}_3\text{PO}_4$ ) using the hanging-meniscus method for  $\sim 15$  seconds with a positive voltage applied between the surface and a platinum disc submerged in the  $\text{H}_3\text{PO}_4$ . The Cu(110) surface is moved around whilst in contact with the  $\text{H}_3\text{PO}_4$  to ensure an even polishing of the surface as seen in figure 3.12:

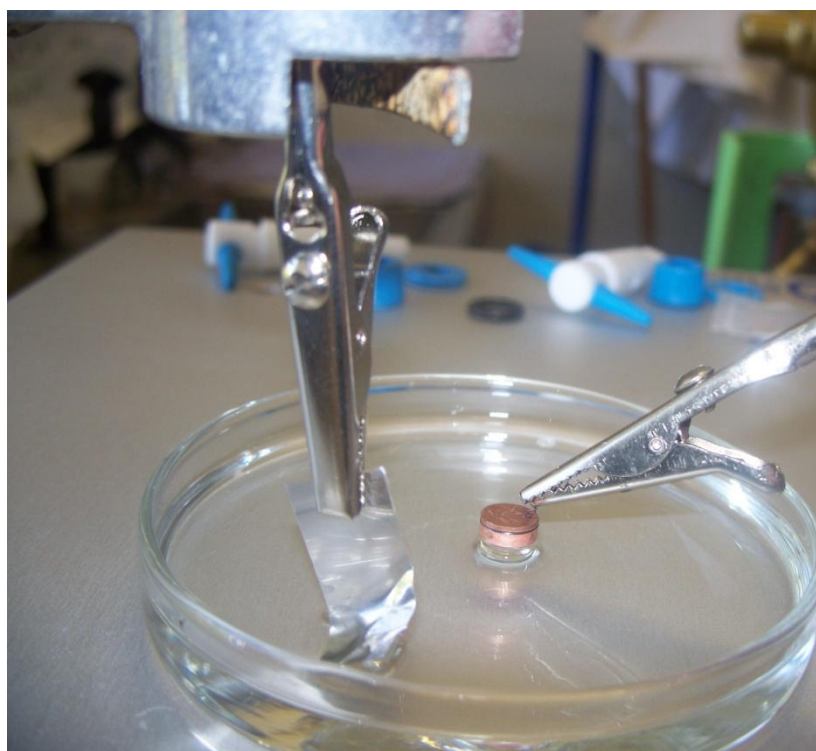


**Figure 3.12: Photo showing the hanging-meniscus method with the Cu(110) surface in contact with the  $\text{H}_3\text{PO}_4$  and the platinum part-submerged in the acid.**

Contact is made with the Cu(110) surface using a tantalum wire wrapped around the crystal, again ensuring an even polishing of the crystal. The Cu(110) surface is then rinsed with the electrolyte being used and transferred to the electrochemical cell with a droplet of electrolyte on the surface to avoid oxidation in air.

Experiments were performed in ultra-pure water (Millipore 18 MΩcm) and in electrolyte solutions of 5 mM H<sub>2</sub>SO<sub>4</sub>, 10 mM HCl and 5 mM H<sub>2</sub>SO<sub>4</sub> + 10 mM KBr and all solutions were degassed with argon before use. An argon chamber is then placed over the electrochemical cell to avoid any contamination with oxygen.

### **3.6 Low Energy Electron Diffraction and X-ray Photoelectron Spectroscopy**

Primarily in this research the Low Energy Electron Diffraction (LEED) and X-ray Photoelectron Spectroscopy (XPS) techniques were used to observe clean crystals in UHV before they were removed to study using RAS. This process is essential because to be able to have a full understanding of the behaviour of the surface using RAS it is necessary to know what the surface looks like before being transferred from UHV to ambient conditions. This transfer process for the Cu(110) surface is very difficult since the surface oxidises quickly in air. In this work this transfer from a UHV environment to the electrochemical cell was achieved by initially allowing argon into the chamber and then adding a droplet of the electrolyte as this stabilises the surface and oxidation will not occur. The electrolyte was then be removed from the surface using cyclic voltammetry where there will be a particular voltage range when the clean Cu(110) surface will be observable.

Ideally these two techniques would be used alongside each other so the surface atomic order would be determined by LEED patterns and cleanliness monitored by XPS. However the UHV equipment used in this research could not have both techniques used at the same time so just one method was deemed sufficient alongside the electrochemistry and RAS experiments conducted.

#### **3.6.1 Low Energy Electron Diffraction**

LEED is a UHV technique which is used to determine the surface structure of crystalline materials by bombardment with a collimated beam of low energy electrons which are then backscattered on a fluorescent screen giving rise to

diffraction (or Bragg) spots. LEED relies on the fact that the electrons used have an energy range of 20-500 eV which correspond to wavelengths from 2.7-0.5 Å using equation 3.56. This is comparable to the lattice spacing so diffraction will take place.

$$\lambda = \left( \frac{150.4}{E} \right)^{\frac{1}{2}} \quad (3.56)$$

Another advantage of using electrons in this energy range is the inelastic mean free path is ~ 5-20 Å hence electrons only penetrate a few atomic layers into the solid ensuring a surface sensitive technique.

The full detail of the experiment will not be discussed in this thesis. However, the set up used can be found in reference 29 which describes the experimental technique in detail.

### 3.6.2 X-ray Photoelectron Spectroscopy

The basic principle of electron spectroscopy is to excite electrons using photons or electron beams which can then be detected. XPS uses X-rays as the source of energy and works based on the photoelectric effect. The photoelectric effect was initially detected by Heinrich Hertz in the late nineteenth century [31]. In 1905, Einstein [32] then used Planck's quantum theory of blackbody radiation to propose that if the frequency ( $\nu$ ) of the incident electromagnetic radiation reaches a specific threshold, an electron could absorb a quantum of energy and be emitted from the material with a kinetic energy,  $E_K$ . This threshold is known as the work function,  $\phi$ , and for XPS is the work function of the electron analyser. These values are related to each other, including the binding energy of the emitted electrons  $E_B$ , using the photoelectric effect shown in equation 3.57:

$$E_K = h\nu - E_B - \phi \quad (3.57)$$

The binding energy of an electron is defined as the amount of energy required for those electrons to escape the attractive force from the atom's positive nucleus. The

work function is defined as the minimum energy required to move an electron from a solid to a point immediately outside the solid surface, or the energy needed to move an electron from the Fermi level to the vacuum level. Since the work function is known for specific materials, in this case the electron analyser, and the kinetic energy of the electrons can be measured using equation 3.57 the binding energy can be determined allowing the identification of the characteristic energy levels of individual elements to be established.

As with the LEED experimental set up, the XPS set up will not be discussed in detail in this thesis and further information about the technique and instrument used can be found elsewhere [33].

### 3.7 References

- [1] Jenkins, T. E., *J. Phys. D: Appl. Phys.* **32** (1999) R45
- [2] Vedam, K., *Thin Solid Films.* **313** (1998) 1
- [3] Klasson, M., Berndtsson, A., Hedman, J., Nilsson, R., Nyholm, R. and Nordling, C., *J. Electron. Spectrosc.* **3** (1974) 427
- [4] Azzam, R. M. and Bashara, N. M., *Ellipsometry and Polarised Light.* (Elsevier, Amsterdam) 1997
- [5] Aspnes, D. E., Colas, E., Stunda, A. A., Bhat, R., Koza, M. A. and Keramidas, V. G., *Phys. Rev. Lett.* **61** (1988) 2782
- [6] McGilp, J. F., *Prog. Surf. Sci.* **49** (1995) 1
- [7] Weightman, P., Martin, D. S., Cole, R. J. and Farrell, T., *Rep. Prog. Phys.* **68** (2005) 1251
- [8] Sheridan, B., Martin, D. S., Power, R. J., Barrett, S. D., Smith, C. I., Lucas, C. A., Nichols, R. J. and Weightman, P., *Phys. Rev. Lett.* **85** (2000) 4618
- [9] Smith, C. I., Maunder, A. J., Lucas, C. A., Nichols, R. J. and Weightman, P., *J. Electrochem. Soc.* **150** (2003) E233
- [10] Smith, C. I., Dolan, G. J., Farrell, T., Maunder, A. J., Fernig, D. G., Edwards, C. and Weightman, P., *J. Phys.: Condens. Matter.* **16** (2004) S4385
- [11] LeParc, R., Smith, C. I., Cuquerella, M. C., Williams, R. L., Fernig, D. G., Edwards, C., Martin, D. S. And Weightman, P., *Langmuir* **22** (2006) 3413
- [12] Smith, C. I., Bowfield, A., Dolan, G. J., Cuquerella, M. C., Mansley, C. P., Fernig, D. G., Edwards, C. and Weightman, P., *J. Chem. Phys.* **130** (2009) 044702

- [13] Bowfield, A., Smith, C. I., Dolan, G. J., Cuquerella, M. C., Mansley, C. P. and Weightman, P., *e\_j, Surf. Sci. Nanotech.* **7** (2009) 225
- [14] Maunder, A., Ph. D. Thesis. The University of Liverpool. (2001)
- [15] Macdonald, B. F. and Cole, R. J., *Appl. Phys. Lett.* **80** (2002) 3527
- [16] Macdonald, B. F., Law, J. S. and Cole, R. J., *J. Appl. Phys.* **93** (2003) 3320
- [17] Weightman, P., Dolan, G. J., Smith, C. I., Cuquerella, M. C., Almond, N. J., Farrell, T., Fernig, D. G., Edwards, C. and Martin, D. S., *Phys. Rev. Lett.* **96** (2006) 086102
- [18] Mansley, C., Ph. D. Thesis. The University of Liverpool (2010)
- [19] Farrell, T., Harrison, P., Smith, C. I., Martin, D. S. and Weightman, P., *Appl. Phys. Lett.* **93** (2008) 191102
- [20] Pletcher, D., *A First Course in Electrode Processes*. (The Electrochemical Consultancy, London) 1991
- [21] von Helmholtz, H. L. F., *Ann. Physik* **89** (1853) 211
- [22] Gouy, G., *Compt. Rend.* **149** (1909) 654
- [23] Gouy, G., *J. Phys.* **9** (1910) 457
- [24] Champman, D. L., *Phil. Mag.* **25** (1913) 475
- [25] The Southampton Electrochemistry Group, University of Southampton. *Instrumental Methods in Electrochemistry*. (Horwood Publishing, Chichester) 2001
- [26] Stern, O., *Z. Electrochem.* **30** (1924) 508
- [27] Grahame, D. C., *Chem. Rev.* **41** (1947) 441
- [28] Kolb, D. M., *Surf. Sci.* **500** (2002) 722

- [29] Wilms, M., Kruft, M., Bermes, G. and Wandelt, K., *Rev. Sci. Instrum.* **70** (1999) 3641
- [30] Luth, H., *Solid Surfaces, Interfaces and Thin Films*. (Heidelberg, New York; Springer-Verlag) 2010
- [31] Hertz, H., *Sitzungsbericht der Berliner Akademie der Wissenschaften* **9** (1887) & *Ann. Physik* **31** (1887) 983
- [32] Einstein, A., *Ann. der Physik.* **17** (1905) 132
- [33] Bowfield, A. Ph. D. Thesis. The University of Liverpool (2009)



## **Chapter 4**

### **The Si(110) Surface**

## 4.1 Introduction

Semiconductors and semiconductor surfaces have considerable potential in a variety of technological applications including transistor diodes, photovoltaic cells and photon detectors. It is an important aspect of semiconductor research to understand how the electronic and atomic structure of a semiconductor material affects its physical properties. In particular the temperature dependence of semiconductors is of interest since at higher temperatures the conductivity of the material increases.

This research employed a Si(110) wafer of 100  $\mu\text{m}$  thickness as described in section 2.4. This has an anisotropic surface structure ideal for investigations using RAS. The chapter will describe the physical and electronic properties of silicon and then describe how changing the temperature affects the RA spectrum. The results of the RAS studies will be used to determine both the real and imaginary parts of the reflection anisotropy given in equations 2.37 and 2.38.

## 4.2 The Physical Structure of Silicon

Silicon possesses some interesting temperature dependent properties and, as discussed in section 2.2.4, at absolute zero silicon will generally be an insulator and even as the temperature is increased to room temperature,  $\sim 295\text{ K}$ , the conductivity will be relatively low. The low conductivity is due to the low numbers of charge carriers since the numbers of electrons and holes in the material will be equal which is one of the properties of an intrinsic semiconductor. There are ways to increase the number of charge carriers such as by doping the pure silicon with a foreign species such as phosphorus or boron which provide either excess electrons, or excess holes. Any increase in the electron-hole ratio will improve the silicon conductivity. An alternative way of increasing the conductivity is to increase the temperature of the silicon wafer. In this case the electrons will receive an input of thermal energy exciting them from the conduction band to the valence band

leaving behind a hole. As the temperature increases the process will happen more frequently and hence the conductivity of the silicon increases. The temperature dependence of the silicon is the focus of this research but before that is discussed the electronic structure of silicon will be described.

### **4.3 The Electronic Structure of Silicon**

The physical and the electronic structure of silicon are intimately related and changes in the band gap have a strong influence on the properties of the material.

The band structure for silicon is shown in figure 4.1 [1]. It can be seen that the highest occupied state at the  $\Gamma$  point of the Brillouin zone is not in line with the lowest point of the unoccupied band which lies at the X point of the Brillouin zone. Therefore silicon is an indirect band gap semiconductor since for an electron to be excited from the valence band to the conduction band the electron must gain a crystal momentum equivalent to the difference in electron wavevector,  $k$  vector, between the X and  $\Gamma$  points.

This text box is where the unabridged thesis included the following third copyright material:

Cohen, M. L and Chelikowsky, J. R., Electronic Structure and Optical Properties of Semiconductors. (Springer-Verlag, Berlin) 1988

**Figure 4.1: Band structure of silicon calculated using the local pseudopotential (dotted line) and non local pseudopotential (solid line) [1].**

The band structure shown in figure 4.1 has been calculated using the non-local pseudopotential scheme which is an advance on the local pseudopotential calculations which did not show good agreement with experimental techniques [2,3]. Specifically, valence band widths obtained using pseudopotential calculations showed discrepancies with experiment. The full detail of pseudopotential calculations has been discussed by Cohen and Chelikowsky [1] and non-local pseudopotential calculations by [4-6]. In brief, the pseudopotential calculation ‘freezes’ the core electrons and considers only the valence electrons as they move in a weak, one-electron potential. The local pseudopotential assumes the crystal potential is the sum of all local potentials. This restriction is removed in non-local pseudopotential calculations. This causes a much larger number of terms in the calculations but the result is a better agreement with experimental procedures. The more accurate calculation is shown in figure 4.1 by the solid line when

compared to the local potential, shown by the dotted line, especially when plotting the valence band structures.

An experimental technique to determine the energy gap in an intrinsic semiconductor is optical absorption. Since at low temperatures there are not many charge carriers available the semiconductors are transparent to infrared radiation until, at a specific energy, transitions are excited and interband transitions allowed. For direct band gap semiconductors the highest occupied band and lowest unoccupied band have very similar  $k$  vector values since the adsorbed photon has a small wavevector. Hence, the energy required for optical absorption to take place is given by:

$$E_g = \hbar\omega_g \quad (4.1)$$

where  $\omega_g$  is the frequency of the incident light and  $E_g$  is the bandgap. In indirect semiconductors the optical absorption process is more complex since there is not only a vertical transition but also a shift in  $k$  vector values,  $\mathbf{k}_c$ . In all transitions of this form, the wavevector of the photon must be conserved and if this is a purely vertical transition this will not be the case. However, if a phonon with wavevector,  $\mathbf{K}$ , and frequency,  $\Omega$ , is created this will provide the required momentum and satisfy the conservation rules. In this situation, a free electron, a free hole and a phonon of energy  $\hbar\Omega$  are created on absorption of a photon allowing an indirect transition with an energy given in equation 4.2.

$$E_g = \hbar\omega \pm \hbar\Omega \quad (4.2)$$

The plus or minus sign depends on phonon absorption or emission respectively. This also satisfies wavevector conservation rules as shown in equation 4.3.

$$\mathbf{k}(\text{photon}) = \mathbf{k}_c + \mathbf{K} \cong 0 \quad (4.3)$$

Due to the extra phonon factor in indirect transitions this means they are greatly reduced in energy compared to direct transitions.

This difference in energy can be seen in figure 4.2 by comparing the absorption coefficient for  $E_g$  compared to  $E_1$  and  $E_2$ . The transitions  $E_1$  and  $E_2$  are direct transitions, at the L point and X point respectively. As can be seen in figure 4.1 these transitions occur when the conduction band and valence band are almost parallel causing direct transitions with almost equal photon energy with many values of  $k$ . Hence the absorption coefficients at these energies are much larger as observed in figure 4.2. Experimentally the indirect band gap in silicon has been determined to be 1.17 eV at 0 K, reducing to 1.11 eV at 300 K [8] results which are in good agreement with the band structure (solid line) shown in figure 4.1.

This text box is where the unabridged thesis included the following third copyright material:

Fox, M., Optical Properties of Solids. (Oxford University Press, Oxford) 2001

**Figure 4.2: Interband absorption spectrum at 300 K [7].**

#### **4.3.1 The Electronic Structure of Si(110)**

In bulk semiconductors, the covalent bond can be considered to arise from hybridisation between orbitals which are in different bands in a band structure description of the electronic structure. These bonds form from s- and p- orbitals and are given the name  $sp^3$  hybrid bonds which determine the diamond crystal structure found in silicon since they are highly directional. When silicon atoms form bonds to create this crystal structure there will be both bonding and antibonding levels which then extend into the valence and conduction band. However, at the

surface of the low index faces of silicon these hybrid bonds will have different structures as shown schematically in figure 4.3. This figure shows that the (111) surface will have only one dangling hybrid bond per unit cell whereas the (110) and (100) surfaces will each have two. The difference between the (110) and (100) surfaces is that the former has two atoms each with one dangling hybrid bond whereas the latter has one atom with two dangling hybrid bonds [9]. This difference in the number of dangling bonds per surface unit cell for the low Miller index surfaces has a significant effect on the surface tension of the silicon. Since the (111) surface has only one dangling hybrid bond this will have the lowest surface tension whereas the (100) surface will have the highest since each surface atom contains two dangling hybrid bonds. This makes the (111) surface the natural cleavage plane for silicon. However, since this surface is isotropic and is not suitable for use with RAS this research will use the (110) surface which contains the necessary anisotropy.

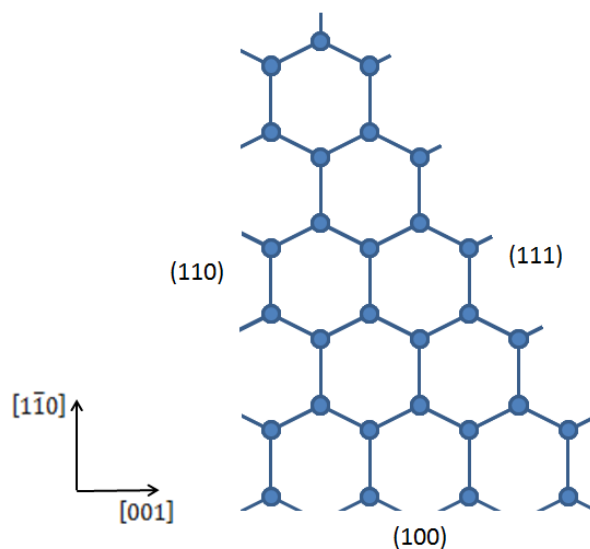


Figure 4.3: Diagram illustrating the three low Miller index faces.

## 4.4 Interband Transitions

As discussed, silicon is an indirect semiconductor although there can also be direct interband transitions at a wide range of energies from 1.00 eV to 12.00 eV.

Ellipsometry and reflectivity techniques together with theoretical calculations, including pseudopotential calculations [1], have been used to develop the current understanding of the silicon electronic band structure. The absorption spectrum has been shown in figure 4.2 for silicon at 300 K which shows two main features corresponding to interband transitions. Furthermore, reflectance measurements can be performed to understand the optical constants  $n$  and  $K$  which are the real and imaginary parts of the complex index of refraction respectively as shown in equation 4.4. These values can then be plotted as a function of energy and will show in more detail any interband transitions that take place.

$$N = n - iK \quad (4.4)$$

The real part,  $n$ , is sometimes called the refractive index and the imaginary part,  $K$ , called the extinction coefficient which is related to the absorption coefficient,  $\alpha$ :

$$\alpha = \frac{4\pi K}{\lambda} \quad (4.5)$$

where  $\lambda$  is the wavelength of the light.

Ellipsometry measurements generally show the complex dielectric function  $\epsilon(\omega)$  as a function of energy rather than the optical  $n$  and  $K$  values. However, as shown in section 2.3.4 the equations required to convert between the optical constants and dielectric functions are relatively straight forward. The equations are repeated below where  $\epsilon_b'$  is the real part of  $\epsilon(\omega)$  and  $\epsilon_b''$  is the imaginary part although they are sometimes labelled  $\epsilon_1$  and  $\epsilon_2$  for real and imaginary parts respectively.

$$\epsilon_b' = n^2 - K^2 \quad (4.6)$$

$$\epsilon_b'' = 2nK \quad (4.7)$$

The spectra for the dielectric functions  $\epsilon_b'$  and  $\epsilon_b''$  are shown in figure 4.4.



This text box is where the unabridged thesis included the following third copyright material:

Vuye, G., Fisson, S., Nguyen Van, V., Wang, Y., Rivory, J. and Abelès, F., *Thin. Solid. Films.* **233** (1993) 166

Aspnes, D. E. and Studna, A. A., *Phys. Rev. B.* **27** (1983) 985

**Figure 4.4: The dielectric function of silicon for (a) real,  $\epsilon_b'$ , and (b) imaginary,  $\epsilon_b''$ , parts at 293 K [10]. The dotted lines show a comparison with the results of Aspnes *et al* [11].**

The labels  $E_0'$ ,  $E_1$ ,  $E_2(X)$  and  $E_2(\Sigma)$  in figure 4.4 show the critical points and are direct interband transitions located in the Brillouin zone. The transitions are defined as critical points as a result of their the amplitude,  $A$ , threshold energy,  $E$ , broadening,  $\Gamma$ , excitonic phase angle,  $\phi$ , and dimensionality,  $n$ , of the structures observed in experiment [12,13] using equation 4.8.

$$\varepsilon(\omega) = C - Ae^{i\phi}(\omega - E + i\Gamma)^n \quad (4.8)$$

Where  $C$  is a constant. As observed in figure 4.4 the  $E_0'$  and  $E_1$  transitions lie very close in energies,  $\sim 100$  meV apart [14]. The  $E_0'$  transition occurs at the  $\Gamma$  point of the Brillouin zone and due to its close proximity with  $E_1$  is nearly degenerated with them. The  $E_1$  transitions take place along the  $\Lambda$  direction. There is a further  $E_1 + \Delta_1$  transition, along the  $\Lambda$  direction that is attributed to a split of  $E_1$  by spin-orbit interaction. However, in silicon the spin-orbit splitting is very small and so is not taken into account in the spectra [15]. The  $E_2$  transitions are more complicated since they are not attributed to a single critical point but of three,  $E_2(1)$ ,  $E_2(2)$  and  $E_2(3)$ , as observed from low field electroreflectance analysis [16]. The  $E_2$  transitions are split up into transitions labelled  $E_2(X)$  and  $E_2(\Sigma)$  at  $\sim 4.32$  eV and  $\sim 4.54$  eV respectively. The  $X$  and  $\Sigma$  symbols represent transitions along the  $X$  or  $\Sigma$  directions

of the Brillouin zones [6,17]. There is a further  $E_1'$  transition not shown in figure 4.4 at an energy of  $\sim 5.50$  eV that is attributed to a transition between the valence and conduction band along the  $\Lambda$  direction. This differs from the  $E_1$  transition along the same direction because the  $E_1'$  transition corresponds to a higher conduction band. Since this transition is on the edge of what can be measured within this research the focus will be on the remaining transitions.

#### **4.4.1 Temperature Dependence of Interband Transitions**

An important feature of the interband transitions in silicon is their dependence on temperature. This is because numerous applications of semiconductor technology rely on either a specific temperature or specific energy range. For example, the optimal conditions for growth of dielectric films are high temperatures. When the temperatures of semiconductor materials are increased there is a shift in energy of the electronic states [18] which can be monitored using similar techniques to those that have been used to determine the critical points. Since the indirect transition between an occupied state at the  $\Gamma$  point and the unoccupied state at the X point of the Brillouin zone, labelled  $E_g$  in figure 4.2, has a lower absorption coefficient than the direct transitions, labelled  $E_1$  and  $E_2$ , only the temperature dependence of the direct transitions will be discussed in this research. With increasing temperature these transitions also experience an increased lifetime broadening which is observed in the spectrum as a broader peak when compared to lower temperature spectrum. As a result of the uncertainty principle, the initial and final state energies are not precisely defined and therefore the energy levels cannot be specified exactly. The width of a transition depends on both the initial and final states and only when both states have long lifetimes and well defined energies will the spectral lines be narrow [19].

Lifetime broadenings corresponding to Auger type decays are very small unless the electrons or holes have an energy, with respect to the band edge, of  $\sim 16.00$  eV, the plasma frequency. Up to  $\sim 3.00$  eV the broadening from Auger decay is only

$\sim 10$  meV [20] and these processes are almost temperature independent. The direct transitions observed in silicon,  $E_0'$ ,  $E_1$  and  $E_2$ , possess initial and final state energies less than 3.00 eV with lifetime broadenings of more than  $\sim 10$  meV which are temperature dependent. Consequently the Auger process does not influence the lifetime broadening and the temperature dependence must arise from other processes, such as the electron-phonon interaction.

The electron-phonon interaction is highly temperature dependent since at higher temperatures there are more phonons present which scatter the electrons at a faster rate than at lower temperatures. This scattering causes the electrical resistivity to increase, for example, for copper at 273 K the electrical resistivity is  $1.55 \mu\Omega\text{cm}^{-1}$  whereas at 373 K this has increased to  $2.28 \mu\Omega\text{cm}^{-1}$  [8]. A phonon refers to the quantum unit of a crystal vibration in the same way as a photon quantises light and a plasmon quantises plasma oscillations. The electron-phonon contribution is calculated in theoretical work by splitting the contribution into the Debye-Waller terms [21] and the 'self-energy' terms. These have been found [22-24] to have roughly the same magnitude so both need to be considered. The Debye-Waller terms focus on the phonon amplitude and not the specific phonon involved whereas the 'self-energy' terms are different for each phonon at an electronic state. The method in which these terms arise is discussed extensively by Allen *et al* [25] for silicon and germanium.

In addition to the electron-phonon interaction there is also a contribution from the thermal expansion which is a factor in the temperature dependence of the critical points. This is calculated from the dependence on the band structure using the respective expansion coefficients [26].

The temperature dependence of the complex dielectric function of silicon has been studied using ellipsometry techniques up to a temperature of 1200 K [10,27-29]. Figure 4.5 shows the real,  $\epsilon_b'$ , and imaginary,  $\epsilon_b''$ , parts of the dielectric function of silicon at a range of temperatures with the critical points labelled. As observed in

figure 4.5 the transition energies all reduce as the temperature is increased and also decrease in magnitude. In particular the  $E_0'$  and  $E_1$  transition peaks are unobservable at higher temperatures in the  $\epsilon_b''$  spectra and more strongly resemble a high energy cut off shoulder in the  $\epsilon_b'$  spectra. As expected figure 4.5 shows all transitions become broadened in width which is a consequence of the increased electron-phonon interaction at higher temperatures.

This text box is where the unabridged thesis included the following third copyright material:

Jellison, Jr. G. E. and Modine, F. A., *Phys. Rev. B.* **27** (1983) 7466

**Figure 4.5: The real,  $\epsilon_b'$ , and imaginary,  $\epsilon_b''$ , parts of the dielectric function at a range of energies from 10 K to 972 K [27].**

The peak intensity of the interband transitions can be plotted as a function of temperature to determine a value for the temperature coefficient. Lautenschlager *et al* [28] observed that the temperature dependence of the peak intensity can be

fitted to particular equations. The Varshni equation [30], shown in equation 4.9, can successfully fit the data over a wide range of energies, 30 K-820 K.

$$E(t) = E(0) - \frac{\alpha T^2}{T + \beta} \quad (4.9)$$

where  $E(0)$  is related to the initial peak energy position,  $\alpha$  is the temperature coefficient and  $\beta$  is associated with the Debye temperature [30]. Generally a linear least squares fitting program can be used to determine  $E(0)$ ,  $\alpha$  and  $\beta$  [27]. However, for a more narrow temperature range, 350 K-820 K, the data can be fitted to the more linear form, shown in equation 4.10. In this temperature range the  $E_0'$  and  $E_1$  transitions cannot be defined individually but can be fitted to this linear model.

$$E(T) = E_C - \lambda T \quad (4.10)$$

Where  $\lambda$  is the temperature coefficient and  $E_C$  is based around the initial peak energy. The values for the temperature coefficients for silicon over the temperature ranges (a) 30 K-820 K and (b) 350 K-820 K are shown in table 4.1.

(a)	<b>Interband Transition</b>	<b>Temperature Coefficient, <math>\alpha</math> (<math>10^{-4}</math> eVK<math>^{-1}</math>)</b>
	$E_0'$	3.5 (3.8)
	$E_1$	4.7 (1.7)
	$E_2(X)$	2.9 (7)
(b)	<b>Interband Transition</b>	<b>Temperature Coefficients, <math>\lambda</math> (<math>10^{-4}</math> eVK<math>^{-1}</math>)</b>
	$E_1$	4.1 (3)

**Table 4.1: Temperature coefficient between (a) 30 K to 820 K and (b) 350 K and 820 K [28]. The 95% confidence limit is shown in brackets.**

These results of Lautenschlager *et al* [28] show good agreement with other work [10,29].

## 4.5 The Reflection Anisotropy Spectroscopy of the Si(110) Surface

The remainder of this chapter will present the RA spectra for the Si(110) surface over a temperature range of 296 K to 623 K in air. It is assumed there will be an oxide layer present on the Si(110) surface which will be discussed later. The equipment used to heat the silicon wafer is a Linkham heating stage which has a maximum temperature of ~650 K and an accuracy of  $\pm 0.1$  K. Due to the 100  $\mu\text{m}$  thickness of the silicon wafer there will be a discrepancy in the temperature of the heating stage and the temperature of the surface. To determine this difference an infrared thermometer was used to measure the temperature of the surface which gave good consistency to ~5 % of the value given on the heating stage. Since this research focuses on the change in RA profile as the temperature changes this error is acceptable. The research in this chapter will use a heating, or cooling, rate of  $1 \text{ Kmin}^{-1}$ .

As discussed in sections 2.4 and 3.2, RAS can measure both the real,  $Re\left(\frac{\Delta r}{r}\right)$ , and imaginary,  $Im\left(\frac{\Delta r}{r}\right)$ , parts of the fractional anisotropy of the surface as shown in equation 2.24 and both these RA profiles will be presented in this chapter. Experimentally the real and imaginary parts are measured at different frequencies as described by equations 3.38 and 3.39. As a consequence, to maximise the appropriate Bessel function the retardation amplitude introduced by the PEM is set to 3.054 radians for  $Re\left(\frac{\Delta r}{r}\right)$  and 1.850 radians for  $Im\left(\frac{\Delta r}{r}\right)$ .

### 4.5.1 The $Re\left(\frac{\Delta r}{r}\right)$ part of the RA spectra as a function of temperature

The RA profile of silicon at room temperature, 296 K, is shown in figure 4.6. As can be seen in the figure, the spectrum is dominated by two peaks labelled,  $E_1$  at an energy of 3.52 eV and  $E_2$  at 4.36 eV.

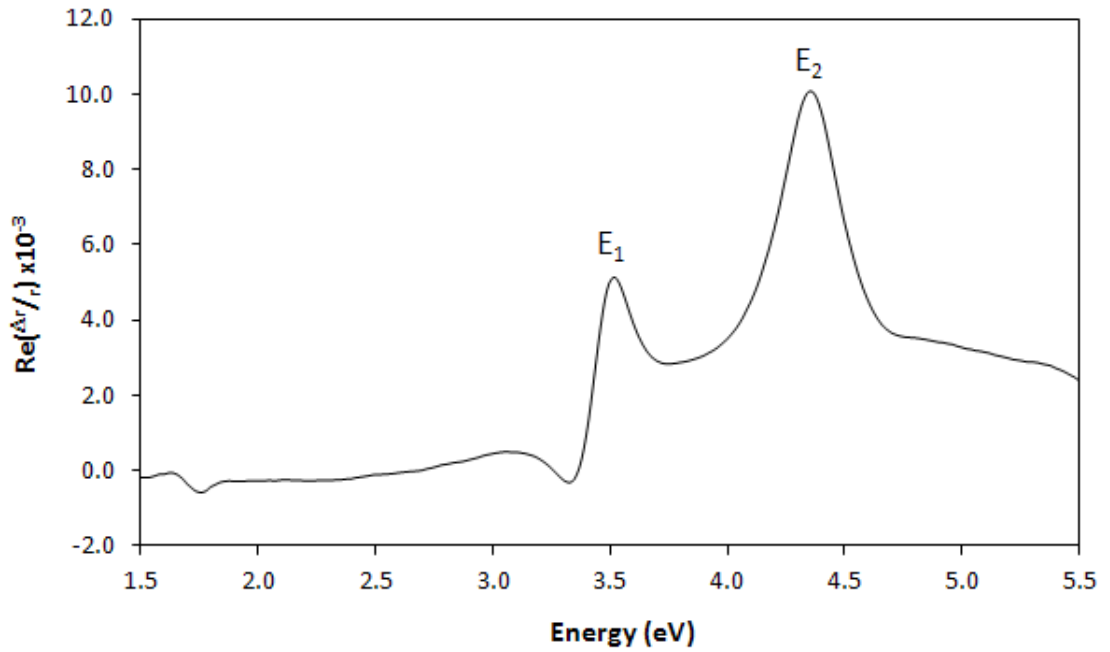


**Figure 4.6: RA profile of Si(110) at 296 K with transitions labelled  $E_1$  and  $E_2$ .**

These transitions are attributed to the same  $E_1$  and  $E_2$  transitions as discussed in section 4.4 since their respective energies are consistent with those observed using ellipsometry techniques. Similar features at 3.40 eV and 4.20 eV are also observed by Rossow *et al.* in work which studied various lineshapes of surface induced optical anisotropy using RAS [31]. The analysis presented in this work also discusses how the RA spectrum can resemble ‘derivative-like lineshapes’ and ‘dielectric-function-like lineshapes’ which, although not discussed in this thesis, could prove to be an important aspect when trying to simulate the RA spectrum in future work.

At 296 K, the temperature is too high for the  $E_0'$  transitions to be observed independently from the  $E_1$  transitions using RAS and consequently only the  $E_1$  transition is labelled. Similarly the  $E_2(X)$  and  $E_2(\Sigma)$  transitions cannot be separated and are annotated by the more general  $E_2$  label.

The RA profile of silicon at a range of temperatures is shown in figure 4.7. In agreement with ellipsometry techniques there is a reduction in peak intensity as the temperature is increased along with a decrease in peak energy. For the  $E_1$

transition, the peak energy decreases by  $\sim 0.10$  eV and the  $E_2$  transition peak energy decreases by  $\sim 0.07$  eV over this temperature range.

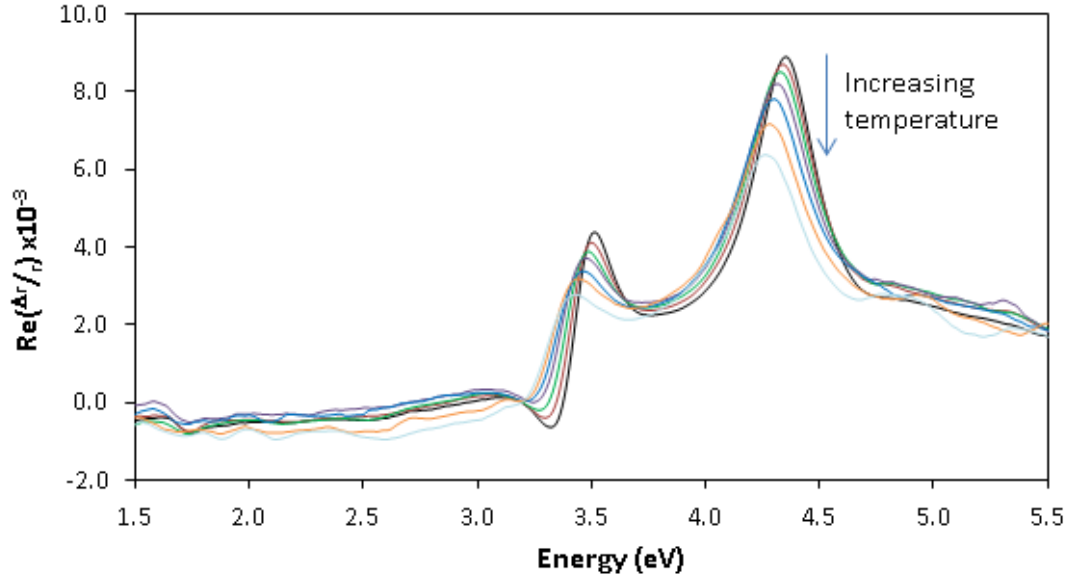


**Figure 4.7:** RA profile of Si(110) at 323 K (black line), 373 K (red line), 423 K (green line), 473 K (purple line), 523 K (blue line), 573 K (orange line) and 623 K (light blue line).

The dependence of the RA peak energy with temperature is shown in figure 4.8 for the  $E_1$  transition and  $E_2$  transition respectively. The peak positions are determined by eye which is consistent throughout the rest of the thesis. The theoretical line is calculated using the linear dependence equation, equation 4.10, since the temperature range in these experiments are too narrow to use the Varshni equation, equation 4.9.



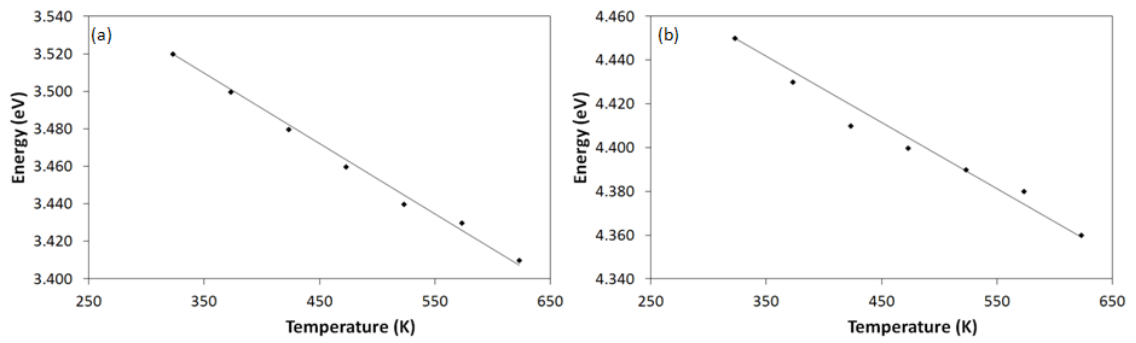


**Figure 4.8: RA peak energy as a function of temperature for (a) the  $E_1$  transition and (b) the  $E_2$  transition.**

Temperature (K)	Temperature Coefficients ( $10^{-4} \text{ eV K}^{-1}$ )	
	$E_1$ transition	$E_2$ transition
<b>323-623</b>	$\sim 4.0 \pm 0.2$	$\sim 3.0 \pm 0.2$

**Table 4.2: Temperature coefficients,  $\alpha$ , for the transitions in the RA spectra. The errors are estimated by performing multiple measurements and using the standard deviation.**

The values for the temperature coefficient,  $\alpha$ , for the  $E_1$  and  $E_2$  transitions are shown in table 4.2 and show good agreement with those in table 4.1.

It has been observed [10,27,28] that there is an oxide layer on the silicon surface at room temperature,  $\sim 293$  K. Although this oxide layer is likely to be present in this research it is expected to be very thin and is assumed to be structurally isotropic so therefore unlikely to affect the results with any significance. This is further confirmed by comparing the ambient RA spectra shown in the research to the clean Si(110) surface in UHV conditions [32] which show very good agreement. Exposing the silicon to higher temperatures may affect the thickness of this oxide layer. However, figure 4.9 shows the RA profile when the temperature is heated to 323 K along with an almost identical profile obtained when the silicon has cooled from 623 K back to 323 K showing any oxide layer has a negligible effect on the RA profiles.

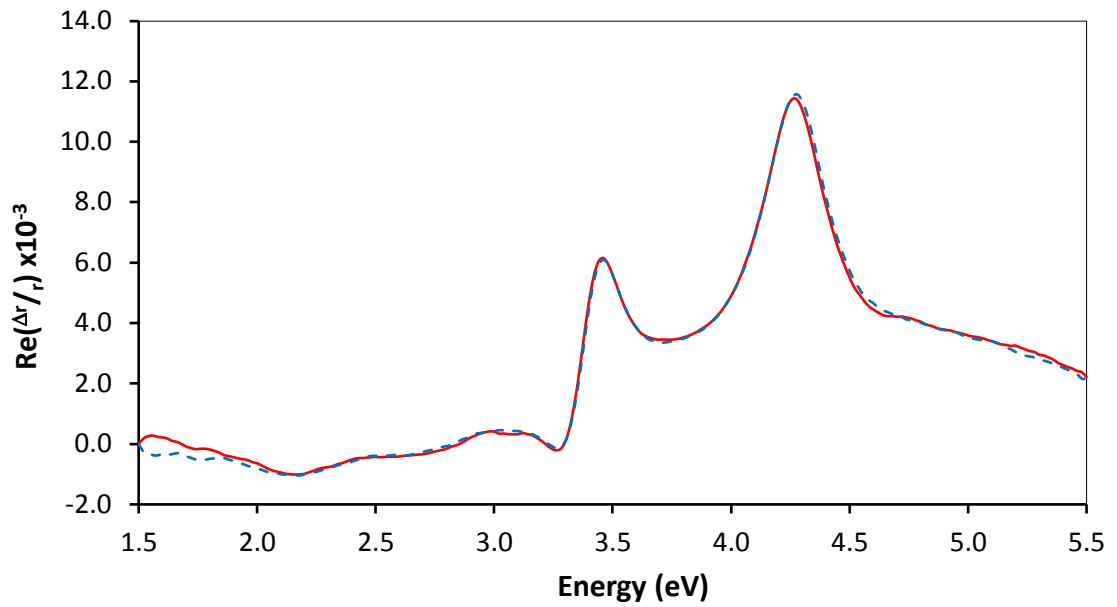
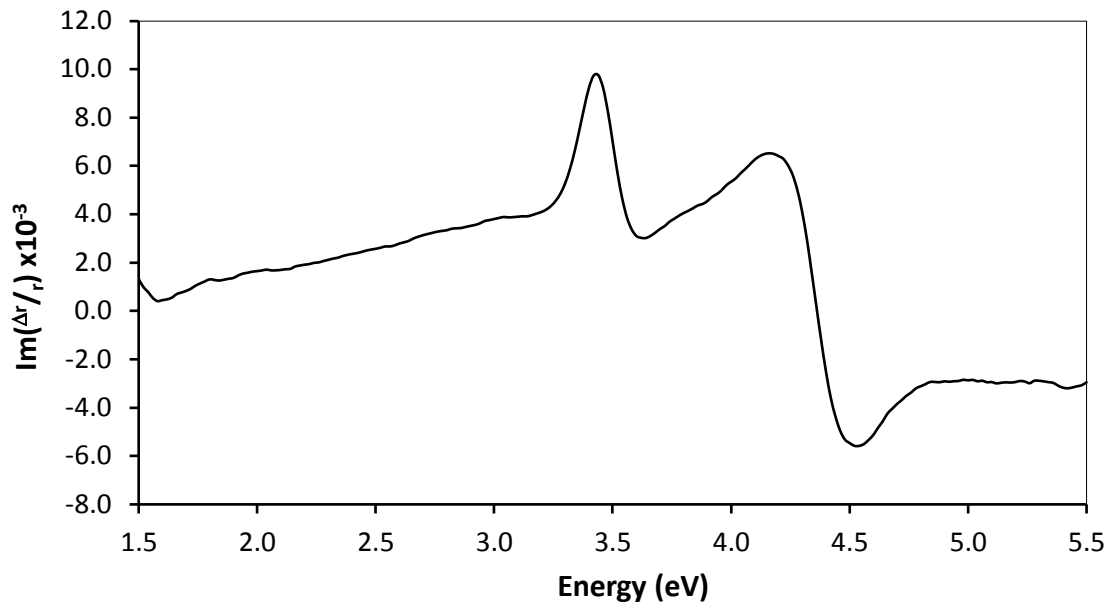


Figure 4.9: RA profile at 323 K for the initial spectrum (red line) and after the surface has been cooled from 623 K (blue dashed line)

#### 4.5.2 The $Im\left(\frac{\Delta r}{r}\right)$ part of the RA spectra as a function of temperature

The imaginary part of the RA spectra is shown in figure 4.10 at room temperature, 293 K. The spectrum is different to that of the real part although the transitions are observed around the same energies. There is a strong positive feature at 3.42 eV followed by a positive increase into another feature at 4.24 eV. Finally the spectrum tends into a negative peak at 4.52 eV. Another aspect of this profile is that it is featureless at energies lower than ~3.00 eV. This is expected as silicon is transparent at energies below this energy as can be seen in the absorption spectrum in figure 4.2.



**Figure 4.10:** RA spectrum for  $Im\left(\frac{\Delta r}{r}\right)$  of Si(110) at 293 K.

The peak at 3.42 eV is attributed to the  $E_1$  transition along the  $\Lambda$  direction of the Brillouin zone. The further peaks may be attributed to the  $E_2$  transition which occurs along the X or  $\Sigma$  directions.

The dependence of the imaginary part of the RA spectra on temperature is shown in figure 4.11. As the temperature is increased the peaks show a decrease in intensity and also a shift in peak position to lower energies. In this case the peak energy for the  $E_1$  transition shows a decrease in energy of  $\sim 0.12$  eV with the peak at 4.52 eV decreasing by  $\sim 0.10$  eV. At some of the higher temperatures some of the spectra become less smooth which can happen due to external factors such as vibrations. However, it could also be due to the surface being less stable at these higher temperatures.

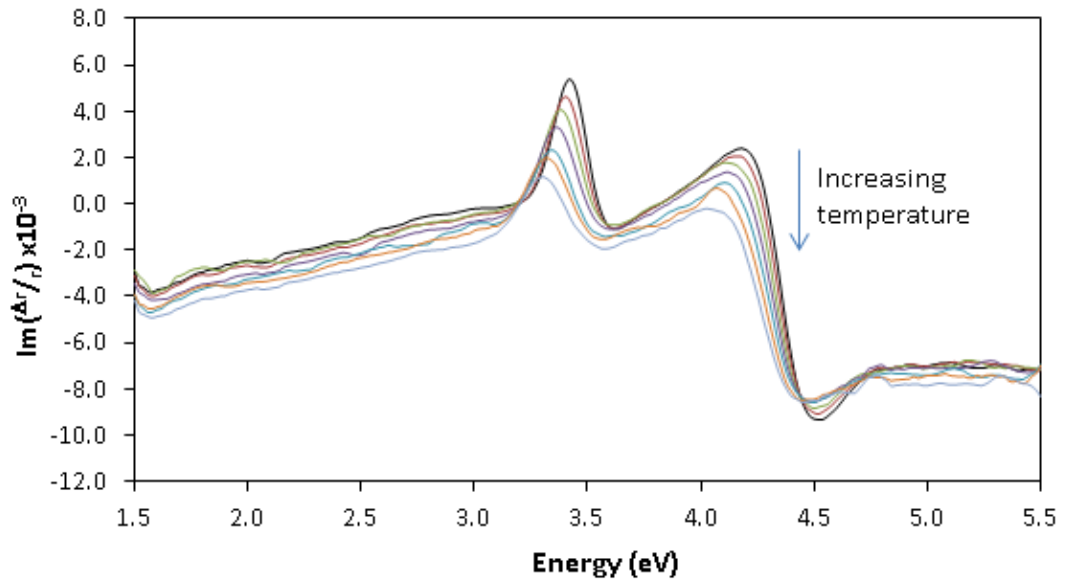


**Figure 4.11:** RA spectra for  $Im\left(\frac{\Delta r}{r}\right)$  of Si(110) at 323 K (black line), 373 K (red line), 423 K (green line), 473 K (purple line), 523 K (blue line), 573 K (orange line) and 623 K (light blue line).

The temperature dependence of the peak energy is shown in figure 4.12 for the three peaks along with table 4.3 showing the temperature dependence. As with  $Re\left(\frac{\Delta r}{r}\right)$  the theoretical lines are calculated using the linear temperature coefficient equation given in equation 4.10.

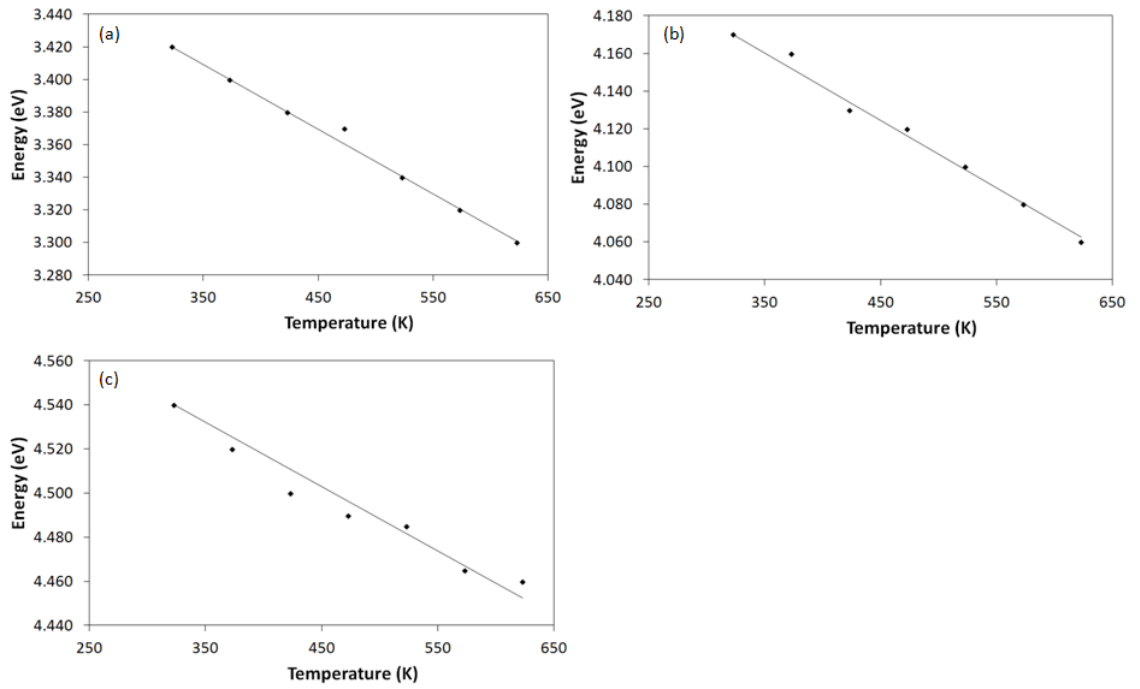


**Figure 4.12:** RA peak energy as a function of temperature for energies (a) ~3.40 eV, (b) ~4.20 eV and (c) ~4.50 eV in the  $Im\left(\frac{\Delta r}{r}\right)$  spectra.

Temperature (K)	Temperature Coefficients ( $10^{-4}$ eVK $^{-1}$ )		
	At ~3.40 eV	At ~4.20 eV	At ~4.50 eV
323-623	$3.97 \pm 0.08$	$3.58 \pm 0.08$	$2.91 \pm 0.10$

**Table 4.3:** Table to show the temperature coefficient,  $\alpha$ , for  $Im\left(\frac{\Delta r}{r}\right)$  for Si(110). The errors are estimated by performing multiple measurements and using the standard deviation.

The temperature coefficients calculated from the  $Im\left(\frac{\Delta r}{r}\right)$  spectra can be compared to those from the  $Re\left(\frac{\Delta r}{r}\right)$  spectra to determine how the energy of the transitions contributes to the imaginary spectra. In the  $Re\left(\frac{\Delta r}{r}\right)$  spectra the  $E_1$  transition has an energy of 3.50 eV and ellipsometry studies showed the transition, at room temperature, to be at ~3.40 eV which is consistent with the  $Im\left(\frac{\Delta r}{r}\right)$  spectra where the room temperature peak is positioned at 3.42 eV. All these peaks then have a temperature coefficient ~4.00 eVK $^{-1}$  so the transition at 3.42 eV is attributed to the  $E_1$  transition in the  $\Lambda$  direction of the Brillouin zone. The transitions at higher

energies in the  $Im\left(\frac{\Delta r}{r}\right)$  spectra have temperature coefficients within  $0.5 \text{ eV K}^{-1}$  of the value given in table 4.1. Although the temperature coefficient for the peak at  $\sim 4.50 \text{ eV}$  is a more accurate value than the temperature coefficient at  $\sim 4.30 \text{ eV}$ . This could be because the higher energy feature has a symmetrical peak shape whereas the peak at  $\sim 4.30 \text{ eV}$  is not symmetrical. The asymmetrical peak shape can cause problems when calculating the temperature dependence as it is more difficult to judge how the peak shifts with increasing temperature. Alternatively the features at  $\sim 4.30 \text{ eV}$  and  $\sim 4.50 \text{ eV}$  are due to the  $E_2(X)$  and  $E_2(\Sigma)$  transitions respectively and the higher temperature coefficient found for the  $E_2(X)$  is due to the differences in the specific techniques used to obtain the spectra. In ellipsometry experiments  $\epsilon_s''$  is measured whereas in RAS,  $Im\left(\frac{\Delta r}{r}\right)$  is measured.

Another argument to explain the differences in the higher energy temperature coefficients is the role the Kramers-Kronig relations play. Simply, these state that where there is a peak present in the real part of the spectrum, there will be a related feature in the imaginary spectrum. When more peaks are added in a single spectrum the Kramers-Kronig relations become more complicated and therefore the temperature coefficient observed for  $E_2$  in the real spectrum may be a combination of both the temperature coefficients observed at  $4.30 \text{ eV}$  and  $4.50 \text{ eV}$  in the imaginary spectrum.

## 4.6 The Complex Anisotropic Surface Dielectric Function of Si(110)

The final part of this chapter will discuss the anisotropic surface dielectric function of silicon. The dielectric function,  $\epsilon$ , discussed thus far is the substrate dielectric function of silicon in terms of the real,  $\epsilon_b'$ , or imaginary parts,  $\epsilon_b''$  and has an isotropic structure. Thus, this value does not change for any of the low Miller index surfaces. However, it is expected that there will be a finite anisotropic surface layer with an associated dielectric function that can be captured in the three layer

model. This is the anisotropic surface dielectric function and given in equation 4.11. The anisotropic surface dielectric function provides an enhanced understanding of surface optical processes and surface specific information such as surface termination. The anisotropic surface dielectric function is unique to the orientation of the crystal planes at the surface with respect to the bulk crystal axes. As a consequence the results for the anisotropic surface dielectric function presented in this research are specific to the (110) surface of silicon.

$$\Delta\epsilon_s = \Delta\epsilon'_s - i\Delta\epsilon''_s \quad (4.11)$$

Where  $\Delta\epsilon'_s = \epsilon'_{sx} - \epsilon'_{sy}$  and  $\Delta\epsilon''_s = \epsilon''_{sx} - \epsilon''_{sy}$  as shown in a schematic diagram, figure 2.11, in chapter 2. These are related to the real and imaginary parts of the RA spectra as shown in equations 2.37 and 2.38. These equations are repeated below:

$$Re\left(\frac{\Delta r}{r}\right) = \frac{4\pi d}{\lambda[(\epsilon'_b - 1)^2 + \epsilon''_b{}^2]} \{(\epsilon'_b - 1)\Delta\epsilon''_s - \epsilon''_b \Delta\epsilon'_s\} \quad (4.12)$$

$$Im\left(\frac{\Delta r}{r}\right) = \frac{4\pi d}{\lambda[(\epsilon'_b - 1)^2 + \epsilon''_b{}^2]} \{(\epsilon'_b - 1)\Delta\epsilon'_s - \epsilon''_b \Delta\epsilon''_s\} \quad (4.13)$$

Where  $\lambda$  is the wavelength of the incident light and  $d$  is the thickness of the anisotropic surface layer.

Since both the  $Re\left(\frac{\Delta r}{r}\right)$  and  $Im\left(\frac{\Delta r}{r}\right)$  quantities are known from the results of the RAS experiments presented earlier and the  $\epsilon'_b$  and  $\epsilon''_b$  functions are well known it is possible for the surface dielectric functions,  $\Delta\epsilon'_s$  and  $\Delta\epsilon''_s$ , to be determined. The Vuye *et al* [10] data for the  $n$  and  $K$  values of silicon are used as the  $\epsilon'_b$  and  $\epsilon''_b$  quantities calculated by the conversion factors given in equations 2.21 and 2.22. This data was chosen as it most accurately represents the temperature range used in this research and has good agreement with other work [28]. The  $\epsilon'_b$  and  $\epsilon''_b$  are shown using the data from Vuye *et al* at temperatures to coincide with the RAS data.

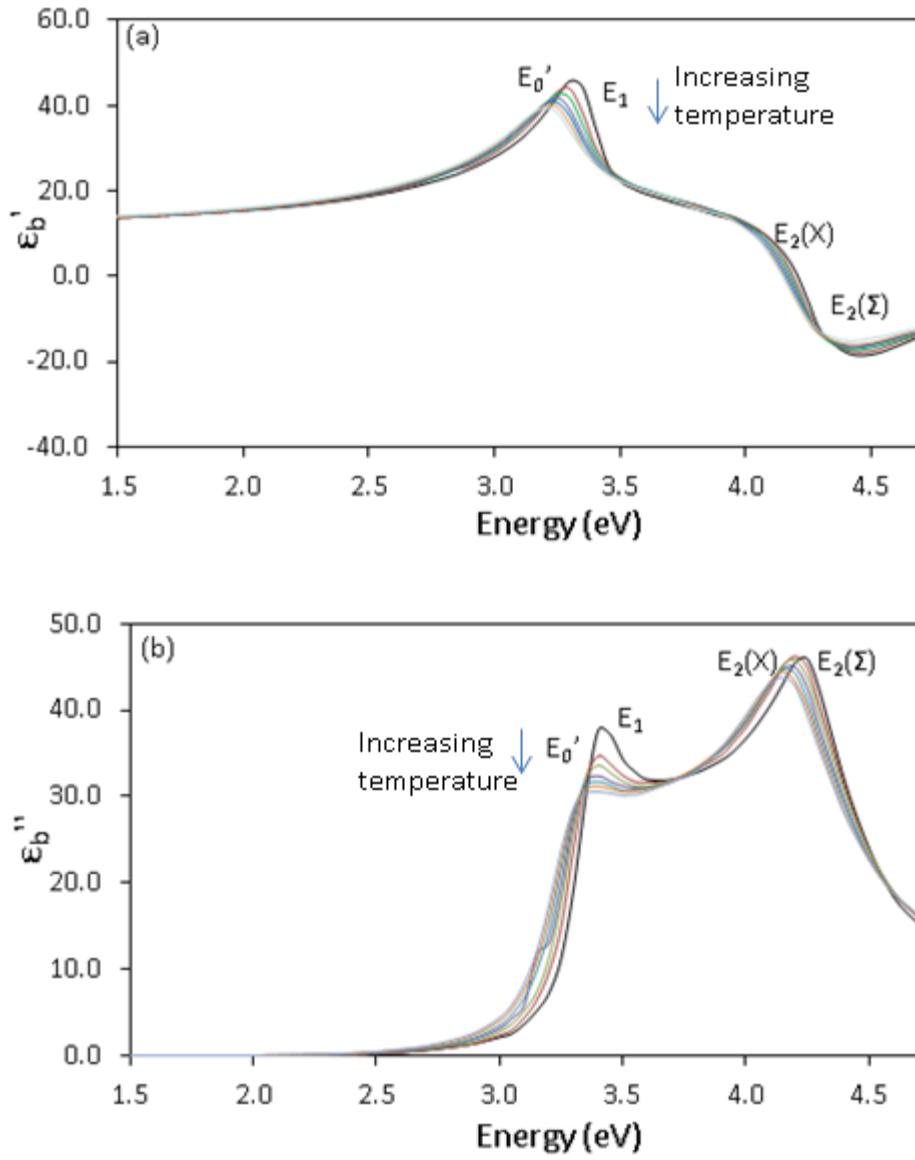


**Figure 4.13: Dielectric function of silicon for (a) the real part,  $\epsilon'_b$ , and (b) the imaginary part,  $\epsilon''_b$  with the transitions labelled. Spectra taken at 293 K (black line), 373 K (red line), 423 K (green line), 473 K (purple line), 523 K (blue line), 573 K (orange line) and 623 K (light blue line).**

By solving equations 4.12 and 4.13 as simultaneous equations the values of the surface dielectric functions can be determined as shown in equations 4.14 and 4.15.

$$\Delta\epsilon'_s = \frac{(\epsilon'_b - 1)Im\left(\frac{\Delta r}{r}\right) - \epsilon''_b Re\left(\frac{\Delta r}{r}\right)}{A[\epsilon''_b{}^2 + (\epsilon'_b - 1)^2]} \quad (4.14)$$



$$\Delta\epsilon_s'' = \frac{(\epsilon_b' - 1)Re\left(\frac{\Delta r}{r}\right) - \epsilon_b''Im\left(\frac{\Delta r}{r}\right)}{A[\epsilon_b''^2 + (\epsilon_b' - 1)^2]} \quad (4.15)$$

where:

$$A = \frac{4\pi d}{\lambda[(\epsilon_b' - 1)^2 + \epsilon_b''^2]} \quad (4.16)$$

The value  $d$ , for the thickness of the surface layer, has been given a value of 1 nm for these calculations.

The anisotropic surface dielectric functions  $\Delta\epsilon_s'$  and  $\Delta\epsilon_s''$  are shown in figures 4.14 and 4.15 along with their dependence with temperature. These spectra differ from those of the real and imaginary parts of the bulk dielectric functions,  $\epsilon_b'$  and  $\epsilon_b''$  in figure 4.13. However, as the temperature is increased the peaks observed in the spectra of figures 4.14 and 4.15 reduce in intensity and move to lower energies as was observed for the bulk dielectric functions.

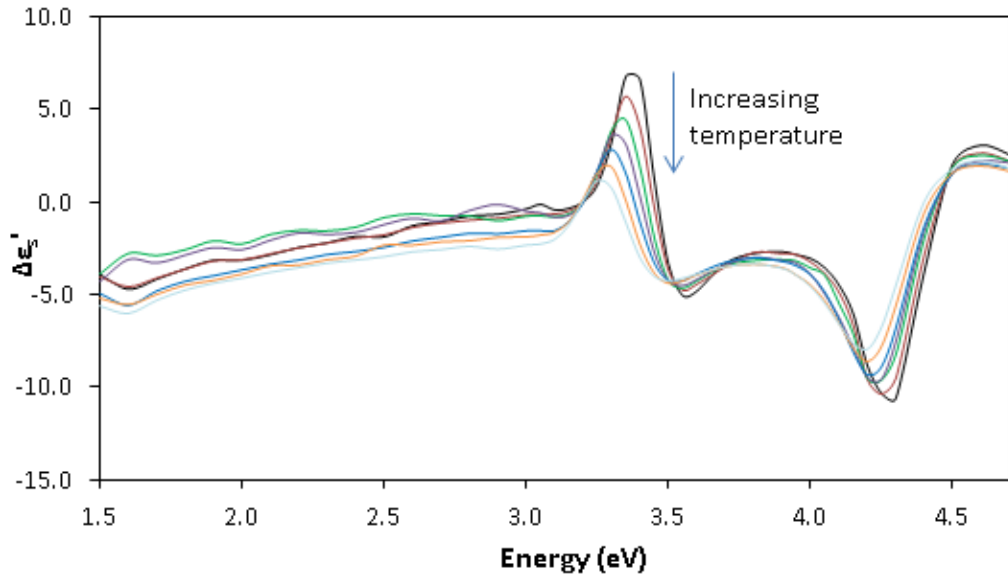


**Figure 4.14:** Real part of the surface dielectric function,  $\Delta\epsilon_s'$ . Spectra taken at 293 K (black line), 373 K (red line), 423 K (green line), 473 K (purple line), 523 K (blue line), 573 K (orange line) and 623 K (light blue line).

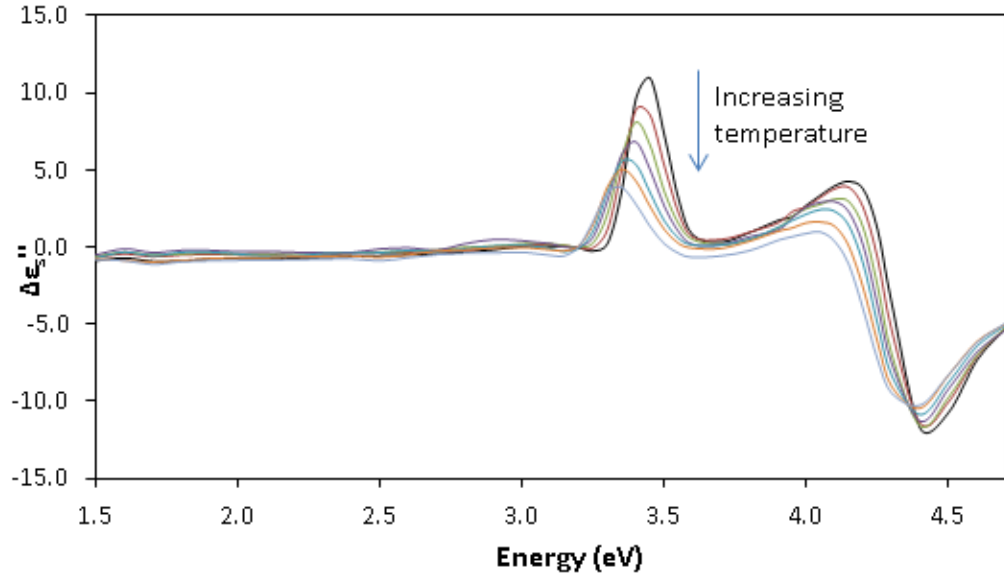


**Figure 4.15: Imaginary part of the surface dielectric function,  $\Delta\epsilon_s''$ . Spectra taken at 293 K (black line), 373 K (red line), 423 K (green line), 473 K (purple line), 523 K (blue line), 573 K (orange line) and 623 K (light blue line).**

In the  $\Delta\epsilon_s'$  spectrum at 293 K there is a feature at 3.35 eV followed by a more negative feature at  $\sim 3.50$  eV which leads into a more prominent negative feature peaking at 4.30 eV. The  $\Delta\epsilon_s''$  spectrum at the same temperature shows an initial positive peak at 3.40 eV followed by a less intense positive feature at  $\sim 4.20$  eV leading to a large negative feature at 4.40 eV. These peaks are assigned to be associated with transitions  $E_1$  and  $E_2$  as shown in table 4.4. These values are shown alongside the bulk dielectric transition energies for comparison. The table shows that the two real parts of the bulk and surface dielectric functions show good agreement. The imaginary parts of the bulk and surface dielectric functions show some discrepancy in the peak energy transitions as the transitions observed in the surface are slightly higher than those in the bulk. This could be due to the anisotropy present in the surface but not the bulk. Also, since the anisotropic surface dielectric function is being measured the optical response will differ in the two principal crystal directions, the  $[1\bar{1}0]$  and  $[001]$  directions, which could affect the transition energy [33]. Furthermore, the  $\Delta\epsilon_s''$  spectrum is very close to zero at energies below  $\sim 3.00$  eV. This is expected since silicon is transparent at these

energies. The  $\Delta\epsilon_s'$  spectrum, although featureless, shows some small oscillations at energies below  $\sim 3.00$  eV which were also present in the  $Im\left(\frac{\Delta r}{r}\right)$  spectra and are thought to be due to the surface being less stable at higher temperatures and more prone to external fluctuations. In conjunction with this there can be a peak that presents itself some of the RA spectra at  $\sim 2.70$  eV which arises from a peak in the output of the Xe lamp which, due to the less than perfect optical elements, does not cancel completely in the ratio in equation 3.1.

	Transition Energy (eV)				
	$E_1$	$E_2$		$E_1$	$E_2$
$\epsilon_b'$	3.32	4.30	$\Delta\epsilon_s'$	3.35	4.30
$\epsilon_b''$	3.40	4.30	$\Delta\epsilon_s''$	3.45	4.40

**Table 4.4:** The peak energy of transitions  $E_1$  and  $E_2$  for the real and imaginary parts of the bulk dielectric function,  $\epsilon_b'$  and  $\epsilon_b''$ , and surface dielectric functions,  $\Delta\epsilon_s'$  and  $\Delta\epsilon_s''$ . The errors in this table are all 0.02 eV which is the smallest unit shown when observing the peaks by eye.

The temperature coefficient of the  $E_1$  and  $E_2$  transitions in the surface dielectric function spectra are shown in figures 4.16 and 4.17 fitted to the linear temperature equation given in equation 4.10.

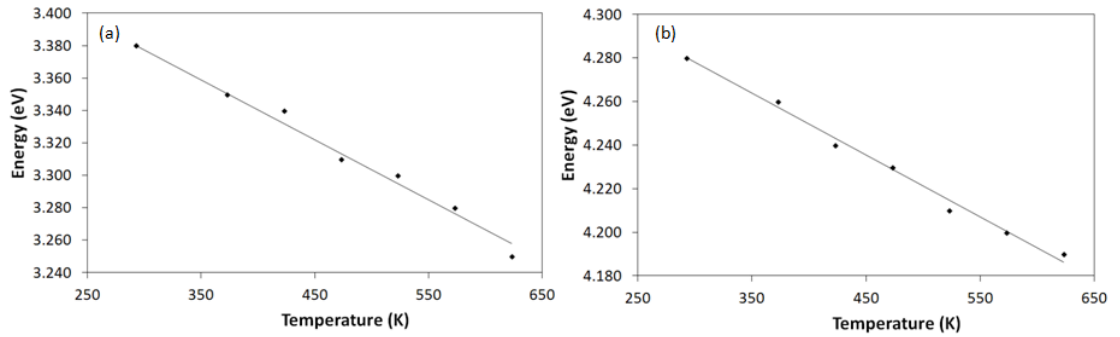


**Figure 4.16:** RA peak energy as a function of temperature for (a) the  $E_1$  transition and (b) the  $E_2$  transition for the  $\Delta\epsilon_s'$  function.

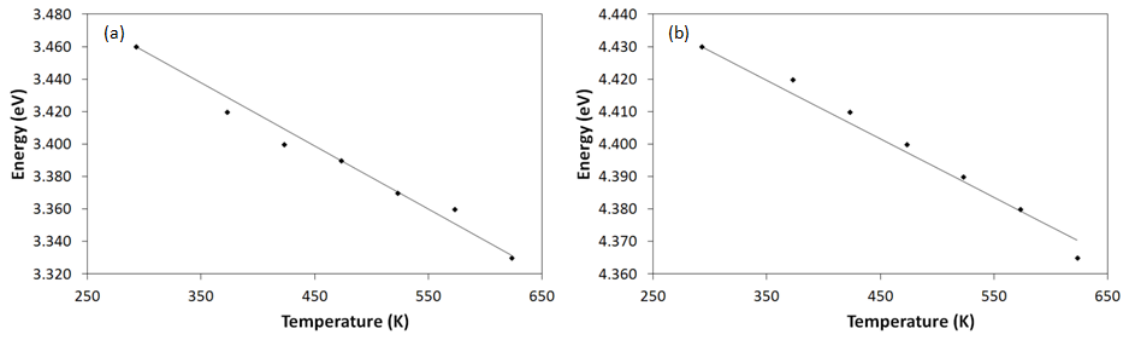


**Figure 4.17: RA peak energy as a function of temperature for (a) the  $E_1$  transition and (b) the  $E_2$  transition for the  $\Delta\epsilon_s''$  function.**

The tabulated temperature coefficients for the surface dielectric functions are then shown in table 4.5, alongside the coefficients for the bulk dielectric functions for comparison. The bulk temperature coefficients are split up into the real and imaginary parts,  $\epsilon_b'$  and  $\epsilon_b''$ . The blank spaces in the table are where the temperature coefficients cannot be calculated from the spectra. For example, there is no  $E_2$  transition temperature coefficient in the  $\epsilon_b'$  spectrum as there is no definite peak at  $\sim 4.30$  eV in the  $\epsilon_b'$  spectrum. The temperature coefficients for the bulk and surface dielectric functions fit well for the  $E_1$  transition but do not show complete agreement for the  $E_2$  transition. The discrepancy could be because in the bulk there is a centrosymmetric structure whereas the surface is anisotropic. This contrast in structures will mean the electronic band structure of the bulk and surface will not be identical which could account for different temperature coefficients.

	Temperature Coefficients ( $10^{-4} \text{ eVK}^{-1}$ )				
	$E_1$	$E_2$		$E_1$	$E_2$
$\epsilon_b'$	$3.32 \pm 0.08$		$\Delta\epsilon_s'$	$3.33 \pm 0.08$	$3.03 \pm 0.08$
$\epsilon_b''$	$2.91 \pm 0.07$	$2.87 \pm 0.07$	$\Delta\epsilon_s''$	$3.33 \pm 0.08$	$1.81 \pm 0.07$

**Table 4.5: Temperature coefficients,  $\alpha$ , for the transitions  $E_1$  and  $E_2$  for the surface dielectric functions,  $\Delta\epsilon_s'$  and  $\Delta\epsilon_s''$  functions along with the bulk dielectric functions  $\epsilon_b'$  and  $\epsilon_b''$ . The errors are estimated by performing multiple measurements and using the standard deviation.**

## 4.7 Summary

This chapter has described the RAS studies of a Si(110) surface at room temperature and as it is heated up to a temperature of 623 K. The chapter began by discussing previous experiments and how the surface behaves at varying temperatures. The first results presented were those of the  $Re\left(\frac{\Delta r}{r}\right)$  part of the RA spectra and the transitions  $E_1$  and  $E_2$  have been observed. The temperature coefficients associated with these transitions show good agreement with previous experimental and theoretical data.

The chapter went on to present data for the  $Im\left(\frac{\Delta r}{r}\right)$  part of the RA spectra. The transitions  $E_1$  and  $E_2$  were identified in the spectra the temperature coefficients calculated. Although the higher features in the  $Im\left(\frac{\Delta r}{r}\right)$  spectra are more difficult to attribute to the  $E_2$  transition, the temperature coefficient for the feature at 3.46 eV does show good agreement and is attributed to be the  $E_1$  transition.

In the final part of the chapter bulk dielectric data was used alongside the  $Re\left(\frac{\Delta r}{r}\right)$  and  $Im\left(\frac{\Delta r}{r}\right)$  parts the RA spectra to determine the surface dielectric functions. The features within the surface dielectric function have been assigned to transitions  $E_1$  and  $E_2$  and show good agreement to the energies of the transitions obtained in previous experiments. The temperature dependence of these transitions has also been determined.

This chapter has shown that both the  $Re\left(\frac{\Delta r}{r}\right)$  and  $Im\left(\frac{\Delta r}{r}\right)$  parts of the RA spectra can be measured successfully. This will provide more useful information about the optical properties of the surface which will enhance the understanding of optical processes.

## 4.8 References

- [1] Cohen, M. L and Chelikowsky, J. R., *Electronic Structure and Optical Properties of Semiconductors*. (Springer-Verlag, Berlin) 1988
- [2] Pollak, R. A., Ley, L., Kowalczyk, S., Shirley, D. A., Joannopoulos, J. D., Chadi, D. J. and Cohen, M. L., *Phys. Rev. Lett.* **29** (1972) 1103
- [3] Grobman, W. D. and Eastman, D. E., *Phys. Rev. Lett.* **29** (1972) 1508
- [4] Phillips, J. C. and Pandey, K. C., *Phys. Rev. Lett.* **30** (1973) 787
- [5] Chelikowsky, J. R. and Cohen, M. L., *Phys. Rev. Lett.* **32** (1974) 674
- [6] Chelikowsky, J. R. and Cohen, M. L., *Phys. Rev. B* **14** (1976) 556
- [7] Fox, M., *Optical Properties of Solids*. (Oxford University Press, Oxford) 2001
- [8] Kittel, C., *Introduction to Solid State Physics*, Eighth Edition. (John Wiley & Sons Inc, Hoboken) 2005
- [9] Ivanov, I., Mazur, A. and Pollmann, J., *Surf. Sci.* **92** (1980) 365
- [10] Vuye, G., Fisson, S., Nguyen Van, V., Wang, Y., Rivory, J. and Abelès, F., *Thin. Solid. Films.* **233** (1993) 166
- [11] Aspnes, D. E. and Studna, A. A., *Phys. Rev. B.* **27** (1983) 985
- [12] Cardona, M., *Modulation Spectroscopy*, Suppl. 11 of *Solid State Physics*. (Academic, New York) 1969
- [13] Aspnes, D. E., *Handbook on Semiconductors*, Volume 2. (North Holland, Amsterdam) 1980
- [14] Tsoi, S., Rodriguez, S., Ramdas, A. K., Ager III, J. W., Riemann, H, and Haller, E. E., *Phys. Rev. B.* **72** (2005) 153203
- [15] Aoki, T. and Adachi, S., *J. Appl. Phys.* **69** (1991) 1574

- [16] Kondo, K. and Moritani, A., *Phys. Rev. B.* **15** (1977) 812
- [17] Daunois, A. and Aspnes, D. E., *Phys. Rev. B.* **18** (1978) 1824
- [18] Lautenschlager, P., Allen, P. B. And Cardona, M., *Phys. Rev. B.* **33** (1986) 5501
- [19] Mandl, F., Quantum Mechanics. (John Wiley & Sons Inc, Hoboken) 2003
- [20] Hanke, W., Meskini, N. and Weiler, H., Electronic Structure, Dynamics and Quantum Structural Properties of Condensed Matter. (Plenum, New York) 1985
- [21] Antončík, E., *Czech. J. Phys.* **5** (1955) 449
- [22] Schlüter, M., Martinez, G. and Cohen, M. L., *Phys. Rev. B.* **12** (1975) 650
- [23] Allen, P. B., *Phys. Rev. B.* **18** (1978) 5217
- [24] Chakraborty, B. And Allen, P. B., *Phys. Rev. B.* **18** (1978) 5225
- [25] Allen, P. B. And Cardona, M., *Phys. Rev. B.* **27** (1983) 4760
- [26] Okada, Y. and Tokumaru, Y., *J. Appl. Phys.* **56** (1984) 314
- [27] Jellison, Jr. G. E. and Modine, F. A., *Phys. Rev. B.* **27** (1983) 7466
- [28] Lautenschlager, P., Garriga, M., Viña, L. and Cardona, M., *Phys. Rev. B.* **36** (1987) 4821
- [29] Šik, J., Hora, J. and Humlíček, J., *J. Appl. Phys.* **84** (1998) 6291
- [30] Varshni, Y. P., *Physica* **34** (1967) 149
- [31] Rossow, U., Mantese, L. and Aspnes, D. E., *Appl. Surf. Sci.* **123/124** (1998) 237

- [32] Silaghi, S. D., Friedrich, M. And Zahn, D. R. T., *J. Phys. IV France* **132** (2006) 69
- [33] Chen, C., An, I. and Collins, R. W., *Phys. Rev. Lett.* **90** (2003) 217402



## **Chapter 5**

### **The Ag(110) surface**

## 5.1 Introduction

Silver is a transition metal and has a high electrical and thermal conductivity. Silver also has an interband absorption edge of  $\sim 4.00$  eV, within the ultraviolet range, and as a consequence has a high reflectivity throughout the visible spectrum of light. Hence silver is widely used for making mirrors and is also used in catalysts. In many systems silver is used as a coating on other materials to reduce corrosion, or in optical techniques, to increase reflectivity. Therefore, understanding how a silver surface behaves is important to further this range of technology.

This research specifically uses a Ag(110) crystal which provides good anisotropy to yield RA spectra. In air at room temperature silver possesses an oxide layer which dissociates on heating leaving a clean, oxide free, surface. The thermodynamics of this process will be discussed in the next section.

This chapter will use a similar procedure to that discussed in chapter 4 beginning with the electronic structure of the Ag(110) surface. The chapter will then go on to present data for the  $Re\left(\frac{\Delta r}{r}\right)$  and  $Im\left(\frac{\Delta r}{r}\right)$  parts of the RA spectra before studying the azimuthal dependence of the RAS of the Ag(110) surface.

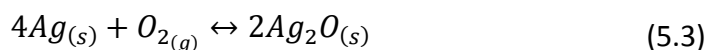
## 5.2 Ellingham Diagram for Silver

Ellingham diagrams were first introduced by Harold Ellingham in the 1940's and show the temperature dependence of the stability for elements and compounds. Initially Ellingham diagrams focused on the temperature dependence between a metal, its oxide and oxygen although this has been extended for reactions of a metal with other elements such as nitrogen. In this section the focus will be on oxidation reactions [1].

Ellingham diagrams plot the Gibbs free energy change,  $\Delta G$ , for oxidation reactions versus the temperature. The Gibbs free energy is given in equation 5.1.

$$\Delta G = \Delta H - T\Delta S \quad (5.1)$$

Where  $\Delta H$  is the change in enthalpy and  $\Delta S$  is the change in entropy at temperature  $T$ . Enthalpy measures the total energy of a system and when  $\Delta H < 0$  the reaction gives off energy whereas when  $\Delta H > 0$  the reaction requires an input of energy. The oxidation reaction for silver is given in equation 5.3, although a more general reaction is summarised in equation 5.2, for a single mole of  $O_2$ .



In general in the reactions described in equations 5.2 and 5.3, the metal and metal oxides are solids, (s), or liquids, (l), with the oxygen in gaseous phase (g). In a gaseous state the entropy,  $S$ , is much higher than in the solid state therefore the total entropy reduces during the reaction. Hence the majority of lines on Ellingham diagrams slope upwards with a gradient of  $\Delta S$  and intercept of  $\Delta H$ . This assumes no change of phase since  $\Delta H$  and  $\Delta S$  are constant with temperature unless there is a change of phase.

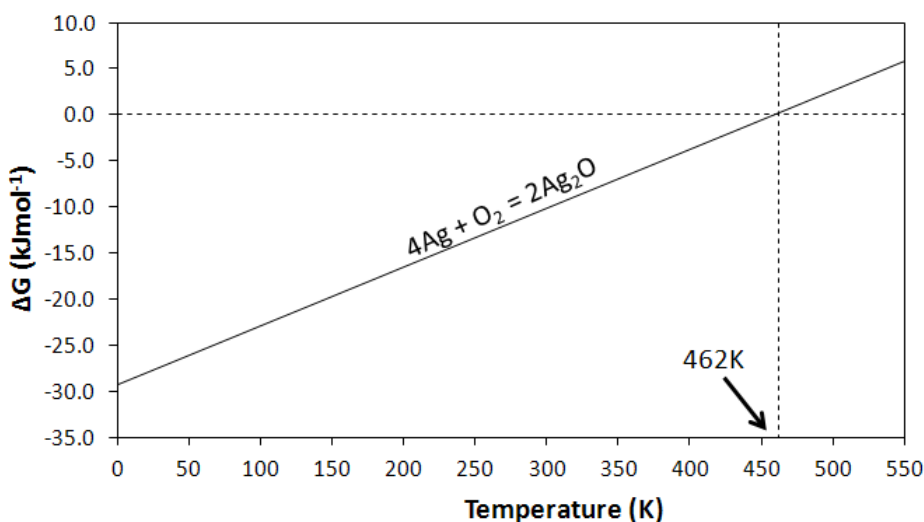


Figure 5.1: Diagram showing the reaction given in equation 5.3.

The reaction given in equation 5.3 is shown in figure 5.1. The diagram shows that at temperatures above 462 K,  $\Delta G > 0$  and therefore the oxygen dissociates from the

silver. However, this reaction assumes a pure oxygen environment when the partial pressure of oxygen,  $P_{O_2}$ , is equal to 1 and not atmospheric conditions. The partial pressure is related to the Gibbs free energy as it effectively acts as the reaction constant in an oxidation reaction as shown in equation 5.4.

$$\Delta G = RT \ln(P_{O_2}) \quad (5.4)$$

Where  $R$  is the gas constant and in atmosphere,  $P_{O_2} = 0.21$ . Figure 5.2 shows the reaction line in black along two lines which show the Gibbs free energy with respect to the partial pressures in pure oxygen and in atmosphere. By observing where these lines intersect the reaction line the temperature at which the oxide dissociates/recombines can be determined. In atmosphere this temperature is  $\sim 380$  K.

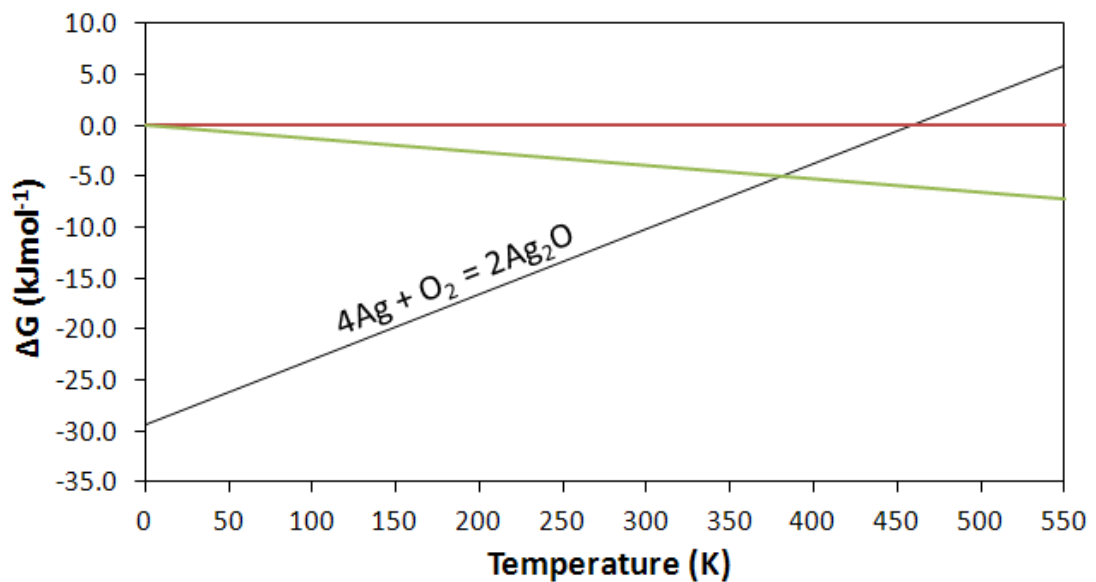


**Figure 5.2:** Basic Ellingham diagram showing the reaction line along with the line at  $P_{O_2} = 1$ , red line, and at  $P_{O_2} = 0.21$ , green line.

This temperature is achievable on the Linkham heating stage as described in section 4.5. Consequently the RA spectra can be produced at various temperatures observing how the Ag(110) surfaces transform.

## 5.3 The Ag(110) Surface

The chapter will now describe various properties of the Ag(110) surface and how RAS can be used to gain more information about the surface. This section will focus on the current understanding of the Ag(110) surface using RAS although other techniques have been used to get a thorough understanding.

### 5.3.1 The Electronic Structure of the Ag(110) Surface

The electronic band structure of a material can explain many physical properties such as optical absorption and electrical conductivity. Generally they are described with respect to high symmetry points in the Brillouin zone as discussed in chapter 2.

Experimental techniques [2,3] and theoretical calculations [4] have been the foundation for the current understanding of the electronic structure of the Ag(110) surface. Figure 5.3 shows the surface band structure which was obtained using momentum resolved inverse photoemission spectroscopy at  $\hbar\omega = 9.7 \text{ eV}$ . The states labelled  $S_1$  and  $S_2$  show the intrinsic surface states at the  $\bar{X}$  and  $\bar{Y}$  points of the surface Brillouin zone respectively.

This text box is where the unabridged thesis included the following third party copyrighted material:

Goldmann, A., Dose, V. and Borstel, G., *Phys. Rev. B.* **32** (1985) 1971

Figure 5.3: Electronic band structure for the Ag(110) surface [3].

### 5.3.2 Reflection Anisotropy Spectroscopy of the Ag(110) Surface in UHV

The features observed using RAS can provide vital information about the surface structure of Ag(110). The RA profile of the Ag(110) surface in UHV at room temperature is shown in figure 5.4 with three main features labelled a, b and c. The lowest energy feature, a, at 1.70 eV is attributed to a transition between surface states at the  $\bar{Y}$  point of the surface Brillouin zone [5]. The transition is between an occupied state 0.10 eV below the Fermi level and an unoccupied surface state 1.60 eV above the Fermi level. This feature is sensitive to contamination such as oxygen absorption [6]. These surface states exist in projected s,p-like band gaps of the bulk Brillouin zone. The occupied state has  $p_y$  type character and the unoccupied state has s type character. There is a similar transition between surface states at the  $\bar{Y}$  point on the Cu(110) surface which will be discussed in detail in chapter 6. However, the peak intensity for the transition on the Cu(110) surface is much higher than the peak intensity on the Ag(110) surface because there are more occupied states present on the Cu(110) surface. This has been confirmed with pseudopotential calculations of the band structure [2]. Another difference is that this transition between surface states at the  $\bar{Y}$  point on the Ag(110) is the sole contributor to the resulting peak intensity in the RA profile, whereas for the transition on the Cu(110) surface there are other contributions from bulk bands and interband transitions which will be discussed in full later.

This text box is where the unabridged thesis included the following third party copyrighted material:

Hansen, J. -K., Bremer, J. and Hunderi, O., *Surf. Sci.* **418** (1998) L58

**Figure 5.4: RA profile of Ag(110) at room temperature in UHV. Inset shows the transition between surface states at 1.7 eV [6].**

As seen in figure 5.4 the higher energy features in the RA spectrum are more dominant than the feature attributed to a transition between surface states at 1.7 eV. At ~3.8 eV there is a sharp positive peak followed immediately by a sharp negative feature at ~3.9 eV. These peaks do not appear to be sensitive to surface contamination [5] which suggests this feature is related to the bulk dielectric response. This is further confirmed since interband transitions for silver begin at an energy of ~3.8 eV [8]. In particular, transitions at ~3.9 eV and ~4.1 eV have been attributed to transitions around the L point of the Brillouin zone [17]. At lower energy there is a transition from  $E_F \rightarrow L_1$  and at higher energy from  $L_{2'} \rightarrow L_1$  as shown schematically in figure 5.5. There is a further transition shown in figure 5.5 from  $L_3 \rightarrow L_{2'}(E_F)$  [9] although this is not discussed in this research.

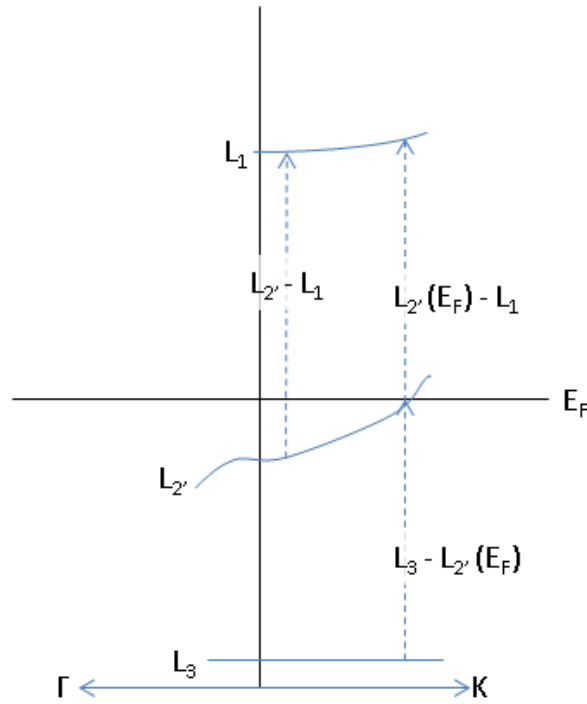


**Figure 5.5: Schematic diagram about the L point of the Brillouin zone showing three transitions.**

The dependence of these peaks on surface morphology has been studied by J. Bremer *et al* [10] who used RAS alongside STM images to show how the peaks change as the surface changes. When the two peaks are present, STM images show step edges aligned parallel to the  $[1\bar{1}0]$  crystallographic direction. In contrast, when the lower energy peak is no longer present in the spectrum the steps on the surface have an isotropic structure. This is confirmed theoretically although the theory predicts a much smaller magnitude than is observed by experiment. This discrepancy is explained by the absorption of light by surface plasmons induced by the steps which increase the peak intensity in the RA spectrum. These peaks coincide with the plasmon resonance energy at 3.90 eV [11]. Furthermore the surface plasmons present on the Ag(110) surface show strong dependence on the crystal azimuth [12] which agrees with the results of theoretical calculations [13,14,15]. Consequently, the RA spectrum of the Ag(110) surface in UHV at room temperature may, or may not, include the lower energy peak at 3.80 eV depending on whether the surface possesses terraces parallel to the  $[1\bar{1}0]$  direction or ordered terraces in no preferred direction.



### 5.3.3 The Temperature Dependence of the Ag(110) Surface

As discussed in chapter 4 understanding how surface properties change with temperature can provide information relevant to many practical applications.

The results of photoemission experiments [16] show that the energy of the occupied surface state reduces linearly as the temperature is increased from 60 K to 450 K at a rate of  $\sim 1.7 \text{ meVK}^{-1}$ . In addition, RAS experiments have shown that as the temperature of the Ag(110) surface increases the peak energy of the feature that has been attributed to the transition between surface states at 1.70 eV reduces [17]. This is consistent with a decrease in binding energy of the initial occupied surface state, as seen in the photoemission experiments, since when the binding energy of this state is reduced the energy required to induce transitions to the unoccupied state is also reduced. The energy of the unoccupied state is independent of temperature. Consequently, the RA peak attributed to the transition between surface states at the  $\bar{Y}$  point is shifted to lower energies. Martin *et al* [17] also observed the 1.70 eV peak reduce in intensity at temperatures up to  $\sim 520 \text{ K}$ . Above 520 K the feature is no longer present in the RA profile. The reduced peak intensity as temperature is increased is due to the initial occupied state being shifted up towards, and then over, the Fermi level causing a depopulation of the state. The depopulation of the occupied state reduces the number of possible transitions between the two surface states hence reducing the overall RA peak intensity.

The temperature dependence of the higher energy features at  $\sim 3.90 \text{ eV}$  also show a decrease in peak energy in the RA spectrum at higher temperatures. The peak energy positions have been observed to vary linearly with temperature and the gradients are shown in table 5.1 alongside gradients calculated using other techniques. In this case the RAS data has been produced using an Ag(110) surface prepared by annealing to 1000 K. By preparing the crystal in this way, the sharp

positive feature observed at  $\sim 3.8$  eV is not present as the terraces on the surface have no particular directional alignment.

<i>Peak Energy (eV)</i>	$\sim 3.9$ eV	$\sim 4.1$ eV
<b>Data Set</b>	<b>Temperature Dependence (<math>10^{-4}</math> eVK<math>^{-1}</math>)</b>	
<b>A</b>	$\sim 4.8$	$\sim 5.9$
<b>B</b>	$\sim 8.5$	$\sim 8.5$
<b>C</b>	$\sim 6.6$	$\sim 6.0$

**Table 5.1: Table showing the temperature gradients using various techniques. All values are quoted to an error of  $0.1 \times 10^{-4}$  eVK $^{-1}$ .**

In table 5.1, A are RAS experiments performed by Martin *et al* [17], B are experiments using a polarimetric method which measures  $\frac{\Delta \varepsilon''_b}{\Delta T}$  [18] and C used thermorefectance measurements [19]. Table 5.1 shows reasonable consistency between the three gradients despite the different techniques used.

#### **5.3.4 The Azimuthal Dependent Reflection Anisotropy Spectroscopy of the Ag(110) Surface**

As discussed in section 3.3, azimuthal dependent reflection anisotropy spectroscopy (ADRAS) can yield a more detailed understanding of the surface. In particular it can be used to determine the alignment of molecules [20] adsorbed on a surface or the alignment of dipole transitions on films deposited on a surface [21,22]. Generally, the ADRAS data for surfaces, including Au(110) and Cu(110) [23] follow a  $\cos 2\vartheta$  dependence. However, the Ag(110) surface exhibits a different dependence around the plasmon resonance energy at 3.90 eV.

Figure 5.6 shows the ADRAS data for Ag(110) around 3.90 eV. At energies higher and lower than the plasmon resonance frequency the surface shows a  $\cos 2\vartheta$  dependence and the results can be fitted to equation 3.51 in chapter three. However, at 3.90 eV the RA response is much smaller and shows a  $\sin 4\vartheta$

dependence. In this case the RAS data is fitted to equation 5.5 which includes the  $\sin 4\vartheta$  dependence.

$$Re\left(\frac{\Delta r}{r}\right) = A + B \cos(2\theta + \phi) - C \sin(4\theta + \phi) \quad (5.5)$$

This text box is where the unabridged thesis included the following third party copyrighted material:

Farrell, T., Harrison, P., Smith, C. I., Martin, D. S. and Weightman, P., *Appl. Phys. Lett.* **93** (2008) 191102

**Figure 5.6: ADRAS data for the Ag(110) surface around the plasmon energy at 3.9 eV [11].**

Farrell *et al* [11] have explained the  $\sin 4\vartheta$  dependence by using a frame of reference in which the sample components,  $r_x$  and  $r_y$  are aligned at  $45^\circ$  with respect to the polariser. A schematic diagram of the frame of reference used is shown in figure 5.7.

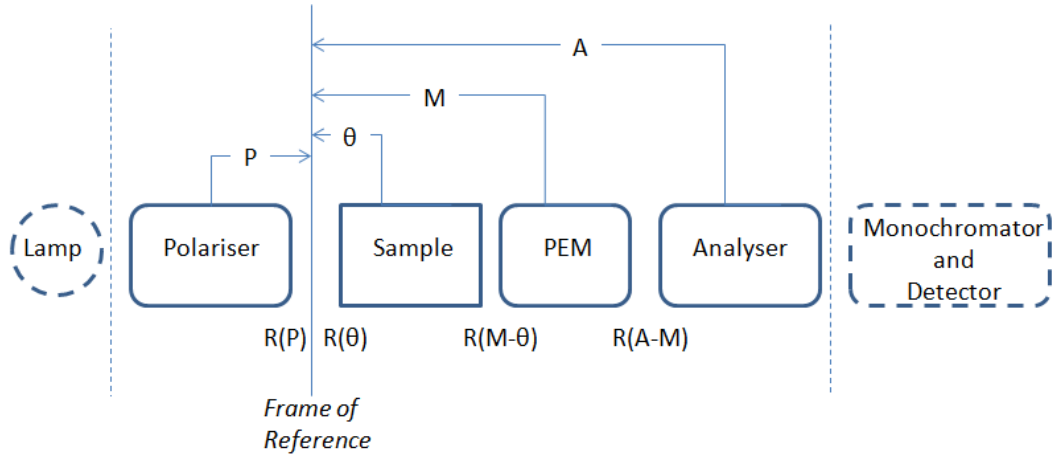


**Figure 5.7: Schematic diagram showing the frame of references and the rotation matrices for the rotating sample system.**

The Jones matrices used in this analysis differ from those described in section 3.2. In this case the polariser, analyser and modulator are set to  $45^\circ$ ,  $90^\circ$  and  $-45^\circ$  respectively with respect to the sample. The sample components,  $r_x$  and  $r_y$  can be represented by their real and imaginary components as shown in equation 3.25 but also repeated below:

$$r_x = a + ib \quad (5.6)$$

$$r_y = c + id \quad (5.7)$$

The rotation matrices shown in figure 5.7 are:

$$R(A - M) = R(P) = \frac{1}{\sqrt{2}} \begin{bmatrix} 1 & -1 \\ 1 & 1 \end{bmatrix} \quad (5.8)$$

$$R(\theta) = \begin{bmatrix} \cos(\theta) & \sin(\theta) \\ -\sin(\theta) & \cos(\theta) \end{bmatrix} \quad (5.9)$$

$$R(M - \theta) = \frac{1}{\sqrt{2}} \begin{bmatrix} (\cos(\theta) - \sin(\theta)) & (\cos(\theta) + \sin(\theta)) \\ -(\cos(\theta) + \sin(\theta)) & (\cos(\theta) - \sin(\theta)) \end{bmatrix} \quad (5.10)$$

which, by following a similar procedure as described from the matrix multiplication in section 3.2, gives the intensity of the optical response as:

$$I = \Gamma\{[K + L \sin(2\theta)] + M \cos(2\theta) \sin(\delta) + [L \cos(2\theta) - N \sin(4\theta)] \cos(\delta)\} \quad (5.11)$$

where  $\Gamma$  is an instrument constant and  $\delta = E \sin(\omega t)$  and is the retardation induced by the PEM. The constants  $K$ ,  $L$ ,  $M$  and  $N$  are:

$$K = 2\{(a^2 + b^2) + (c^2 + d^2)\} \quad (5.12)$$

$$L = 2\{(a^2 + b^2) - (c^2 + d^2)\} \quad (5.13)$$

$$M = 4(bc - ad) \quad (5.14)$$

$$N = (a - c)^2 + (b - d)^2 \quad (5.15)$$

Equation 5.11 is different to that described in chapter 3 (equation 3.29). However, as with equation 3.29, the first term,  $K + L \sin 2\vartheta$ , is the dc term and describes the total reflections as shown in equation 3.35. The remaining terms then describe the reflectance difference at the modulator frequency  $f$  (imaginary term) and  $2f$  (real term) shown in equations 3.36 and 3.37 respectively.

It follows that when  $\vartheta = 0^\circ$  the dc term is proportional to  $(R_x + R_y)$  since  $r_x^* r_x = R_x$  and  $r_y^* r_y = R_y$  as shown in equation 2.23 and where  $R_x$  or  $R_y$  are the reflections in the  $x$  or  $y$  direction. As the sample is rotated through the angle  $\vartheta$ , the  $\sin 2\vartheta$  term will no longer equal zero and will have a corresponding contribution proportional to  $(R_x - R_y)$ .

The imaginary term, involving  $\sin \delta$ , varies as  $\cos 2\vartheta$  and the real term, involving  $\cos \delta$ , varies as  $\sin 4\vartheta$ . The additional contribution involving  $\cos \delta$  is a  $\cos 2\vartheta$  term which again will have a magnitude proportional to  $(R_x - R_y)$ . For cubic materials  $(R_x + R_y) \gg (R_x - R_y)$  and therefore the latter term is usually negligible.

The  $\sin 4\vartheta$  term will only be zero when  $\vartheta = 0^\circ$  or when  $a = c$  and  $b = d$ . In contrast the  $\cos 2\vartheta$  term will be zero when  $R_x = R_y$  which is possible for numerous values of  $a$ ,  $b$ ,  $c$  and  $d$ . These terms depend on the complex refractive index,  $N$ , and are also related to the dielectric function,  $\epsilon$ , as shown in equation 2.20. Hence when the

dielectric function is anisotropic, the real term will be finite, not including the  $\vartheta = 0^\circ$  situation, regardless of whether the reflectance is isotropic.

In the bulk of cubic materials the dielectric function is isotropic,  $\epsilon_x = \epsilon_y$  and therefore  $a \sim c$  and  $b \sim d$ . If the constants,  $g$  and  $h$ , are the factors which relate  $c$  to  $a$  and  $d$  to  $b$  respectively the resulting equations are:

$$c = ga \quad (5.16)$$

$$d = hb \quad (5.17)$$

Then providing  $g \sim h$  and  $g \sim 1$ , then the ratio between  $L$  and  $N$  from equations 5.13 and 5.15 vary as:

$$\frac{2(1 - g^2)}{(1 - g)^2} \quad (5.18)$$

Hence,  $L \gg N$ , in general and so the  $\cos 2\vartheta$  term dominates the real part of the spectrum. Furthermore, in the dc term,  $K \gg L$  which is then observed to be independent of  $\vartheta$ . The  $\cos 2\vartheta$  is equal to zero when:

$$(a^2 + b^2) = (c^2 + d^2) = (g^2 a^2 + h^2 b^2) \quad (5.19)$$

which will give  $N$  a value of:

$$N = 2\{a^2(1 - g) + b^2(1 - h)\} \quad (5.20)$$

However, the earlier assumption was that  $g$  and  $h$  are close to unity and therefore the  $N$  term will be very small. This explains the presence of the  $\sin 4\vartheta$  dependence at a much smaller intensity seen in figure 5.6. Although this  $\sin 4\vartheta$  dependence is rare on metal surfaces there is no reason to suggest that it should not be present on more surfaces. A similar dependence has been observed in polymers [21] although this was thought to arise incoherence from the optical response of the surface.

## 5.4 The Reflection Anisotropy Spectroscopy of the Ag(110) Surface

The chapter will focus on the results obtained from RAS experiments on the Ag(110) surface in air. Initially the  $Re\left(\frac{\Delta r}{r}\right)$  part of the spectrum will be investigated before moving on to study the  $Im\left(\frac{\Delta r}{r}\right)$  part of the RA spectrum. The temperature dependence of the Ag(110) surface will be studied along with the azimuthal dependence of the RA spectrum at higher temperatures. As discussed in section 5.2 as the Ag(110) crystal is heated the oxide layer dissociates leaving an oxide free surface. The heating stage used in the research is the same as that described in chapter 4. However, the silver crystal used in this research has a larger thickness than the silicon wafer discussed previously. It is therefore important to allow more time between heating the sample and performing the experiments. As explained earlier this research focuses on how the Ag(110) surface changes with variation in temperature and therefore absolute temperature values on the surface is of less importance.

It is important to note that assurance that the oxide has been removed from the surface relies only on the Ellingham diagram studies and therefore to further this research it would be important to perform x-ray photoemission spectroscopy (XPS) measurements on the Ag(110) surface. This would provide definitive results which show the Ag(110) surface is oxide free.

### 5.4.1 The $Re\left(\frac{\Delta r}{r}\right)$ part of the RA Spectra

The RA spectrum of the Ag(110) surface at room temperature, 293 K, is shown in figure 5.8. This spectrum was obtained from a new Ag(110) crystal without any prior cleaning. The features observed in previous experiments at ~3.90 eV and 4.10 eV are present although at a much larger intensity than those observed under a UHV environment. The transition between surface states observed in UHV at

~1.70 eV is not present in the spectrum at room temperature in air. This transition is extremely sensitive to surface contamination and at room temperature in an atmospheric environment the Ag(110) surface will have an oxide layer and therefore the transition between surface states is not expected to be observed. The lower energy feature at ~3.90 eV has a higher absolute intensity than the feature at ~4.10 eV which is the opposite to that observed in a UHV environment as shown in figure 5.4.

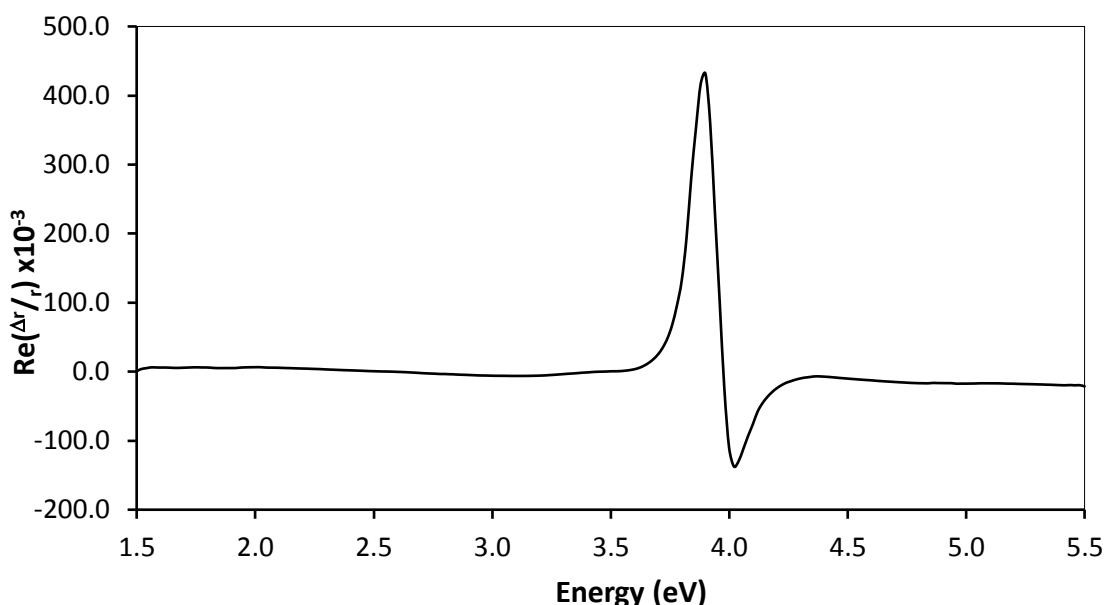


**Figure 5.8: RA spectrum of the Ag(110) surface at room temperature.**

As discussed in section 5.2 the thermodynamic properties of the Ag(110) surface show that as the temperature of the surface increases the oxide layer will dissociate from the surface leaving a clean Ag(110) surface. This will happen at temperatures above ~380 K. However, the crystal is heated to 623 K to compensate for any error in the heating stage and to ensure the Ag(110) surface is oxygen free. The RA spectrum of the Ag(110) surface at 623 K is shown in figure 5.9. The two main differences between figures 5.8 and 5.9, which have significantly different vertical scales, are the reduced intensity of the features at ~3.90 eV and at ~4.10 eV together with a movement to lower energies. The reduction in intensity of the RA signal is consistent with the native oxide layer being removed from the surface. The



reduction in peak energy is also consistent with previous observations. The dependence of peak energy on temperature will be discussed later. At 623 K the transition between surface states at 1.70 eV is not present, as expected, as the occupied surface state is expected to have been raised above the Fermi level.

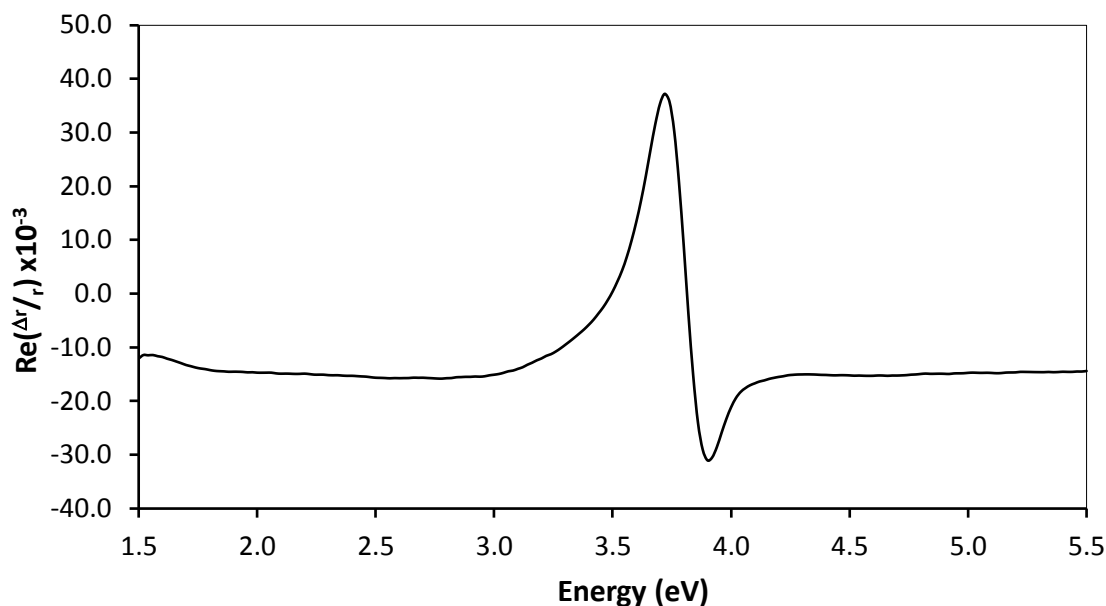
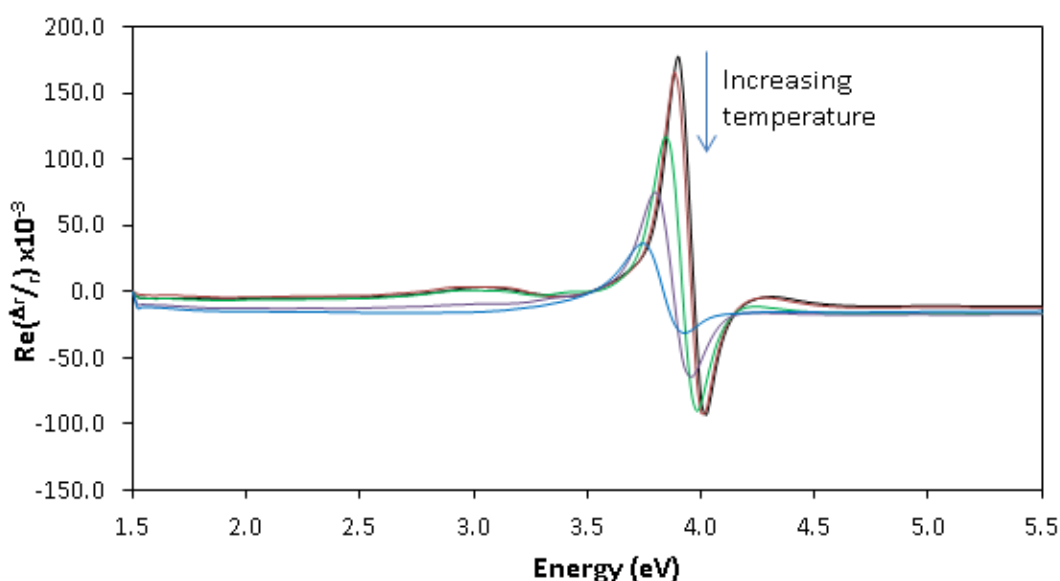


Figure 5.9: RA spectrum for the Ag(110) surface at 623 K in air.

#### 5.4.2 The $Re\left(\frac{\Delta r}{r}\right)$ part of the RA Spectra as a function of temperature

The RA spectra of the Ag(110) surface at various temperatures up to 623 K are shown in figure 5.10. None of these spectra show the transition between surface states at 1.70 eV. This could be due to the surface sensitivity of the transition since the surface states involved may not exist out of a UHV environment. Although there have been observations of transitions between surface states in UHV [5,6,17] and electrochemical environments [25,26] there is no evidence to suggest they exist in other ambient environments.

Between 323 K and 423 K the oxide layer dissociates from the Ag(110) surface. At these temperatures the lower energy feature in the RA spectra moves from 3.86 eV to 3.82 eV and then continues to move to lower energies as the temperature increases further. The energy dependence of the peak with temperature is linear and has a gradient of  $4.67 \times 10^{-4} \text{ eV K}^{-1}$ . This is comparable with the value for the gradient of the peak energy at  $\sim 3.90 \text{ eV}$  with temperature, given in table 5.1. The higher energy feature in the RA spectra also moves to lower energies as the temperature is increased although at a slower rate. In this case, although the energy dependence of the peak with temperature is linear, it has a gradient of  $2.67 \times 10^{-4} \text{ eV K}^{-1}$ , almost half that of the lower energy feature.



**Figure 5.10:** RA spectra for Ag(110) at 293 K (black line), 323 K (red line), 423 K (green line), 523 K (purple line) and 623 K (blue line).

Although the study of Ellingham diagrams can provide information on the thermodynamics of the surface these diagrams do not explain the reaction kinetics. The reaction kinetics describe the rate of the reaction given in equation 5.3 which takes place on the surface. Therefore, heating the surface at different rates may result in different RA spectra. Figure 5.11 shows the RA spectra when the surface was heated at  $1.0 \text{ K min}^{-1}$  from an initial time when the surface was at room

temperature, 293 K, up to 623 K a temperature which is reached after  $\sim 5$  hours. The RA spectra shown in figure 5.11 were obtained from the initial time, at 0 hours (black line), up to 4 hours (blue line) in hourly intervals. The inset shows the RA profile for 5 hours, 6 hours and 7 hours after the initial heating around the peak energy at  $\sim 3.80$  eV at which point the temperature will be constant at 623 K. As seen in figure 5.11 the peak at  $\sim 3.80$  eV reduces in intensity and moves to lower energy as the temperature is increased from 293 K to 623 K which is similar that observed in figure 5.10. After  $\sim 5$  hours, 623 K will be reached and the peak at  $\sim 3.80$  eV no longer shows an energy shift. This is seen in the inset to figure 5.11 although there is still a small drop in intensity. The higher energy feature at  $\sim 4.00$  eV also moves to lower energy and reduces in intensity before becoming constant at  $\sim 6$  hours.

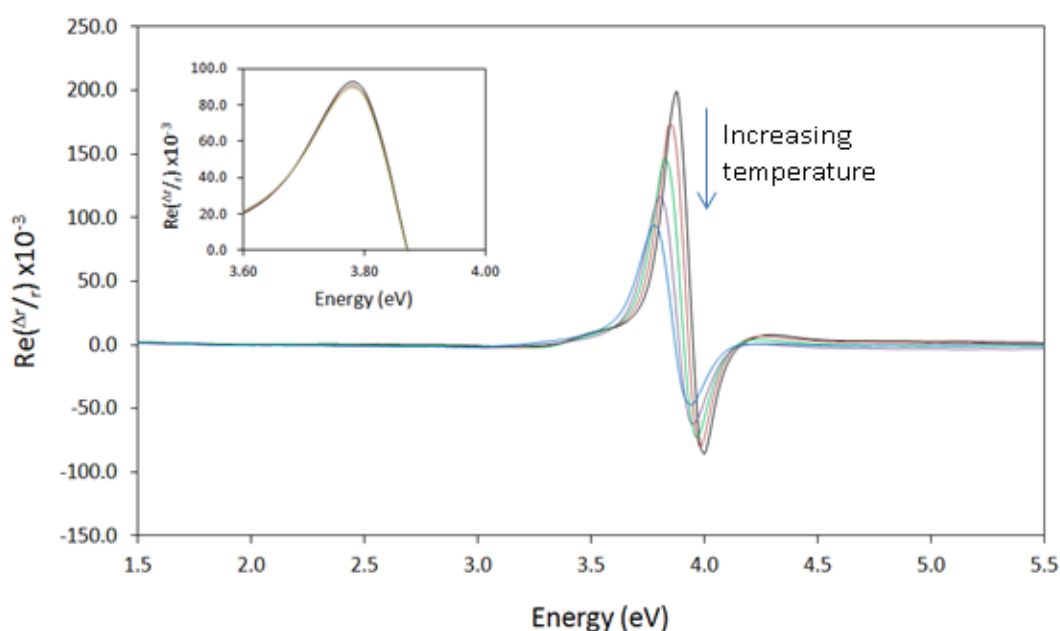


**Figure 5.11: RA spectra heated from 293 K to 623 K at a rate of  $1.0 \text{ Kmin}^{-1}$ . Spectra taken at 0 hours (black line), 1 hour (red line), 2 hours (green line), 3 hours (purple line) and 4 hours (blue line). Inset shows the peak at  $\sim 3.8$  eV at times 5 hours, 6 hours and 7 hours.**

The RA spectra when the rate at which the temperature on the surface is reduced to  $0.1 \text{ Kmin}^{-1}$  is shown in figure 5.12. Increasing the temperature at this rate will

mean that the Ag(110) surface will have reached 623 K after  $\sim 60$  hours. Overall, the features observed in the RA spectra in figure 5.12 show the same dependencies as the previous spectra in figures 5.10 and 5.11 as the temperature is increased from 293 K to 623 K. Hence as the temperature is increased from 293 K from an initial time, 0 hours (black line) to a final temperature of 623 K after 60 hours (blue line) the features at  $\sim 3.80$  eV and  $\sim 4.00$  eV have both shifted to lower energies. There is a further feature observed in figure 5.12 at  $\sim 4.20$  eV which is only present at times up to 15 hours after the initial heating began. After  $\sim 15$  hours, the temperature would be  $\sim 370$  K which is close to the temperature at which it is expected the oxide will dissociate from the Ag(110) surface. Therefore this feature at  $\sim 4.20$  eV is attributed to the oxide on the surface. The inset to figure 5.12 shows the RA spectra centred around the feature at  $\sim 3.80$  eV after 60 hours when the surface has reached 623 K. From the inset it can be seen that there is no longer an energy shift which is a result of the temperature staying constant at 623 K.

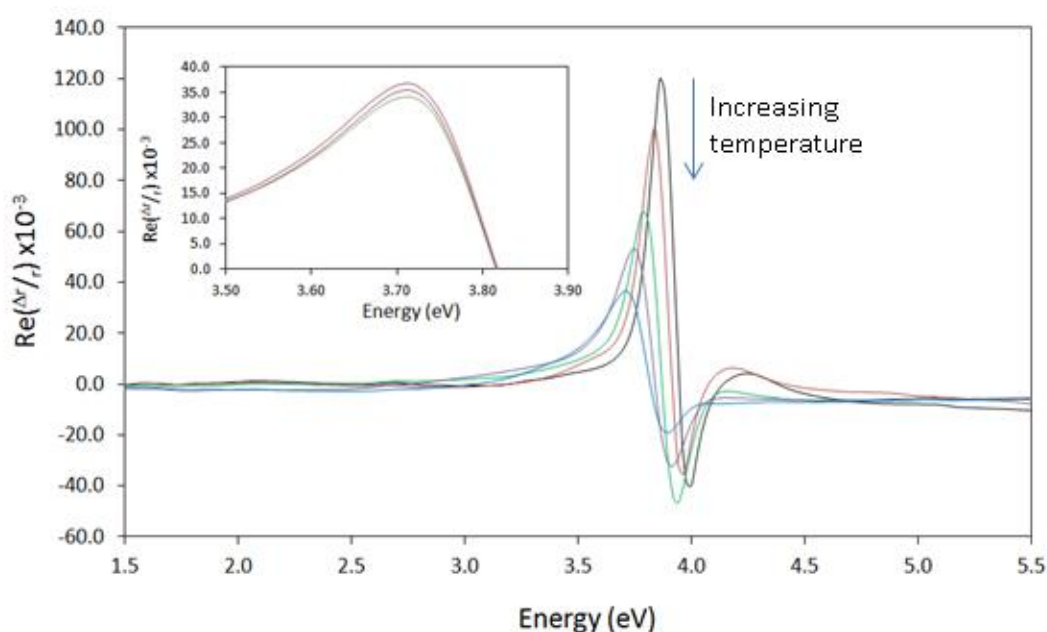


**Figure 5.12:** RA spectra heated from 293 K to 623 K at a rate of  $0.1 \text{ Kmin}^{-1}$ . Spectra taken at 0 hours (black line), 15 hour (red line), 30 hours (green line), 45 hours (purple line) and 60 hours (blue line). Inset shows the peak at  $\sim 3.8$  eV at times 60 hours, 70 hours and 80 hours.

The dependence of the peak energy at  $\sim 3.90$  eV on temperature is shown in figure 5.13 together with the values for the gradients of the temperature dependence of this RAS peak shown in table 5.2. The lines are fitted using the same methods as discussed in section 4.4.1 where the energy positions of the RAS peaks vary linearly as the temperature is increased. The values in table 5.2 show the gradients for the temperature dependence of the peak at  $\sim 3.90$  eV at the heating rates  $1.0 \text{ Kmin}^{-1}$  and  $0.1 \text{ Kmin}^{-1}$ , B and C respectively, alongside those found from Martin *et al* [17] in a UHV environment. Data set A in table 5.2 shows the value for the temperature dependence of the RAS peak at  $\sim 3.90$  eV observed when the temperature had been increased to specific temperatures. The values of the temperature coefficient of the RAS peak at  $\sim 3.90$  eV for the two heating rates, data sets B and C in table 5.2, only show a small discrepancy. Therefore, the rate at which the Ag(110) surface is heated has a negligible influence on the dependence of the 3.90 eV peak on temperature.

Data	Temperature Coefficient ( $10^{-4} \text{ eVK}^{-1}$ )
Martin <i>et al</i>	$\sim 4.8$
A	$\sim 4.67$
B	$\sim 4.65$
C	$\sim 4.93$

**Table 5.2:** Table showing the temperature coefficients at  $\sim 3.9$  eV for data from Martin *et al* [17], from heating to specific temperatures, A, from heating quickly over time, B and heating slowly over time, C. The uncertainties associated with the temperature coefficients are  $0.1 \times 10^{-4} \text{ eVK}^{-1}$  for Martin *et al* and  $0.05 \times 10^{-4} \text{ eVK}^{-1}$  for the data sets A, B and C as calculated using the standard deviation on multiple measurements.

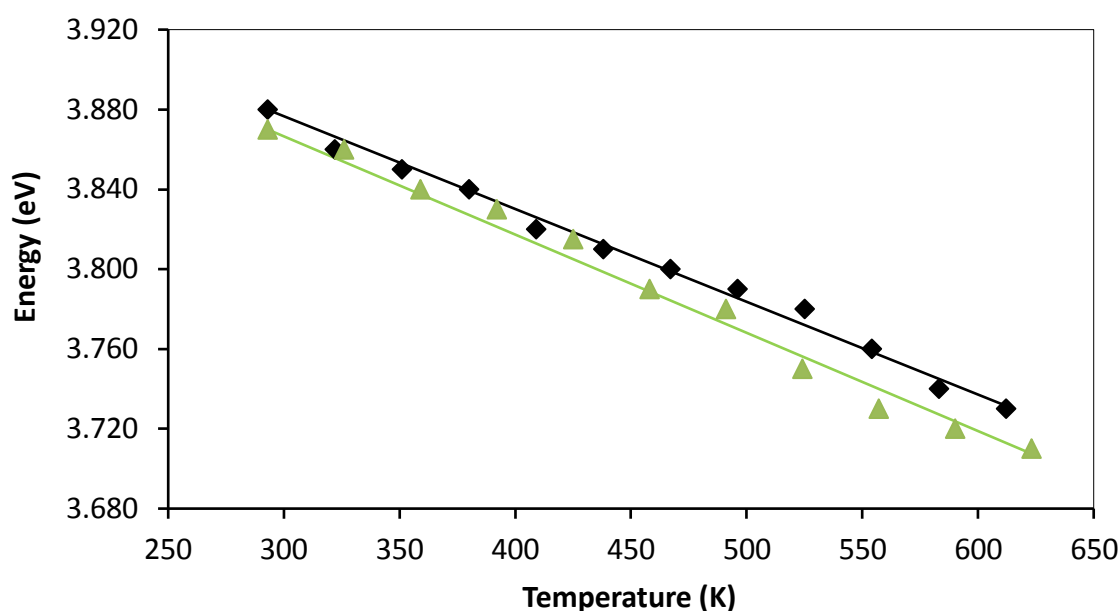


Figure 5.13: RA peak energy at ~3.90 eV as a function of temperature when the Ag(110) surface is heated at a rate of 1.0 Kmin-1 (black points) and at 0.1 Kmin-1 (green points) along with their respective fitted lines.

#### 5.4.3 The $Im\left(\frac{\Delta r}{r}\right)$ part of the RA spectra

The imaginary part of the RA spectrum at 293 K is shown in figure 5.14. There is a prominent negative feature in the RA spectrum around the plasmon energy of 3.90 eV with two smaller positive features on either side. Although the features in the imaginary part of the spectrum are around the same energy as in the real part of the spectrum they have different profiles. To understand the contribution to the spectrum from the clean Ag(110) surface, the surface is then heated up to 623 K when the oxide is dissociated from the surface.

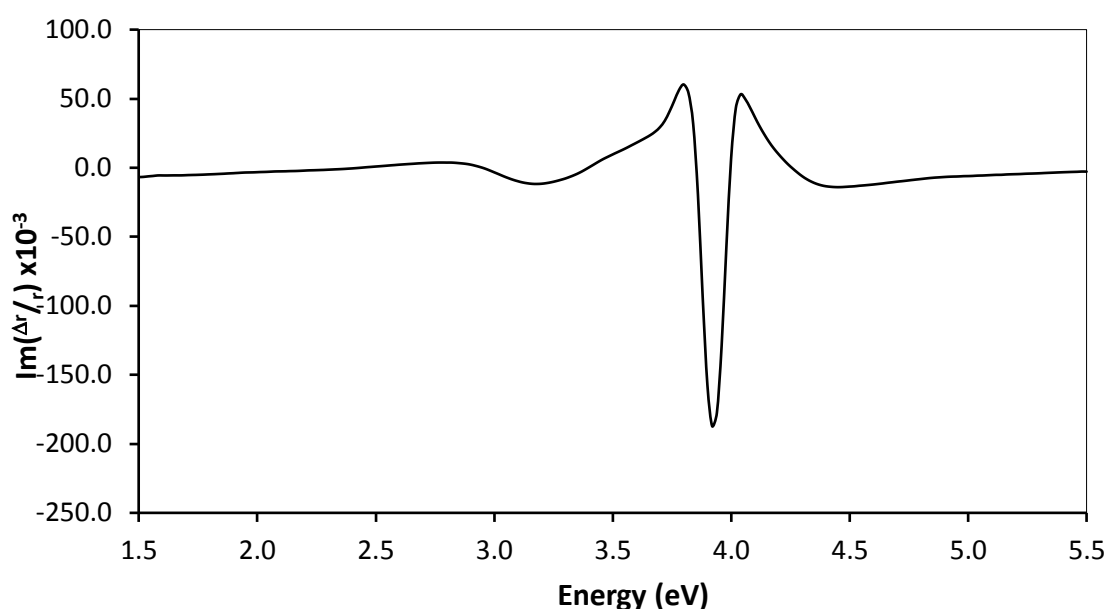


Figure 5.14: RA spectrum of the  $Im\left(\frac{\Delta r}{r}\right)$  for the Ag(110) surface at 293 K.

The RA spectrum for the Ag(110) surface after it has been heated to 623 K is shown in figure 5.15. The spectrum is different to that shown in figure 5.14 as the large negative feature has moved to lower energy and also decreased in intensity. This is the same dependence on temperature as that observed in the real part of the spectra although in this case the positive feature at higher energy,  $\sim 4.10$  eV in the 293 K spectra, is no longer present at 623 K. This suggests this feature was dependent on the oxide layer which is no longer present at these higher temperatures. The lower energy feature has also become broader at higher temperatures.

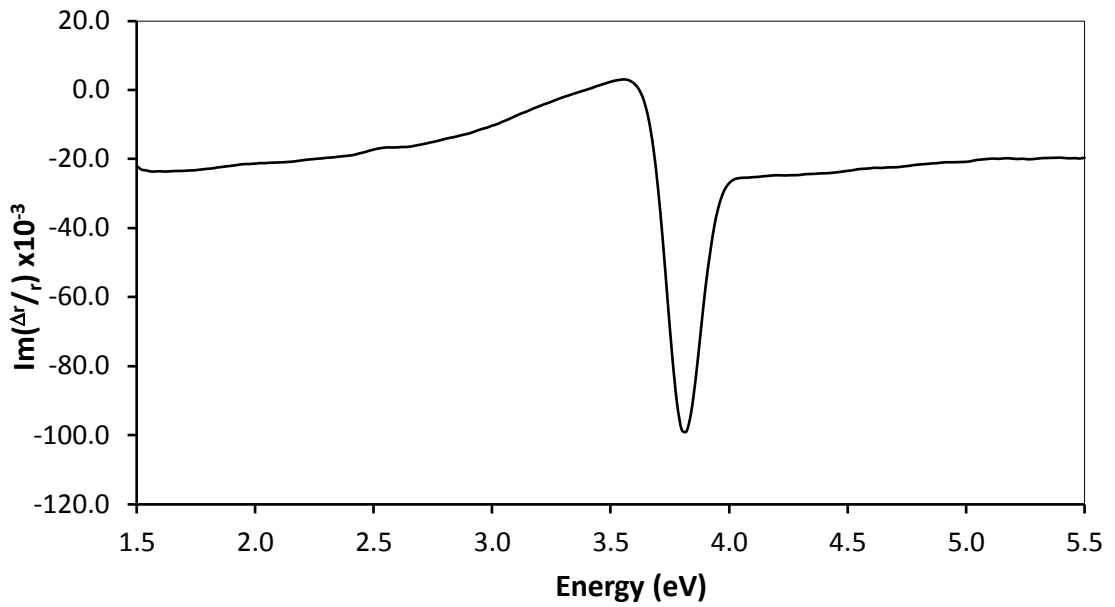


Figure 5.15: RA spectrum of the  $Im\left(\frac{\Delta r}{r}\right)$  for the Ag(110) surface at 623 K.

The dependence on the peak energy at  $\sim 3.90$  eV on temperature can be determined in the same way as for the  $Re\left(\frac{\Delta r}{r}\right)$  part of the RA spectra described in the previous section. Figure 5.16 shows the plot of peak energy against temperature along with lines fitted using a method similar to that in section 4.4.1 in which the peak energy varies linearly with temperature. There are two distinct temperature ranges apparent in figure 5.16. The first, shown in black, is from room temperature to 380 K where the oxide would still be present on the surface, and the second, shown in green, above 380 K where the oxide is expected to have dissociated. These ranges, below and above  $\sim 380$  K, were not observed when studying the  $Re\left(\frac{\Delta r}{r}\right)$  part of the RA spectra as the dependence of peak energy on temperature showed a continuous decrease in peak energy as the temperature is increased, as shown in figure 5.13. This implies that by studying the  $Im\left(\frac{\Delta r}{r}\right)$  part of the spectra over the same energy range, more information about the surface can be gained.



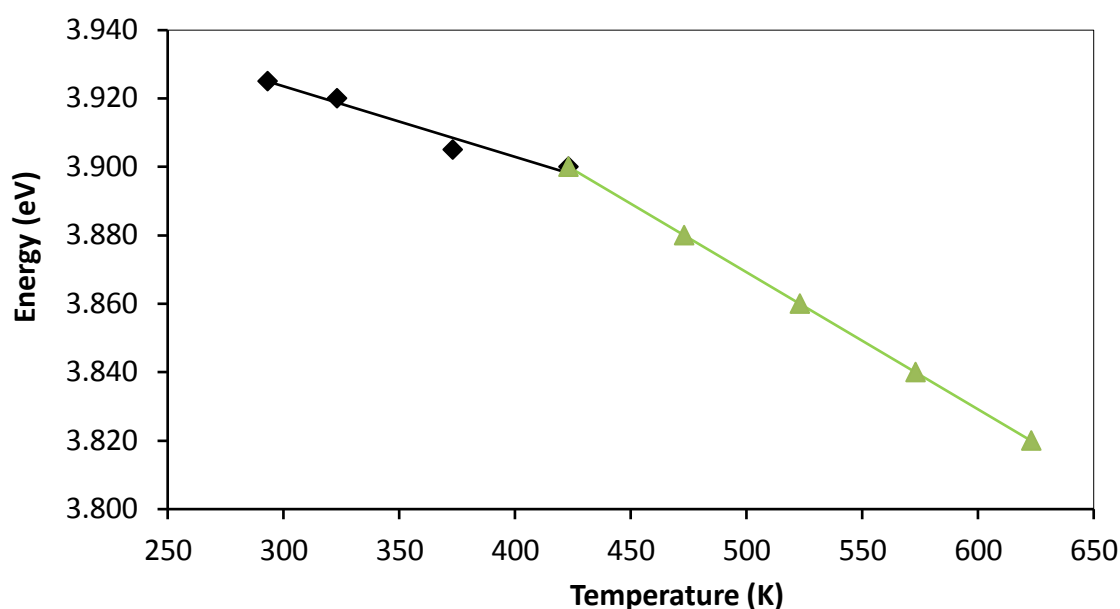


Figure 5.16: RA peak energy at 3.90 eV as a function of temperature when the Ag(110) surface is heated from 293 K to 623 K before (black points) and after (green points) the temperature at which oxide dissociates from the surface. The lines are calculated using the method described in 4.4.1.

The gradients of the dependence of the peak energy at ~3.90 eV on temperature can then be determined for the two ranges and are shown in table 5.3. Below the oxide dissociation temperature, the temperature coefficient is almost half that of the results shown in table 5.2. Whereas in the higher temperature range the coefficient, shown in table 5.3 is in reasonable agreement with the coefficient shown in table 5.2.

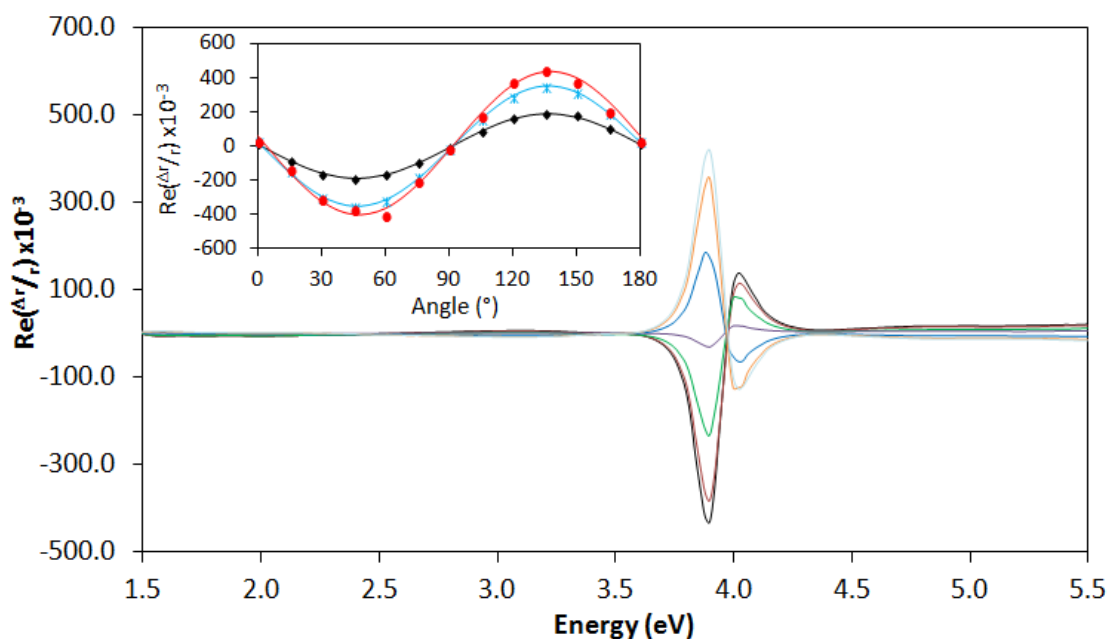
Data	Temperature Coefficient ( $10^{-4} \text{ eVK}^{-1}$ )
293 K < T < 423 K	2.07
423 K < T < 623 K	4.00

Table 5.3: Temperature coefficients for the  $Im\left(\frac{\Delta r}{r}\right)$  part of the RA spectrum. The uncertainties on the measurements are  $0.05 \times 10^{-4} \text{ eVK}^{-1}$  as calculated using the standard deviation on multiple measurements.

## 5.5 Azimuthal Dependence of the Ag(110) surface

As discussed previously the azimuthal dependence of the RAS of a surface can provide valuable insight into the electronic transitions that give rise to the RA spectrum. The Ag(110) surface is particularly interesting as at a specific energy of 3.90 eV the surface shows a  $\sin 4\vartheta$  dependence on the azimuthal angle which is in contrast to the more dominant  $\cos 2\vartheta$  variation. This variation around the plasmon energy at 3.90 eV has been identified in UHV conditions and one aim of this research is to explore whether this dependence can be observed in an atmospheric environment.

The angular variation of the RA spectrum for the Ag(110) surface at 293 K is shown in figure 5.17 along with the inset showing the dependence of the RAS intensity on angle at energies 3.82 eV, 3.86 eV and 3.90 eV. The spectrum shows the Ag(110) surface possesses, in general, a  $\cos 2\vartheta$  dependence although the spectrum does not fully collapse towards zero at  $\sim 3.90$  eV. This discrepancy could be due to a small error in the initial alignment. The surface is initially aligned so the RA spectrum is at a maximum, at  $0^\circ$ , and then rotated  $90^\circ$  to give the maxima spectra at  $0^\circ$  and  $90^\circ$ . Hence any error in the orientation of the  $0^\circ$  spectrum will result in the minimum spectrum at  $45^\circ$  containing small variations from the zero line. Alternatively the adsorbed oxygen present on the surface may give rise to transitions which do not have the same optical axes as the transitions attributed to the Ag(110) surface. The inset shows the RA intensity as a function of angle at three energies of 3.82 eV, 3.86 eV and 3.90 eV. At all three energies there is a  $\cos 2\vartheta$  dependence and there is no evidence for a  $\sin 4\vartheta$  dependence at 3.90 eV. The curves in the inset are determined using equation 3.51, as described in section 3.3.



**Figure 5.17:** RA spectra of Ag(110) at room temperature at 0 ° (black line), 15 ° (red line), 30 ° (green line), 45 ° (purple line), 60 ° (blue line), 75 ° degrees (orange line), 90 ° degrees (light blue line). The inset shows the variation in intensity of the RA signal at 3.82 eV (black line), 3.86 eV (blue line) and 3.90 eV (red line) along with the  $\cos 2\theta$  variation.

Following the results shown in figure 5.17 the surface was heated to 523 K at which temperature the oxide will have dissociated from the surface. A similar azimuthal rotation to that carried out at the lower temperature was performed. The RA spectra obtained in this rotation are shown in figure 5.18. As observed in the previous section, the magnitude of the features decreased when the temperature is increased and the peaks have also moved to slightly lower energy. However, the spectrum does show good symmetry about the 45 ° line when the RA signal is at a minimum, with the two maxima at 0 ° and 90 °. While the spectrum obtained at 45 ° does show a variation from the zero line at ~3.80 eV this has reduced in intensity from that shown in figure 5.17. The main peak in figure 5.18 occurs at 3.86 eV so the angular variation of the RA peak intensity is plotted at energies of 3.82 eV, 3.84 eV, 3.86 eV, 3.88 eV, 3.90 eV and 3.92 eV as shown in figure 5.19. Figure 5.19 shows that at all energies, except 3.86 eV, there is a clear  $\cos 2\theta$  dependence. The fitted lines shown in figure 5.19 are those determined using

equation 3.51 in chapter three. However, at 3.86 eV there is no clear  $\cos 2\vartheta$  or  $\sin 4\vartheta$  dependence as observed in the UHV experiments [11] although there is a phase change in the spectral profile of  $180^\circ$  at energies higher than 3.86 eV which as expected from the UHV work. The RA response close to the plasmon resonance energy at 3.90 eV in UHV conditions is highly surface sensitive. This could explain why the exact  $\sin 4\vartheta$  dependence is not observed in these experiments.

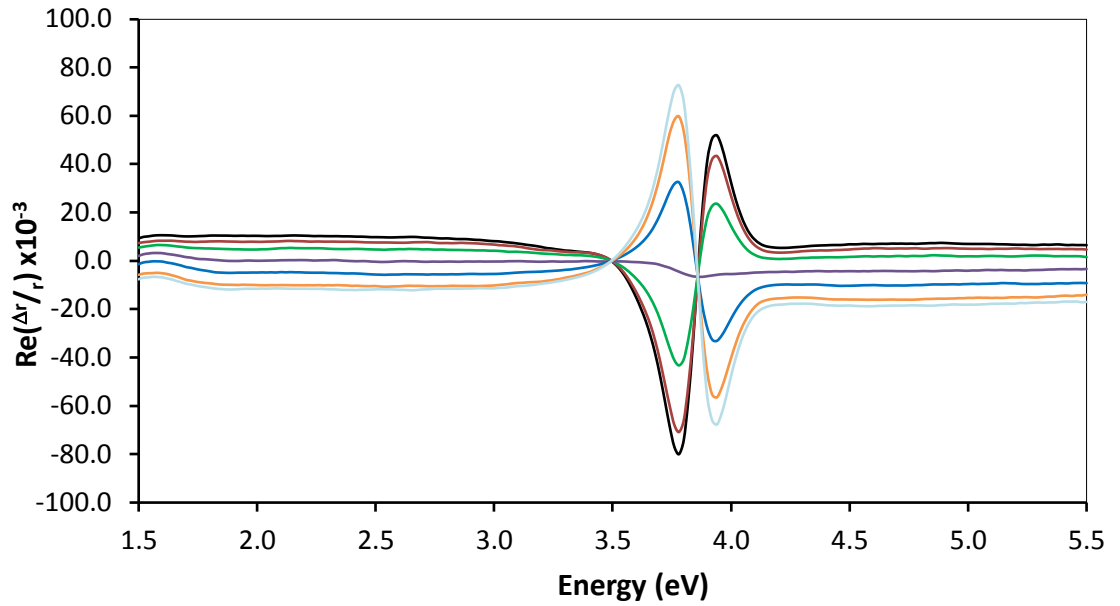


Figure 5.18: RA spectra of Ag(110) at 523 K at  $0^\circ$  (black line),  $15^\circ$  (red line),  $30^\circ$  (green line),  $45^\circ$  (purple line),  $60^\circ$  (blue line),  $75^\circ$  degrees (orange line),  $90^\circ$  degrees (light blue line).

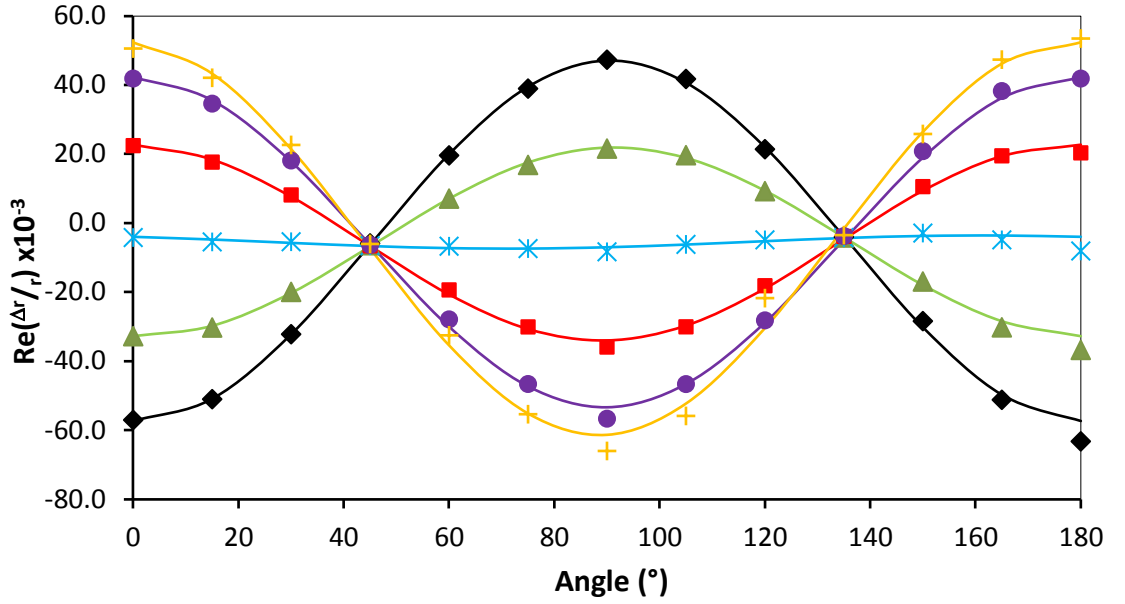


Figure 5.19: RA peak energy as a function of angle for energies of 3.82 eV (black diamonds), 3.84 eV (green triangles), 3.86 eV (blue crosses), 3.88 eV (red squares), 3.90 eV (purple circles) and 3.92 eV (orange plus signs). The fitted lines are calculated using the method described in section 3.3.

As discussed in section 5.3, the RAS optical response from the Ag(110) surface contains both a  $\cos 2\vartheta$  and a  $\sin 4\vartheta$  dependence although usually the  $\cos 2\vartheta$  dependence is much more dominant. Therefore, plotting the coefficient of  $\cos 2\vartheta$ ,  $B$  from equation 5.5, against the photon energy will show that  $B \sim 0$  when the  $\cos 2\vartheta$  term vanishes from the equation and the  $\sin 4\vartheta$  term is dominant. Figure 5.20, shows the data from Farrell *et al* [11] in UHV conditions along with the results obtained in this work in ambient conditions when the surface is heated to 523 K.

The two sets of data are significantly different in figure 5.20, although it is encouraging that the energy at which  $B \sim 0$  occurs is similar in both ambient (black line) and UHV conditions (red line) at 3.86 eV and 3.90 eV respectively. Furthermore, the shift observed from 3.90 eV in UHV to 3.86 eV in ambient could be due to a calibration error which can occur when using two different sets of equipment, a number of years apart. Alternatively this could be a result of the change in environment of the Ag(110) crystal. The peak observed from the UHV

experiments is broader than in ambient conditions. This could be because the Ag(110) surface is in a more stable environment in UHV since in air the surface will be more sensitive to fluctuations in the surrounding environment. Therefore the small energy region in which the  $\sin 4\theta$  can be observed in UHV has narrowed significantly when the surface is observed in an ambient atmosphere. However, although the  $\sin 4\theta$  curve is not observed in atmosphere, the other properties, such as the phase change of  $180^\circ$  and the magnitude of the  $B$  coefficient, at  $\sim 3.90$  eV are consistent with results obtained from UHV.

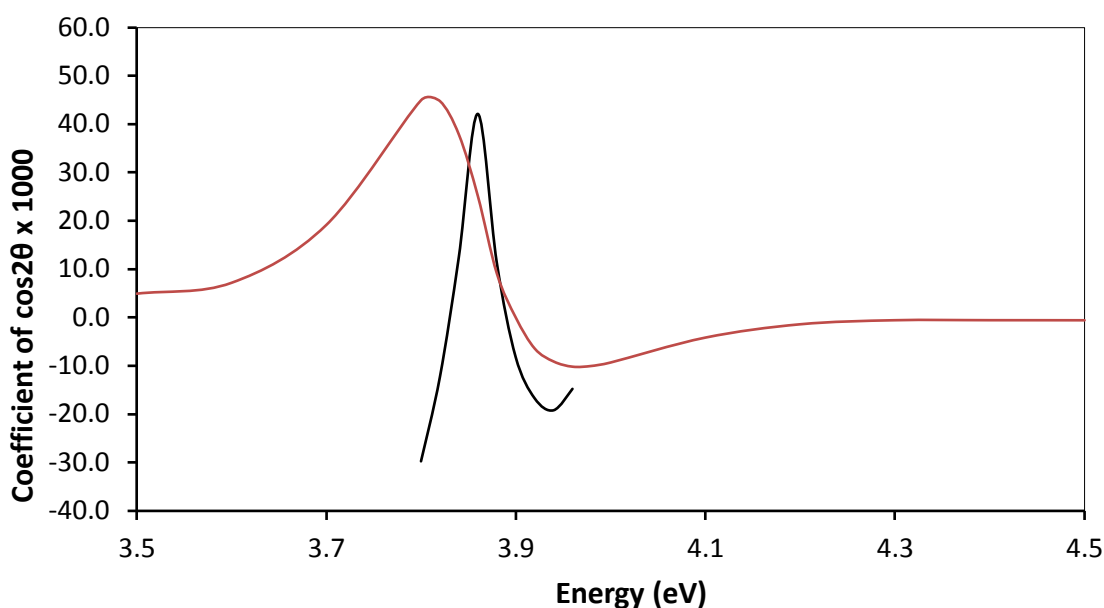


Figure 5.20: The  $\cos 2\theta$  coefficient,  $B$  from equation 3.51, from ambient conditions at 523 K compared to previous data in UHV [10].

## 5.6 Summary

This chapter has described the RAS studies of an Ag(110) surface in ambient conditions as it has been heated to temperatures up to 623 K. The chapter began by discussing Ellingham diagrams which help determine the temperatures at which the oxide layer will dissociate from the Ag(110) surface.

The chapter then went on to explain the current knowledge of the Ag(110) surface, in particular the  $\sin 4\vartheta$  dependence which is observed around the plasmon resonance frequency at  $\sim 3.90$  eV.

The chapter progresses to present the data for both the  $Re\left(\frac{\Delta r}{r}\right)$  and  $Im\left(\frac{\Delta r}{r}\right)$  parts of the RA spectra, and how they change from room temperature, 293 K, up to temperatures of 623 K. It has been observed that the  $Im\left(\frac{\Delta r}{r}\right)$  part of the RA spectra shows two distinct regions, at temperatures lower than when the oxygen dissociates from the surface, and temperatures higher than when the oxygen dissociates from the surface. This was not observed in the  $Re\left(\frac{\Delta r}{r}\right)$  part of the RA spectra. However, the gradients describing the dependence on peak energy with temperature for the  $Re\left(\frac{\Delta r}{r}\right)$  part of the RA spectra show good agreement with previous studies in UHV conditions.

Finally the chapter discussed the azimuthal dependence of the Ag(110) surface and although the  $\sin 4\vartheta$  dependence was not observed, there is evidence that the surface does behave differently around the plasmon resonance frequency at  $\sim 3.90$  eV which agrees with previous work from UHV.

## 5.7 References

- [1] Shatynski, S. R., *Oxid. Met.* **11** (1977) 307
- [2] Ho, K.- M., Harmon, B. N. and Liu, S. H., *Phys. Rev. Lett.* **44** (1980) 1531
- [3] Goldmann, A., Dose, V. and Borstel, G., *Phys. Rev. B.* **32** (1985) 1971
- [4] Jiang, M. Y., Pajer, G. and Burstein, E., *Surf. Sci.* **242** (1991) 306
- [5] Stahrenberg, K., Herrmann, T., Esser, N., Sahm, J., Richter, W., Hoffmann, S. V. and Hofmann, Ph., *Phys. Rev. B.* **58** (1998) R10207
- [6] Hansen, J. –K., Bremer, J. and Hunderi, O., *Surf. Sci.* **418** (1998) L58
- [7] Weightman, P., Martin, D. S., Cole, R. J. and Farrell, T., *Rep. Prog. Phys.* **68** (2005) 1251
- [8] Furtak, T. E. and Lynch, D. W., *Phys. Rev. Lett.* **35** (1975) 960
- [9] Liljenvall, H. G. and Mathewson, A. G., *J. Phys. C: Metal Phys. Suppl.* **3** (1970) S341
- [10] Bremer, J., Hansen, J. –K., Stahrenberg, K. and Worren, T., *Surf. Sci.* **459** (2000) 39
- [11] Farrell, T., Harrison, P., Smith, C. I., Martin, D. S. and Weightman, P., *Appl. Phys. Lett.* **93** (2008) 191102
- [12] Rocca, M., Lazzarino, M. and Valbusa, U., *Phys. Rev. Lett.* **69** (1992) 2122
- [13] Yibing, L., Levi, A. C. and Rocca, M., *Surf. Sci.* **336** (1995) 371
- [14] Liebsch, A., *Phys. Rev. Lett.* **71** (1993) 145
- [15] Feibelman, P. J., *Phys. Rev. Lett.* **72** (1994) 788



- [16] Gerlach, A., Meister, G., Matzdorf, R. and Goldmann, A., *Surf. Sci.* **443** (1999) 221
- [17] Martin, D. S., Blanchard, N. P., Weightman, P., Roseburgh, D. S., Cole, R. J., Hansen, J. –K., Bremer, J. and Hunderi, O., *Phys. Rev. B.* **76** (2007) 115403
- [18] Winsemius, P., van Kampen, F. F., Lengkeek, H. P. and van Went, C. G., *J. Phys. F: Metal Phys.* **6** (1976) 1583
- [19] Colavita, E., Modesti, S. and Rosei, R., *Phys. Rev. B.* **14** (1976) 3415
- [20] Weightman, P., Dolan, G. J., Smith, C. I., Cuquerella, M. C., Almond, N. J., Farrell, T., Fernig, D. G., Edwards, C. and Martin, D. S., *Phys. Rev. Lett.* **96** (2006) 086102
- [21] Macdonald, B. F. and Cole, R. J., *Appl. Phys. Lett.* **80** (2002) 3527
- [22] Macdonald, B. F., Law, J. S. and Cole, R. J., *J. Appl. Phys.* **93** (2003) 3320
- [23] Barritt, E. E., Smith, C. I., Martin, D. S., Gentz, K., Wandelt, K. and Weightman, P., *Journal of Physics: Conference Series* **286** (2011) 012028
- [24] Fernandez, Y., Pahlke, D., Esser, N., Stahrenberg, K., Hunderi, O., Bradshaw, A. M. and Richter, W., *Surf. Sci.* **377** (1997) 388
- [25] Kolb, D. M., Boeck, W., Ho, K. –M. and Liu, S. H., *Phys. Rev. Lett.* **47** (1981) 1921
- [26] Barritt, E. E., Smith, C. I., Martin, D. S., Gentz, K., Wandelt, K. and Weightman, P., *EPL* **92** (2010) 57005

## **Chapter 6**

### **The Cu(110) Surface**

## 6.1 Introduction

The Cu(110) surface studied in this research is one of the low Miller index surfaces of the copper face centred cubic (fcc) crystal structure. The (110) surface is the most open of the low index surface. It has the lowest atomic density and the highest surface energy. The Cu(110) surface oxidises easily in air and although the other low index faces of copper, the (100) or (111) surfaces, are less easily oxidised, they are isotropic surface structures which do not yield RA spectra.

Following the preparation of the clean Cu(110) surface using one of the methods described in section 3.4, the Cu(110) surface has an anisotropic surface structure which is necessary for monitoring surface sensitivity using reflection anisotropy spectroscopy (RAS). This intrinsic surface anisotropy gives rise to well defined features in the RA spectrum which are well understood.

This research will focus initially on the well understood surface structure of the Cu(110) surface before attempting to mimic the surface structure observed in ultra high vacuum (UHV) in ambient conditions using electrochemistry. This will provide important information into material and surface behaviour and also to facilitate the understanding of the electrical double layer induced by the electrode and solution in electrochemical environments.

## 6.2 The Physical Structure of the Cu(110) Surface

The physical structure of the Cu(110) surface is a straight forward termination of the bulk crystal lattice. It does not show the well defined surface reconstructions observed on the Au(110) surface which can exhibit either an unreconstructed (1x1) surface, a reconstructed (1x2) surface and a reconstructed (1x3) surface. A review of the literature of the Au(110) surface reconstructions has been conducted by Almond [1].

In the absence of any reconstructions on the Cu(110) surface there are some physical changes the surface experiences due to oxidation and thermal effects which need to be understood.

The Cu(110) surface oxidises very easily in atmosphere. When the surface is exposed to 10-30 langmuir (L) of atomic oxygen a p(2x1) superstructure [2] is observed with oxygen coverage of 0.5 monolayers [3]. The oxygen chemisorbs to the Cu(110) surface and at this coverage a saturation phase occurs [4]. During the oxygen exposure there is a growth of CuO chains parallel to the [001] direction as seen in figure 6.1.

This text box is where the unabridged thesis included the following third party copyrighted material:

Tsukahara, N., Noto, K., Ohara, M., Shiraki, S., Takagi, N., Takata, Y., Miyawaki, J., Taguchi, M., Chainani, A., Shin, S. and Kawai, M., *Phys. Rev. Lett.* **102** (2009) 167203

**Figure 6.1: The Cu(110) surface with CuO chains parallel to the [001] direction. This surface was exposed to air and then heated to 400 K [5]. The Cu atoms are the red circles and the O atoms are the blue circles.**

The chemisorption of oxygen molecules onto the Cu(110) surface will change the electronic structure compared to that of a clean Cu(110) surface. The oxygen covered surface will not be discussed in detail in this work but it has been investigated using angle resolved photoemission [4,6,7] and inverse photoemission [8,9] along with theoretical calculations [10,11].

The Cu(110) surface also experiences physical changes when subjected to high temperatures. Although permanent changes are only observed at temperatures

higher than 900 K [12]. Below this temperature, in the range 550-900 K, X-ray [13] and helium scattering [14] results revealed a strongly enhanced mean square displacement of surface atoms but with no change in defect or step density. However, at 900 K irreversible physical changes occur due to the creation of adatom-vacancy pairs. At even higher temperatures around 1000 K a roughening transition occurs [15,16]. Physically this transition is observed as monoatomic steps generated across the surface and these steps will change the electronic structure of the Cu(110) surface.

The physical structure of the Cu(110) surface given by the arrangement of atoms on the surface has a strong influence on the electronic structure of the surface. It is therefore important to consider the electronic structure of the Cu(110) surface.

### **6.3 The Electronic Structure of Copper**

The RA spectrum of the Cu(110) surface has been interpreted in terms of single particle excitations between the states of its band structure. Experimental techniques such as electoreflectance spectroscopy (ERS) enable the band structure of materials to be mapped accurately. ERS measurements [17] are sensitive to the anisotropy of the Cu(110) surface and showed that the states occupied with surface electrons are sensitive to the distribution of the atoms on the surface. Theoretical calculations can facilitate an understanding of the full band structure of the surface which can be compared with the experimental studies. Generally the calculations are based on calculations of the bulk electronic structure within a pseudopotential approach.

This text box is where the unabridged thesis included the following third party copyrighted material:

Marder, M. P., Condensed Matter Physics, Second Edition. (John Wiley & Sons Inc, Hoboken) 2010

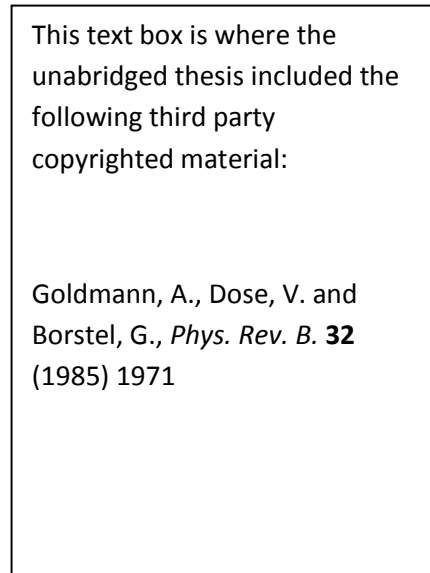
**Figure 6.2: Energy bands of copper as calculated from [18,19] with the picture taken from [20].**

Figure 6.2 shows the energy bands of an fcc copper crystal. These correspond to the results expected for a nearly free electron solid since the closed shells of the d valence electrons are rather localised and the 4s conduction electrons are delocalised. Overall copper has an electron configuration of  $[\text{Ar}]3d^{10}4s^1$  where  $[\text{Ar}]$  is the electron configuration of argon ( $1s^2 2s^2 2p^6 3s^2 3p^6$ ). The dotted line in figure 6.2 represents the Fermi energy and the position of the bands are calculated relative to it. The 3d electrons occupy narrow bands around 2.00 eV below the Fermi surface with the 4s electron occupying the broader band from around 10.00 eV below the Fermi surface to several electron volts above the Fermi surface.

### **6.3.1 The Electronic Structure of the Cu(110) Surface**

As this research focuses on the Cu(110) surface it is necessary to extend the understanding of the bulk band structure to the surface which will become important when trying to understand adsorption processes and corrosion. The surface behaves differently to the bulk since surface atoms do not have the three dimensional environment as the bulk. As mentioned in section 2.3.2 surface states exist only at the surface and can play an important role in surface behaviour. Slightly different techniques have been used to study the surface band structure such as high resolution photoemission [21,22], inverse photoemission [23,24] along with theoretical calculations [25,26]. These studies have shown the presence of

occupied and unoccupied intrinsic surface bands within the band gap. These surface bands have been found around the Fermi energy at different points in the surface Brillouin zone. The Cu(110) surface band structure is shown in figure 6.3 which also shows results obtained with momentum resolved inverse photoemission spectroscopy at  $\hbar\omega = 9.7 \text{ eV}$  [23].



**Figure 6.3: The electronic structure of the Cu(110) surface [23].**

In figure 6.3 the states labelled  $S_1$  are image potential states and the states labelled B arise from the bulk band structure. The image potential states arise from the image binding potential which acts on the electrons on the vacuum side, V, of the Cu(110) surface [25]. The intrinsic surface states are given by  $S_2$ ,  $S_3$  and  $S_4$ . Two of these states,  $S_2$  and  $S_3$ , lie along the  $\bar{Y}$  direction of the surface Brillouin zone and form an unoccupied state with  $S_2 \sim 1.80 \text{ eV}$  above the Fermi energy. The  $S_3$  state is occupied for a small region of k space near the  $\bar{Y}$  point at  $\sim 0.40 \text{ eV}$  below the Fermi energy. There are two further unoccupied surface states at the  $\bar{X}$  point. It is interesting to note that the band gap at the  $\bar{Y}$  point overlaps the Fermi energy whereas at the  $\bar{X}$  point the band gap is above the Fermi energy. At the  $\bar{\Gamma}$  point there is no band gap around the Fermi energy. The surface states at the  $\bar{Y}$  point have localised wavefunctions at the Cu(110) surface [24] and so are sensitive to

thermal changes at the surface. Straube *et al* [22] found the occupied surface state energy varies linearly with temperature. This will mean that the electronic structure of the surface will be highly temperature dependent. Since the Cu(110) surface possesses two different mirror planes, [001] and  $[1\bar{1}0]$ , optical transitions occurring in the surface will depend on the polarisation of the incident light. The polarisation that excites a transition will also depend on the symmetry and parity of the initial and final states. For an allowed optical transition the orbital quantum number condition,  $\Delta l = \pm 1$ , must be obeyed. Hence an optical transition only occurs at these points in the surface Brillouin zone if there is an even and odd state with respect to the reflection in a plane perpendicular to the polarisation of the E vector of the incident light. This will be an important feature of the results presented in this research. A full consideration of the transition selection rules are covered by Jiang *et al* [25]. Photoemission, inverse photoemission and theoretical calculations have formed the basis of the understanding of the electronic structure of the Cu(110) surface. More recently RAS has been used to explore the electronic structure of the surface and its response to the surface environment.

## **6.4 Reflection Anisotropy Spectroscopy of the Cu(110) Surface**

As described in chapter three RAS offers a relatively new way to probe surfaces, observing not only the electronic structure but also any physical changes to the surface. The RA spectrum of the Cu(110) surface at room temperature is shown in figure 6.4. There are three main features in the RA spectrum labelled a, b and c at 2.10 eV, ~4.30 eV and 4.90 eV respectively.



This text box is where the unabridged thesis included the following third party copyrighted material:

Weightman, P., Martin, D. S.,  
Cole, R. J. and Farrell, T., *Rep.  
Prog. Phys.* **68** (2005) 1251

**Figure 6.4: RA spectrum of the Cu(110) surface at room temperature [27].**

The strong feature, a, at 2.10 eV, around 0.25 eV wide, is known to be associated with a transition between surface states at the  $\bar{Y}$  point of the surface Brillouin zone between the occupied state  $\sim 0.40$  eV below the Fermi level and an unoccupied state  $\sim 1.80$  eV above the Fermi level [28]. This has also been confirmed using second-harmonic generation spectroscopy [29]. Although this transition between surface states is the main contribution to the 2.10 eV peak there are also contributions from surface modified interband transitions near the  $\bar{X}$  point of the bulk Brillouin zone and a 'Drude' term associated with anisotropic free electron transport in the surface [30-32]. As discussed in section 3.2 the light incident on the surface during RAS experiments can be described with respect to the E vector. It is this E vector that induces a dipole transition between an occupied initial state and unoccupied final state [27]. Since the Cu(110) surface is anisotropic the transition induced will be dependent on the polarisation of the light [25]. In this case, at the  $\bar{Y}$  point the occupied surface state has  $p_y$  character and the unoccupied state ( $s + p_z$ ) character with respect to the surface copper atoms. Furthermore the ( $s + p_z$ ) type states will have even symmetry in the  $[001]$  and  $[1\bar{1}0]$  directions on the Cu(110) surface whereas the  $p_y$  type states will be even in the  $[1\bar{1}0]$  direction but odd in the  $[001]$  direction. This affects the transition between surface states because for a transition to occur one of the states involved must be even in symmetry whereas

the other must be odd. Hence the surface state transition at the  $\bar{Y}$  point of the surface Brillouin zone will only be induced by light polarised in the  $[001]$  direction. The s and p characters mentioned refer to the atomic orbitals which describe the position of the electrons. The s orbitals do not have any subshells and are spherical in shape. However the p orbitals have 3 subshells in the x, y and z directions orthogonal to each other and have a lobed shape. In this case the y and z directions are taken to be in the surface plane. It is possible for the orbitals to possess a mixture of character types when an s orbital interacts with one of the  $p_x$ ,  $p_y$  or  $p_z$  orbitals. As a result, surface states can be observed to have (s+ $p_z$ ) character, which occurs in this case.

The higher energy features, b and c, arise from transitions around the L point of the Brillouin zone [33]. Specifically peak b is thought to be an optical transition between the Fermi level and empty  $L_1^u$  state and peak c involves transitions from states  $L_2' \rightarrow L_1^u$ . The L high symmetry point can be seen in figure 2.4 in the bulk Brillouin zone and in relation to the surface Brillouin zone in figure 2.8.

The assignment of these transitions is supported by calculations using density-functional theory and the local density approximation (DFT-LDA) [34] which find the features around 4.00 eV to be due to bulk-state to bulk-state transitions. The features b and c have been shown to be sensitive to surface morphology and atomic order. Martin *et al* [30] observed that the RA signal for peak b is enhanced due to steps with rough edges aligned along the  $[001]$  direction and Baumberger *et al* [35] observed that the intensity and sign of this feature is dependent upon step density and coordination number of step atoms respectively. In general these changes in the physical surface arise from thermal treatment or Ar bombardment which are directly linked to the RA signal around 4.00 eV.

#### 6.4.1 Reflection Anisotropy Spectroscopy as a Monitor of Surface States

Figure 6.4 shows a transition between surface states at 2.10 eV which is expected to be sensitive to changes in the surface structure and behaviour. Studies have been performed observing how this transition is affected when the temperature of the surface is increased. This temperature dependence is shown in figure 6.5. It is immediately clear the transition between surface states at 2.10 eV decreases in energy at higher temperatures before becoming a much broader feature at around 850 K. Figure 6.5 also shows there is an energy shift of  $\sim 0.10$  eV in the transition peak at 2.10 eV as the temperature is increased from 180 K to 1060 K. This is linked to the dependence on temperature of the occupied surface state as mentioned earlier [22]. The reduction in the intensity of the feature at 2.10 eV with increasing temperature is explained using the knowledge of the band structure of the Cu(110) surface. Since the occupied surface state is only  $\sim 0.40$  eV below the Fermi level, as the temperature is increased to 615 K this state will approach the Fermi level causing a depopulation of the state as the electrons gain thermal energy. At even higher temperatures up to 850 K anharmonic vibrations cause disorder on the Cu(110) surface [12,36]. Moving up to even higher temperatures around 900 K to 1000 K, around the roughening transition temperature, a shoulder feature develops in the RA spectrum at around 2.20 eV. The disorder on the surface is due to adatom-vacancy pairs as previously discussed. At temperatures lower than the roughening transition temperature, up to  $\sim 1000$  K, when the surface is cooled back to room temperature the 2.10 eV feature in the RA spectrum is observable at the same intensity as the original room temperature measurements. However, after the roughening transition there is an irreversible loss of the 2.10 eV peak.

This text box is where the unabridged thesis included the following third party copyrighted material:

Martin, D. S., Maunder, A. and Weightman, P., *Phys. Rev. B.* **63** (2001) 115403

**Figure 6.5: RA spectra of experimental and simulated (bold line) data for the Cu(110) surface as a function of temperature including the surface local field effect (SLFE) model RA spectra [30].**

The results shown in figure 6.5 confirm that RAS is a sensitive monitor of surface morphology and also surface states. Scanning tunnelling microscopy (STM) images shown in figure 6.6 have been taken of the clean Cu(110) surface and the Cu(110) surface after the roughening transition. These images show the roughening transition induces a high density of monoatomic height steps in the  $[001]$  direction that terminate terraces of  $\sim 5$  nm in the  $[1\bar{1}0]$  direction. As a consequence, the large negative feature at  $\sim 4.20$  eV in the RA spectrum is enhanced with increasing temperature since this feature is dependent on surface roughness. The disappearance of the surface state transition at 2.10 eV is also a result of the presence of the terraces since the narrow width of the terraces causes a

depopulation of the surface state transition as the energy has been raised above the Fermi level by quantum confinement of the state on the narrow terrace [30].

This text box is where the unabridged thesis included the following third party copyrighted material:

Martin, D. S., Maunder, A. and Weightman, P., *Phys. Rev. B.* **63** (2001) 115403

**Figure 6.6: Scanning tunneling microscope images of the (a) clean Cu(110) surface and (b) thermally roughened surface as the temperature has risen to 1060 K [30].**

An advantage of the depopulation of the surface state is the ability to observe the other contributions to the transition at 2.10 eV. These contributions arise from the surface local field effect as demonstrated by theoretical work using the screened local field effect model [37]. This assumes that the d electrons are localised around the ionic core of the atoms and the s-p electrons are delocalised [38]. The contribution from the conduction electrons, in between the ‘sphere of d electrons’, can then be modelled using a screening Drude term. This approach does not account for the negative peak at ~4.00 eV which may be due to this feature being heavily dependent on monoatomic steps.

Since surface states are highly localised at the metal surface they are extremely sensitive to surface contamination in UHV. As mentioned the Cu(110) surface oxidises easily so it is important to understand how the adsorption of molecules also affects the surface state.

Oxygen adsorption [39] on the Cu(110) surface gives rise to a Cu(110)-(2x1)-O surface as described in 6.2. The oxygen adsorption causes the strong transition at 2.10 eV to reduce in intensity and leads to the observation of a double peak which

suggests new surface states have been introduced. The loss of intensity of the 2.10 eV transition is due to the occupied surface state band being shifted upwards in energy by 0.70 eV so the band will then lie 0.30 eV above the Fermi level [40].

There are similar responses when CO molecules are adsorbed [41] or other organic molecules such as 3-thiophene carboxylate [42] and terephthalic acid [31]. The effect of ambient air also changes the Cu(110) structure. This is shown in the RA spectra in figure 6.7 for a polished Cu(110) surface in ambient air, upper plot, and the lower plot shows the RA spectra of the clean and stepped Cu(110) surface in UHV (open circles) and following exposure to ambient air (filled circles) [43]. The XPS data to compliment the RAS data indicates the formation of a cuprous oxide,  $\text{Cu}_2\text{O}$  overlayer. The crosses shown in figure 6.7 illustrate the stimulated spectrum which has been calculated using the three layer model. These transitions around 3.50 eV and 4.30 eV have been found to be dominated by transitions involving bulk bands which are anisotropically modified by the surface layer and show good agreement with the experimental data.

This text box is where the unabridged thesis included the following third party copyrighted material:

Isted, G. E. and Martin, D. S.,  
*Appl. Surf. Sci.* **252** (2005) 1883

**Figure 6.7:** RA spectra of (upper figure) the polished Cu(110) surface in ambient air and (lower figure) clean and stepped Cu(110) surface in UHV (open circles) and following exposure to ambient air (closed circles). The crosses show the simulated spectrum [43].

The discussion of the Cu(110) surface has thus far focused on the behaviour of surface states in UHV conditions. However, the aim of this research is to observe these surface states in an electrochemical environment so the discussion will now move to the study of surface states electrochemically.

## 6.5 The Metal/Liquid Interface

The metal/liquid interface is an important interface to understand since it is common in nature and plays a central role in many chemical processes such as catalysis, corrosion and electrochemistry. During this research the metal/liquid

interface will be studied using electrochemistry which has been described in section 3.3. Despite recent advances [44,45] there is a need to develop the theoretical understanding of the metal/liquid interface and also to apply experimental techniques that will provide information about the electronic structure of the electric double layer that exists at the interface between the electrode and solution.

#### **6.5.1 Surface States at the Metal/Liquid Interface**

Since surface states are known to be extremely sensitive to surface contamination in UHV it might be expected that they would not exist at the metal/liquid interface. The first evidence for surface states at this interface was performed using electroreflectance (ER) measurements. These had been extended into the infrared range and studied the Ag(100)/electrolyte interface [46,47]. This initial work used an electrolyte of 0.5 M NaF although it was later shown that the ER results are influenced by the concentration of the electrolyte and the presence of adsorbed species at the electrode [48]. ER measures the relative change in the reflectance of the surface,  $\Delta R/R$ , but differs from RAS as it is measured along a single crystallographic direction as a function of the potential applied to the electrode. In order to increase sensitivity the applied potential is modulated at high frequency,  $\sim 180$  Hz, to give a derivative lineshape. Further studies were performed on all of the low index faces of silver [49] which again show potential dependent features.

#### **6.5.2 Reflection Anisotropy Spectroscopy of the Metal/Liquid Interface**

RAS can be used to study surfaces in UHV and in a variety of environments such as at the metal/liquid interface. Its disadvantage compared to ER measurements is that it requires the surface to be anisotropic which limits its use to these such surfaces. However, RAS is sensitive to the surface and has no contribution from the bulk. Contributions from the bulk electronic structure can cause problems in ER measurements. Mazine *et al* [50] provided the first studies of the metal/liquid interface using Au(110) and an electrolyte of Na<sub>2</sub>SO<sub>4</sub> to study surface



reconstructions of the Au(110) surface and it was observed the surface reconstructions are dependent on the applied potential. Work has progressed on the Au(110) surface using different electrolytes such as H<sub>2</sub>SO<sub>4</sub> [51] to get a good understanding of the surface reconstructions and how the RA spectrum are sensitive to the surface morphology.

The combination of electrochemistry and RAS has been applied to the study of the molecular adsorption of organic molecules such as pyridine [52] on Au(110). Other studies utilised the ADRAS technique to study the orientation of DNA molecules on Au(110) surfaces [53,54].

In this research the first application of RAS is made to study the Cu(110) surface in a liquid environment.

## **6.6 The Cu(110)/Liquid Interface**

The remainder of this chapter will discuss the Cu(110)/liquid interface which is already well understood in UHV and where RAS has been used as a sensitive monitor of surface states. By developing a good understanding of the Cu(110)/liquid interface this will advance the understanding of corrosion and facilitate the development of biocompatible materials. Copper is an ideal material to use as a metal electrode since it can be applied to a wide range of applications due to its high electrical and thermal conductivities alongside its relatively cheap cost when compared to metals such as gold. It is also a good metal to use in surface state studies as the surface atoms do not reconstruct as readily as the Au(110) surface.

The initial results presented will show the investigations on the interface in a non-electrochemical environment before moving on to the electrochemical studies in the latter part of the chapter. For all results discussed the experimental set up is as described in section 3.4 using the electropolishing method unless stated otherwise.

### 6.6.1 The Cu(110)/Liquid Interface using H<sub>2</sub>O or H<sub>2</sub>SO<sub>4</sub> solutions

During the experiments with H<sub>2</sub>O and 10 mM H<sub>2</sub>SO<sub>4</sub> the copper crystal was positioned within the electrochemical cell but no potential was applied. In this situation the electrochemical cell has been used so the Cu(110) surface is stable and also so it can be placed within an argon chamber. The RA spectra for the Cu(110)/H<sub>2</sub>O and Cu(110)/H<sub>2</sub>SO<sub>4</sub> interfaces are shown in figure 6.8. These spectral profiles are similar, both show a positive peak  $\sim 0.25$  eV wide around 2.20 eV with a steady fall into a negative peak around 4.30 eV. The peak centred around 2.20 eV has a similar peak width as the transition between surface states observed in UHV at the  $\bar{Y}$  point of the surface Brillouin zone but is 0.10 eV higher in energy. A full discussion of the origin of this peak will be considered later but it is encouraging that the initial RAS investigations observe a feature that in some ways resemble the transition profile, as observed in UHV environments. The large negative peak at  $\sim 4.30$  eV has a similar profile to the feature at a similar energy observed on the thermally roughened Cu(110) surface in UHV and a full discussion of the intensity and origin of this feature will also be given later.

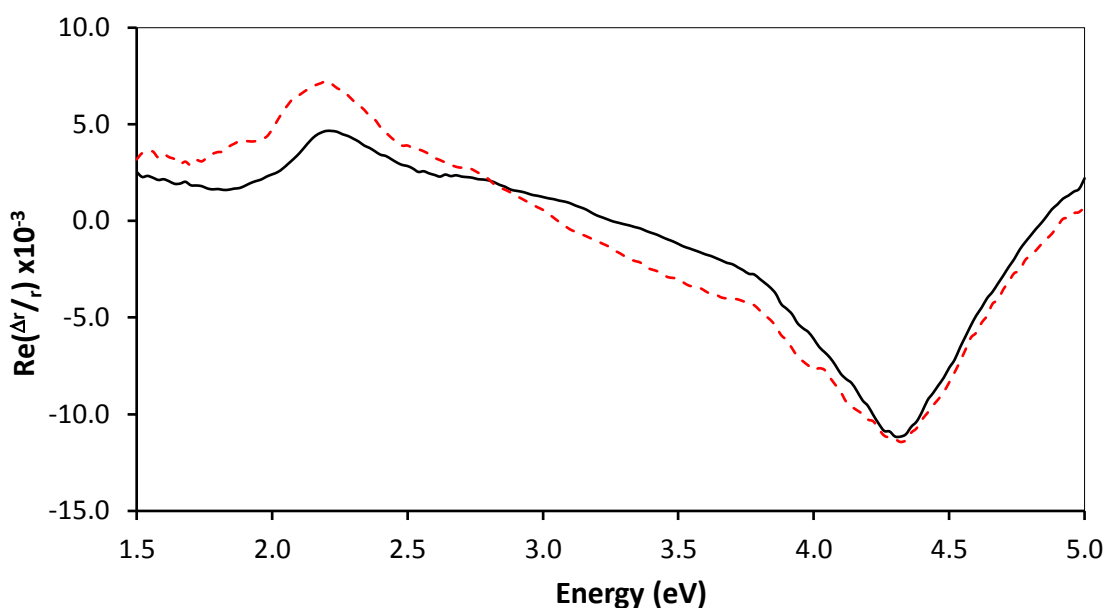
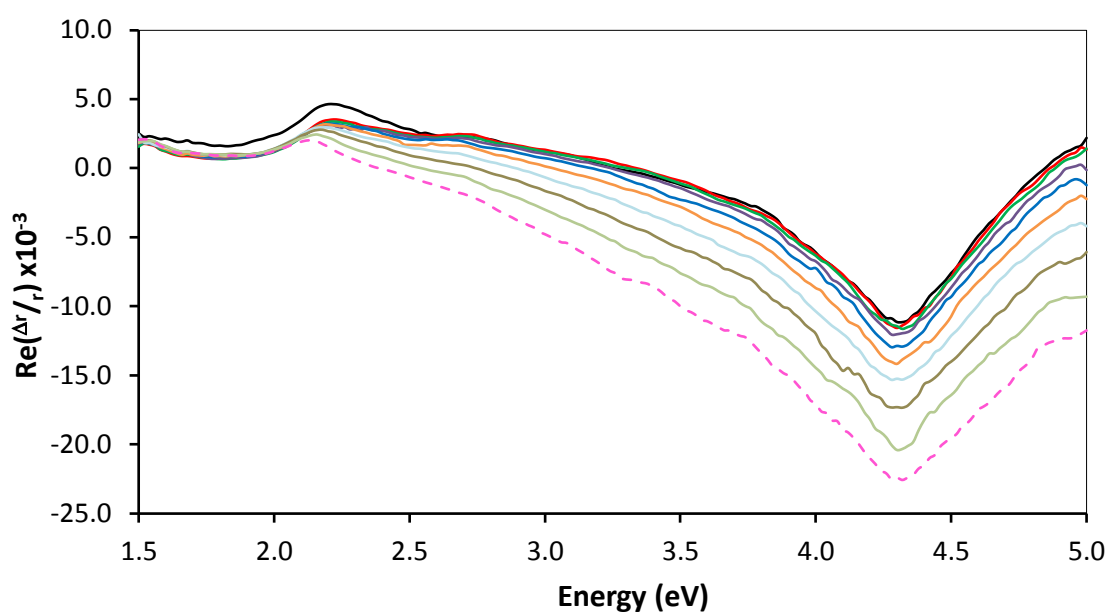
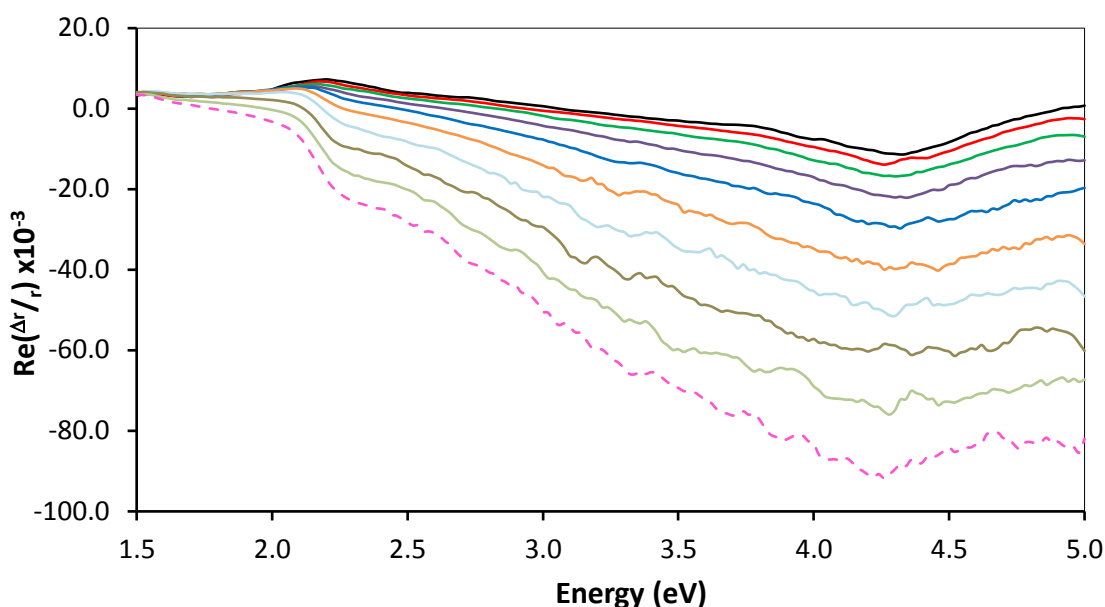


Figure 6.8: RA spectra of the Cu(110) surface in H<sub>2</sub>O (black line) and 10 mM H<sub>2</sub>SO<sub>4</sub> (red dashed line).

As shown in figures 6.9 and 6.10 when the Cu(110) surface is submerged in H<sub>2</sub>O or 10 mM H<sub>2</sub>SO<sub>4</sub> respectively the surface is unstable. In both figures the initial spectra are the black lines with increasing time periods of 10 minutes until 90 minutes which is the pink line. The peak at ~4.30 eV increases over time and doubled in intensity after 90 minutes in H<sub>2</sub>O and increased fourfold in H<sub>2</sub>SO<sub>4</sub> over the same time period. This instability is attributed to the high reactivity of the Cu(110)/liquid interface [55,56] and the tendency of the Cu(110) surface to oxidise. Over the 90 minute timescale of the experiments the Cu(110)/H<sub>2</sub>O and Cu(110)/H<sub>2</sub>SO<sub>4</sub> interfaces do not yield an equilibrium RAS profile.



**Figure 6.9: RA spectra of the Cu(110) surface in H<sub>2</sub>O over a time period of 90 minutes. From an initial time (black line) and every 10 minutes until 90 minutes (pink dashed line).**



**Figure 6.10:** RA spectra of the Cu(110) surface in 10 mM H<sub>2</sub>SO<sub>4</sub> over a time period of 90 minutes. From an initial time (black line) and every 10 minutes until 90 minutes (pink dashed line).

### 6.6.2 The Cu(110)/Liquid Interface using a 5 mM H<sub>2</sub>SO<sub>4</sub> + 10 mM KBr solution

Since the electrochemical cell used in these experiments employed a silver/silver halide reference electrode the electrolyte used must contain a halide element for the electrochemistry to be used successfully. Here, the electrolyte used is 5 mM H<sub>2</sub>SO<sub>4</sub> + 10 mM KBr complying with this rule. The bromide atoms stabilise the surface avoiding the instability that is seen when using H<sub>2</sub>O or H<sub>2</sub>SO<sub>4</sub> but also allowing the process of electrochemistry to be utilised. By changing the applied potential across the Cu(110) surface, which acts as the working electrode, the Br<sup>-</sup> atoms are either adsorbed or desorbed on the surface. Obliers *et al* [57] performed cyclic voltammograms (CV) showing that the potential at which the Br<sup>-</sup> atoms adsorb on the surface is -0.52 V vs Ag/AgBr when the potential is scanned in the positive direction and desorbs off the surface at -0.56 V vs Ag/AgBr when the potential is scanned in the negative direction. All potentials are quoted referenced to this reference electrode, Ag/AgBr.

Figure 6.11 shows the RA spectra at -0.35 V and -0.65 V when the  $\text{Br}^-$  atoms are adsorbed and desorbed to the surface respectively. At -0.65 V the surface should be free of  $\text{Br}^-$  atoms and the transition observed at 2.10 eV from previous RAS experiments in UHV should be observable. However, there is no peak in the spectrum at 2.10 eV although both spectra do show the negative feature at 4.30 eV. This could be because the feature at 4.30 eV is attributed to transitions around the L point of the bulk Brillouin zone and not transitions around the surface Brillouin zone. The fact that the transition at 2.10 eV is not observed in this environment is attributed to the  $\text{Br}^-$  atoms being too strongly bonded to the Cu(110) surface quenching the surface states. The  $\text{Br}^-$  atoms specifically adsorb to the Cu(110) surface via a partly covalent bond with most of the electron density around the bromide ion.

By using a halide solution which does not bond so strongly to the Cu(110) surface such as chlorine it is thought that the adsorbate will not quench the surface states and the strong feature  $\sim 2.10$  eV can be observed.

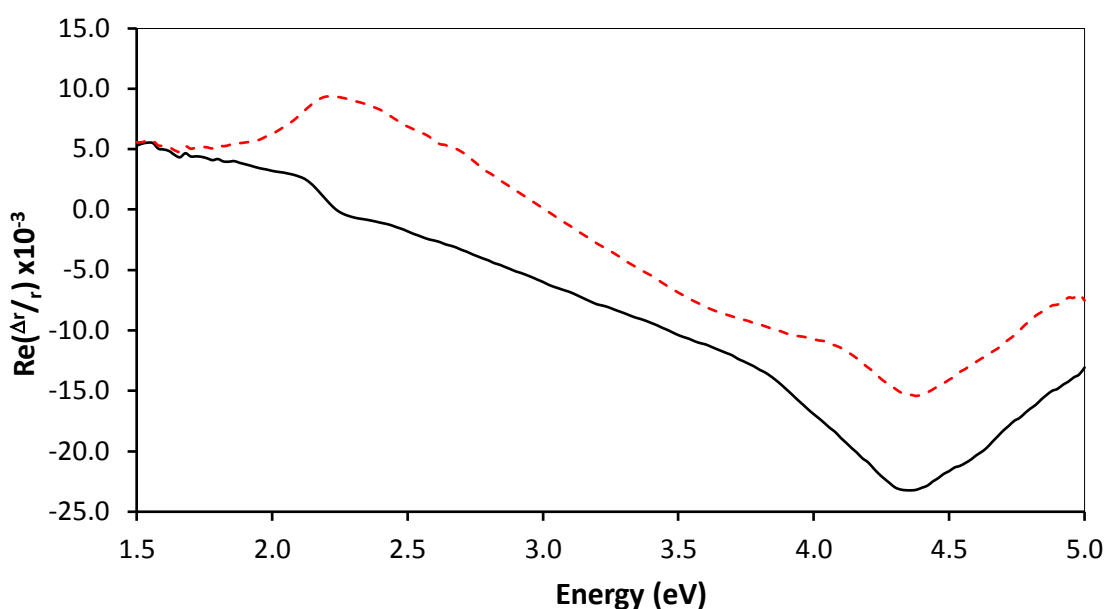


Figure 6.11: RA spectra of the Cu(110) surface in 5 mM  $\text{H}_2\text{SO}_4$  + 10 mM KBr at -0.35 V (red dashed line) and -0.65 V (black line).

### 6.6.3 The Cu(110)/Liquid Interface using a 10 mM HCl solution

Chlorine is directly above bromine in the periodic table and so is still a halide element but should bond less strongly to the Cu(110) surface and therefore be more suited to the electrochemistry experiments. A solution of 10 mM HCl is used and cyclic voltammograms are performed to show the potential at which the  $\text{Cl}^-$  atoms adsorb and desorb on or off the surface. Figure 6.12 shows the CV of the Cu(110)/HCl interface and it shows that  $\text{Cl}^-$  atoms adsorb on the surface at  $-0.40\text{ V}$  vs Ag/AgCl when the potential is scanned in the positive direction and desorbs from the surface at  $-0.43\text{ V}$  vs Ag/AgCl when the potential is scanned in the negative direction. Since chlorine is now being used as the halide the potentials are now quoted referenced to the Ag/AgCl reference electrode. The CV shows there is a window in which the Cu(110) surface is free from  $\text{Cl}^-$  atoms. Figure 6.12 also shows the potential cannot be increased to more positive potentials beyond  $\sim -0.05\text{ V}$  as this is the region where anodic copper dissolution begins or the potential cannot be decreased to more negative potentials beyond  $-0.82\text{ V}$  as hydrogen evolution takes place at these more negative values.

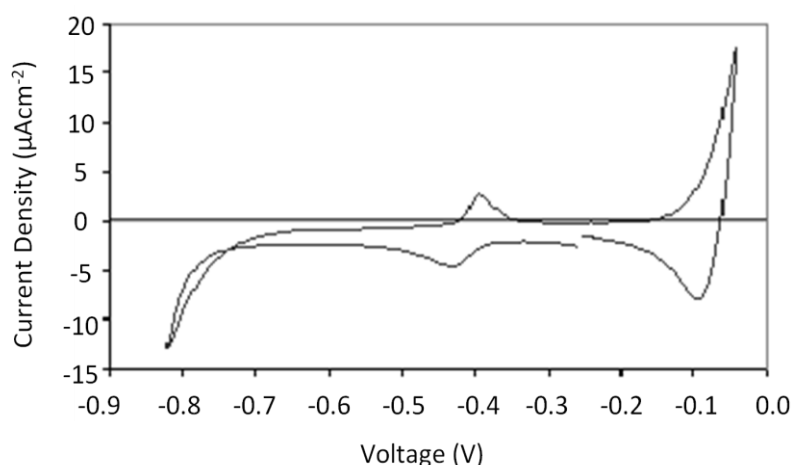
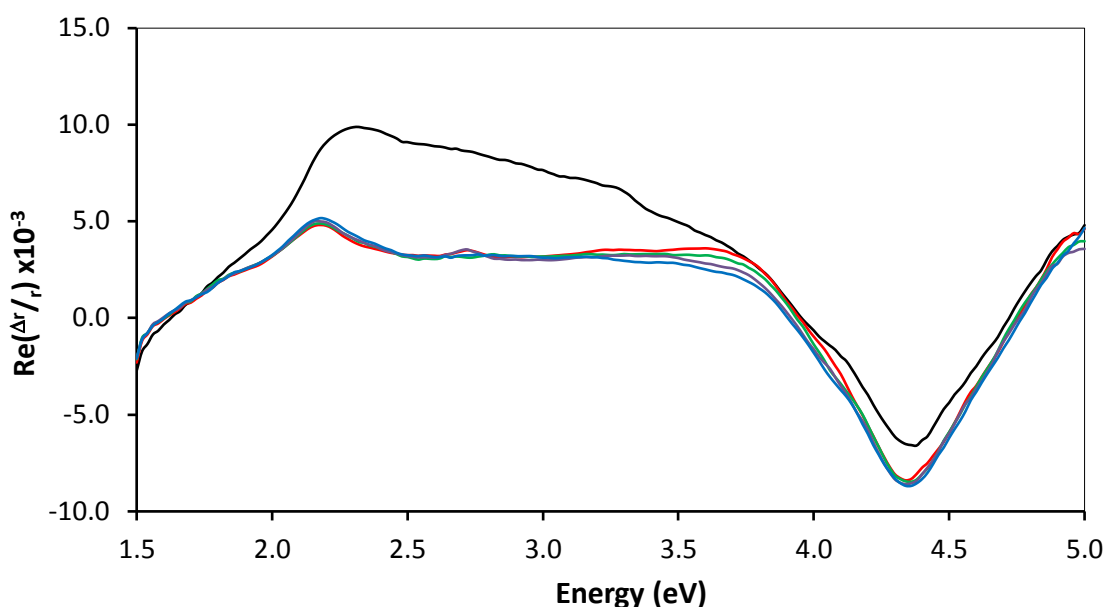
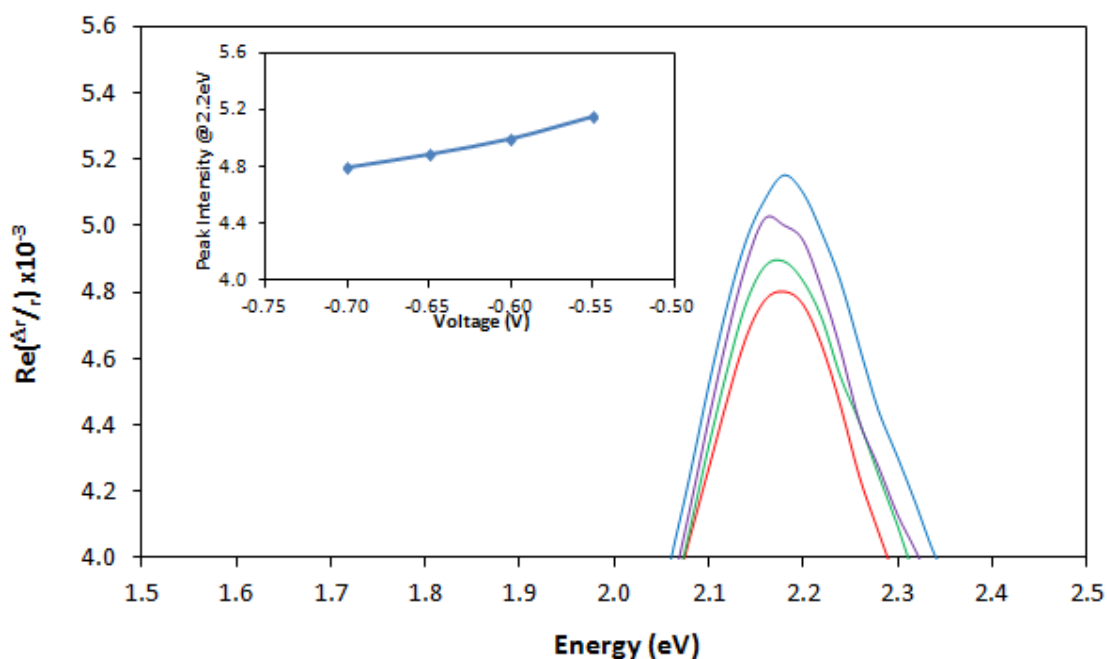


Figure 6.12: Cyclic voltammogram of Cu(110) in 10mM HCl recorded at a scan rate of  $10\text{ mVs}^{-1}$ [58].



**Figure 6.13:** RA spectra for the Cu(110) surface in 10 mM HCl at -0.35 V (black line), -0.55 V (blue line), -0.60 V (purple line), -0.65 V (green line) and -0.70 V (red line).

Figure 6.13 shows the RA spectra at applied potentials -0.70 V, -0.65 V, -0.60 V and -0.55 V when the Cu(110) surface is free from  $\text{Cl}^-$  adsorption and also at -0.35 V when the  $\text{Cl}^-$  atoms are adsorbed on the surface. The RA spectra at potentials more negative than -0.50 V are similar and are also comparable to the spectra in  $\text{H}_2\text{O}$  and 10 mM  $\text{H}_2\text{SO}_4$  with a rising signal from 1.50 eV reaching a peak at 2.20 eV. Subsequently the profiles in figure 6.13 for the  $\text{Cl}^-$  atom free surface remains largely flat before descending into a negative feature at  $\sim 4.30$  eV. There is also a weak feature shown in figure 6.13 at  $\sim 2.70$  eV which arises from a sharp peak in the output of the Xe lamp at this energy which, due to the less than perfect optical elements does not cancel completely in the ratio given in equation 3.1. Figure 6.14 shows the 2.20 eV peak in more detail with the inset showing the intensity of the peak as a function of potential applied. It is observed that as the potential is increased in the positive direction the intensity of the RA spectra increases. Although there is no shift in the peak position as a function of potential the half width of the peak increases from  $\sim 0.20$  eV to  $\sim 0.25$  eV which is more similar to the width found in UHV studies of the clean Cu(110) surface.



**Figure 6.14:** RA spectra of the Cu(110) surface in 10 mM HCl zoomed in around the 2.2 eV peak at -0.55 V (blue line), -0.60 V (purple line), -0.65 V (green line) and at -0.70 V (red line). The inset shows the RA intensity as a function of applied potential.

For comparison purposes, the RA profiles of the Cu(110) surface in various environments is shown in figure 6.15. Although the peak observed at 2.20 eV in H<sub>2</sub>O (c), H<sub>2</sub>SO<sub>4</sub> (d) and at potentials more negative than -0.50 V in HCl (f) has greatly reduced in intensity when compared to the well prepared Cu(110) surface in UHV (a) the lineshape and linewidths are more similar than when compared to the lineshape of the thermally roughened spectrum (b) as shown in the inset to figure 6.15.



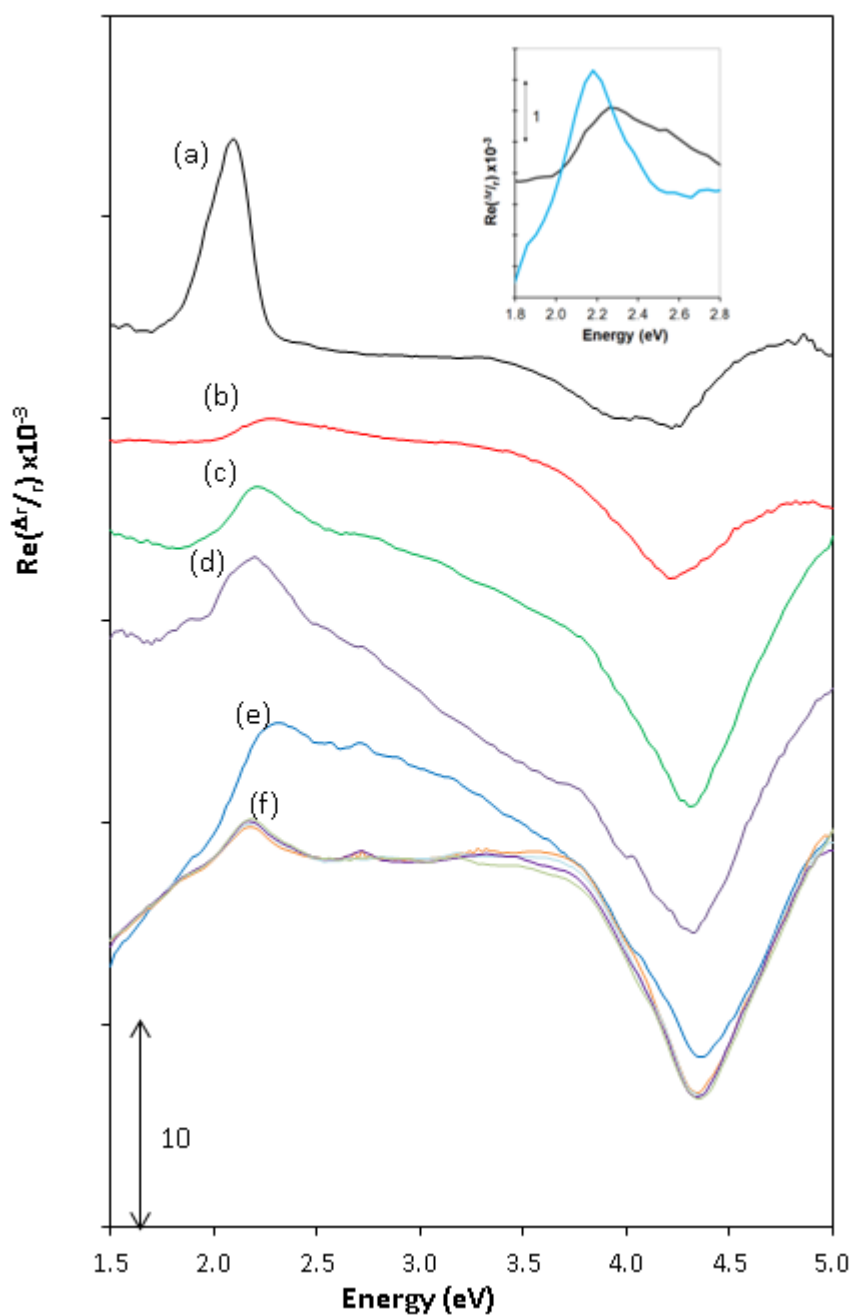


**Figure 6.15: RA spectra of the Cu(110) surface in (a) UHV, (b) the thermally roughened Cu(110) surface, (c) in H<sub>2</sub>O, (d) in 10 mM H<sub>2</sub>SO<sub>4</sub>, and in 10 mM HCl at (e) -0.35 V and (f) at voltages between -0.55 V and -0.70 V.**

The peak observed at 2.20 eV in the RA spectra in H<sub>2</sub>O, H<sub>2</sub>SO<sub>4</sub> and HCl at potentials below -0.50 V (figure 6.15 (c), (d) and (f) respectively) is 0.10 eV higher in energy

than the transition between surface states observed from the well prepared Cu(110) surface in UHV (figure 6.15 (a)). The shift could arise from an overlap with the asymmetric spectrum of the other two contributions to the RAS signal in this region of the spectrum (figure 6.15 (b)), as found from high temperature experiments [30]. Alternatively the 0.10 eV increase in energy could arise from moving out of an UHV environment into a liquid environment. Consequently, the 2.20 eV peak observed under a liquid is attributed to a transition between surface states at the  $\bar{Y}$  point of the surface Brillouin zone.

The thermally roughened Cu(110) surface and the surface in the three electrolytes between 3.50 eV and 5.00 eV show some similarities suggesting the electropolishing process produces an atomically rough surface and that this is the origin of the 4.30 eV feature. The high temperature thermal roughening process will give the Cu(110) surface more kinetic freedom than the electropolishing process with the likely result that in the latter case the terraces are less uniform. These differences in surface roughness could explain why the 2.20 eV transition between surface states is present in the RAS of the Cu(110)/electrolyte interfaces but not in that of the thermally roughened surface. As mentioned, the thermally roughened surface does not show transitions between surface states due to the depopulation of the initial state by surface confinement on the narrow terraces. The electropolished surfaces are expected to exhibit a wider range of terrace sizes resulting in the initial state being populated on some terraces thus giving rise to the transition though at a reduced intensity when compared to the RAS of well prepared Cu(110) surfaces in UHV. These terrace ranges are confirmed by *in situ* STM studies of electropolished Cu(110) surface. Figure 6.16 shows a 139 x 139 nm region with eleven terraces with widths ranging from 4 nm to 35 nm with five terraces of 10 nm width or less [58].

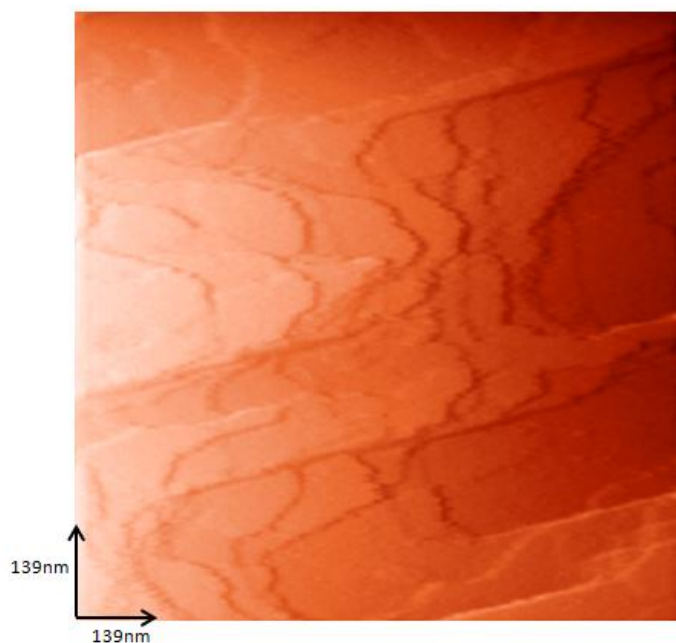


**Figure 6.16: Scanning tunneling microscope image of an electropolished Cu(110) surface in a liquid environment [58].**

The attribution of the 2.20 eV peak in liquid environments to the transition between surface states at the  $\bar{Y}$  point of the surface Brillouin zone can also be supported by considering ER measurements [17,60]. As discussed ER spectra are measured along a single crystallographic direction so for Cu(110) this will be along the [001] and  $[1\bar{1}0]$  directions. These measurements showed a feature at 2.20 eV observed in both directions followed by a broad feature at  $\sim 4.40$  eV only observed along the  $[1\bar{1}0]$  direction, which were attributed to interband transitions and differences in the surface conductivity in the different crystallographic directions. Using Ag and Au surfaces in liquid environments, transitions between d-band states and surface states have been observed and showed an increase in the energy of the transition as the applied potential is varied, in the positive direction, of  $0.9 \text{ eV V}^{-1}$  for Ag(100) and  $1.3 \text{ eV V}^{-1}$  for Ag(111) [48].

Since the d-bands inside the metal will be screened from the applied potential they will be much less affected by the applied potential than the surface states which will be more greatly responsive to the potential in the electric double layer

[46,48,61]. Thus, applying a potential for a transition between d-band states and surface states should result in a shift in transition energy whereas transitions between surface states should not. Figure 6.14 confirms that in this research there is no energy dependence on the applied potential for the transition between surface states at 2.20 eV and only a change in intensity. Further analysis of the Ag/liquid interface using ER [48] shows the surface states had broad widths of 0.6 eV to 0.8 eV which is expected when considering the sensitivity of surface states to variations in the local potential in the electrical double layer caused by small differences in the orientation of water dipoles [48,61]. However, as RAS is a local probe these variations in the potential in the electrical double layer will not broaden the transitions since the initial and final states involved will experience the same local potential. Hence the feature at 2.20 eV has a width of  $\sim 0.25$  eV which is much more similar to the profile of this transition at 2.10 eV observed in UHV.

The observation shown in figure 6.14 that the 2.20 eV peak increases in intensity with increasing potential in the positive direction ultimately means that there is either an increase in anisotropy, an increase in the intrinsic intensity of the transition or an increase in the number of sites giving rise to the transition as these are the factors that the RA spectra are dependent on. It is not clear how the change in potential could change the surface anisotropy, although there is a possibility that the closer the potential comes to hydrogen evolution at  $\sim 0.80$  V, H impurities disrupt the surface states as the potential becomes more negative resulting in a lower intensity of the RAS feature. Similarly as the potential is increased to  $-0.55$  V there could be a desorption of H impurities which could lead to a more structured surface and increasing the transition intensity in the RAS profile. Previous work [41,62,63] has observed how changes in the surface anisotropy can have a large impact on the intensity of this transition. The possibility that the positive increase in the applied potential, which is expected to shift the initial surface state closer to the Fermi level, leads to a depopulation of the initial surface state is discounted since this would cause a fall in intensity of the peak. Along with the possibility that

as the potential is increased to more negative potentials H impurities could reduce the transition intensity, as the potential moves closer to the potential when  $\text{Cl}^-$  atoms adsorb, at -0.55 V there could be low levels of adsorbed  $\text{Cl}^-$  atoms. If these cause more ordered structures with larger terraces hence increasing the population of occupied initial states, an increase in intensity could be observed. A similar dependence has also been seen at the 4.34 eV peak with the peak becoming more intense as the applied potential is increased from -0.70 V to -0.55 V as shown in figure 6.17. However, at the current stage of the research there is no clear explanation for these results.

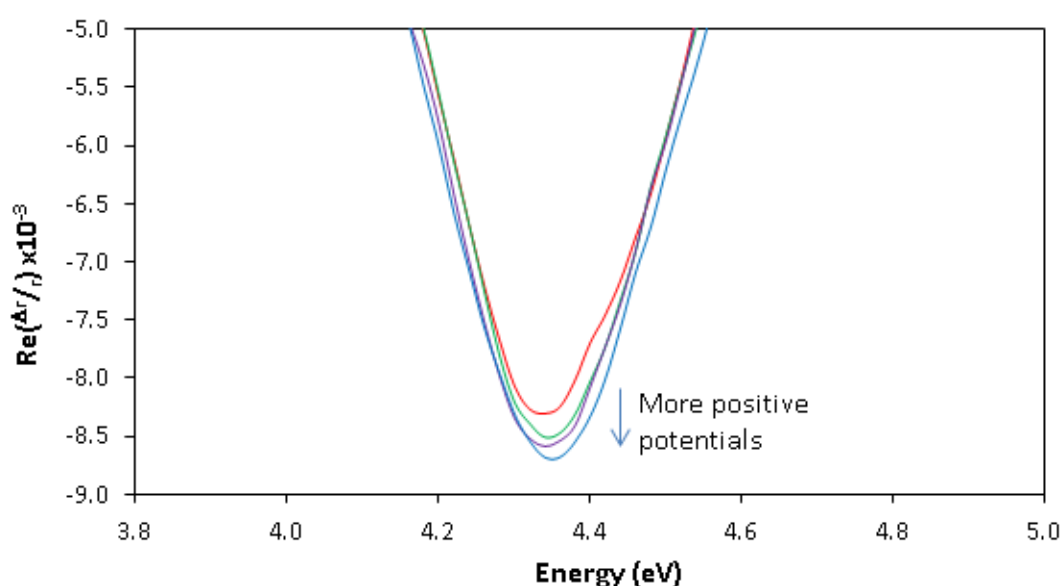
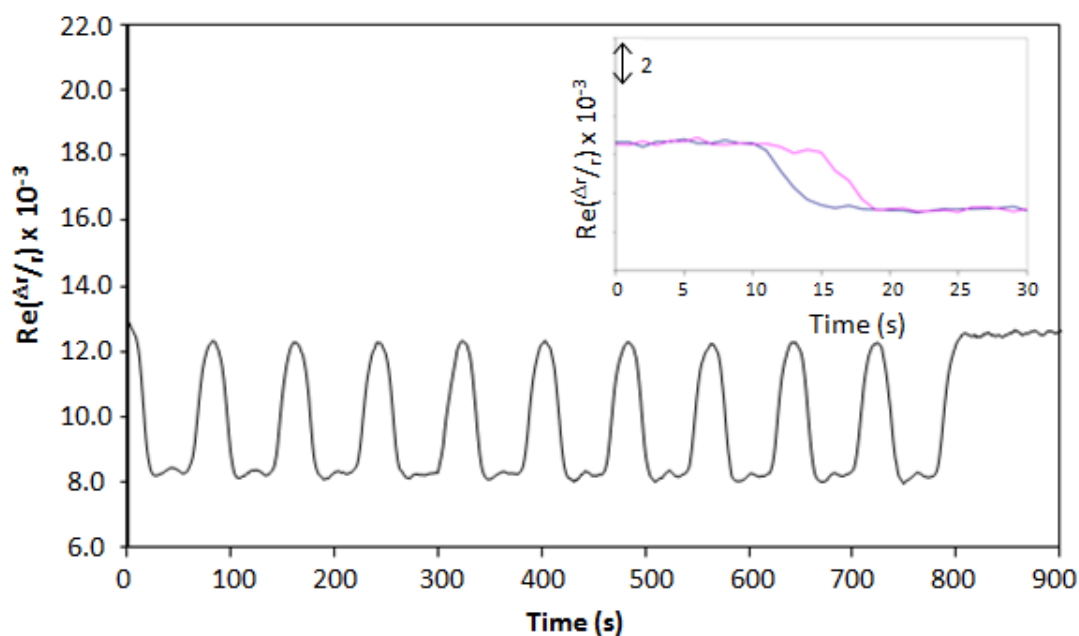


Figure 6.17: RA spectra of the Cu(110) surface in 10 mM HCl zoomed in around the 4.34 eV peak at -0.55 V (blue line), -0.60 V (purple line), -0.65 V (green line) and at -0.70 V (red line).

#### 6.6.4 Kinetic Spectra of the Cu(110) Surface using 10 mM HCl solution

Whilst performing cyclic voltammograms on the Cu(110)/HCl interface the RAS intensity can be recorded as a function of time. Figure 6.18 shows the RAS intensity as the potential is cycled ten times between -0.30 V and -0.70 V with a scan rate of  $10 \text{ mVs}^{-1}$  at an energy of 2.20 eV to coincide with the transition between surface states. The sharp peaks observed in figure 6.18 demonstrate the effect of the  $\text{Cl}^-$  atom desorbing and adsorbing onto the Cu(110) surface. There are small

fluctuations in the spectra when the potential is cycled through the  $\text{Cl}^-$  free Cu(110) surface which is in agreement with figure 6.14 which shows there is a dependence on the potential at 2.20 eV. The RAS intensity shown in figure 6.18 for the Cu(110) surface with adsorbed  $\text{Cl}^-$  atoms is the same throughout all ten cycles with a similar decrease in intensity as the potential is cycled to -0.70 V. The inset in figure 6.18 shows the RAS intensity as the potential is stepped directly from -0.35 V to -0.65 V for desorption of  $\text{Cl}^-$  atoms (blue line), or from -0.65 V to -0.35 V for the adsorption of  $\text{Cl}^-$  atoms (pink line), on the Cu(110) surface. It shows that the desorption process does not happen instantaneously but rather, over a time period of  $\sim 8$  seconds from when the potential is switched. This suggests there could be a difference in how the  $\text{Cl}^-$  atoms desorb from the different sized terraces on the electropolished Cu(110) surface. The adsorption of  $\text{Cl}^-$  atoms on the Cu(110) surface happens at a faster rate of  $\sim 4$  seconds, half the rate of desorption. This could be due to the unstable nature of the Cu(110) surface which is encouraging the adsorption of the  $\text{Cl}^-$  atoms.



**Figure 6.18:** The RAS intensity at 2.20 eV monitored as a function of time cycled between -0.30 V and -0.70 V and the inset is the comparison between the adsorption (pink line) and desorption (blue line) of  $\text{Cl}^-$  atoms on the Cu(110) surface.

## 6.7 Azimuthal Dependence Reflection Anisotropy Spectroscopy of the Cu(110)/HCl Interface

As discussed in section 3.3, RAS results obtained from an azimuthal angular variation are obtained by rotating the sample in the plane of the surface using a rotating platform which ensures the same part of the surface was observed for the full 90 ° rotation.

The RAS of the Cu(110) surface in 10 mM HCl at -0.65 V is shown in figure 6.19. The initial surface alignment is important so the principal axes of the surface are 45 ° to the plane of polarisation of the incident light resulting in a maximum intensity of the RA response. Figure 6.19 shows at  $\theta = 0^\circ$  and  $\theta = 90^\circ$  the RA spectra are at a maximum with the transition at 2.20 eV in the negative and positive direction respectively. Also, at 45 ° the RA profile is featureless which corresponds to the loss of anisotropy in the reflected light. The presence of the 2.20 eV peak when the light is incident along the [001] direction confirms the attribution of this feature to a surface state transition at the  $\bar{Y}$  point of the surface Brillouin zone. The origin of this feature has been studied extensively in UHV [41,46,62] and has been discussed in detail in section 6.4.

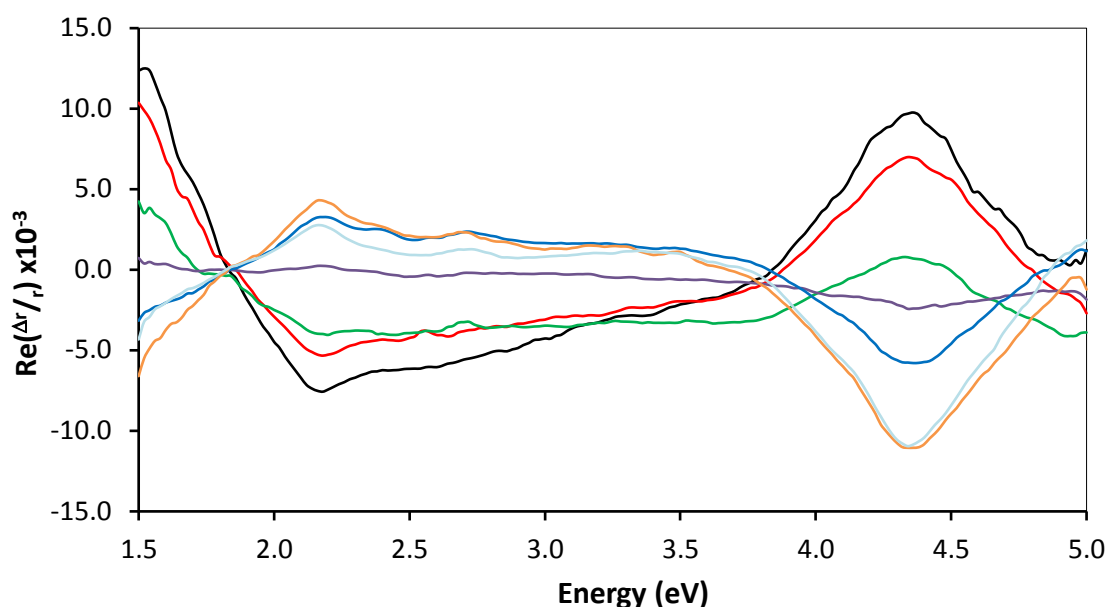


Figure 6.19: RA spectra of Cu(110) in 10 mM HCl at -0.65 V showing the angular variation at 90 ° (black line), 75 ° (red line), 60 ° (green line), 45 ° (purple line), 30 ° (blue line), 15 ° (orange line) and 0 ° (light blue line).

Figure 6.20 (a) and (b) show the variation in intensity of the peak at 2.20 eV and 4.30 eV as a function of  $\vartheta$  which follow a  $\cos 2\vartheta$  dependence as shown by the comparisons with the theoretical curve. The theoretical curve is fitted using equation 3.51 from chapter three. The difference in phase between the origins of the experimental results and theoretical curves is  $\sim 7^\circ$  which is consistent with an error in determining the origin.

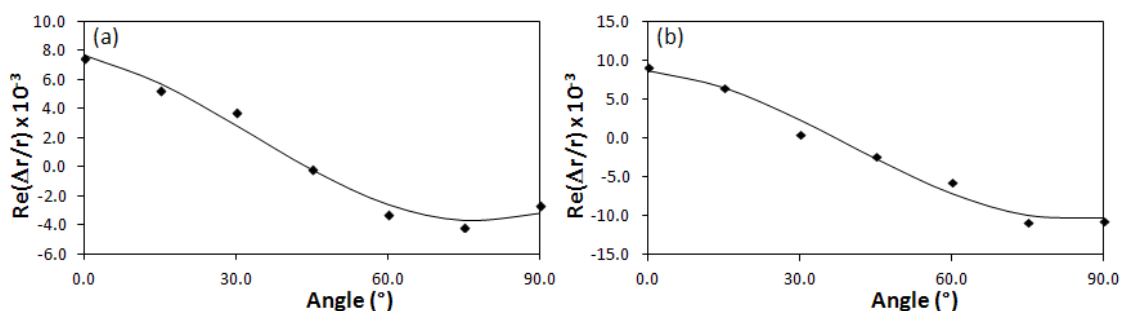


Figure 6.20: Angular dependence of RAS intensities at (a) 2.20 eV and (b) 4.30 eV comparing the experimental data points with a theoretical  $\cos 2\vartheta$  curve.



Although the spectrum at  $45^\circ$  is featureless there is a deviation from the zero line above 3.50 eV which could be explained by the difficulty in finding the exact angle when the spectrum will be at a minimum. However, there could also be weak contributions from transitions that are not orientated along one of the principal directions which would also account for this deviation away from the zero line.

Figure 6.21 shows the angular dependence of the Cu(110)/HCl interface at -0.35 V, hence when  $\text{Cl}^-$  atoms are adsorbed onto the surface. Again the spectrum collapses to the zero line at energies between 1.50 eV and 3.50 eV suggesting the dominant contributions to the RAS spectrum arise from transitions orientated along one of the principal axes, as seen at the Au(110)/liquid interface with cytosine and adenine adsorbed [17,64]. Above 3.50 eV the spectrum again deviates from the zero line implying the same cause as when the  $\text{Cl}^-$  atoms are desorbed from the surface.

The feature observed in figure 6.21 on the  $45^\circ$  line at  $\sim 2.70$  eV is the same feature as observed in figure 6.13 and its origin comes from a sharp peak in the output of the Xe lamp at this energy.

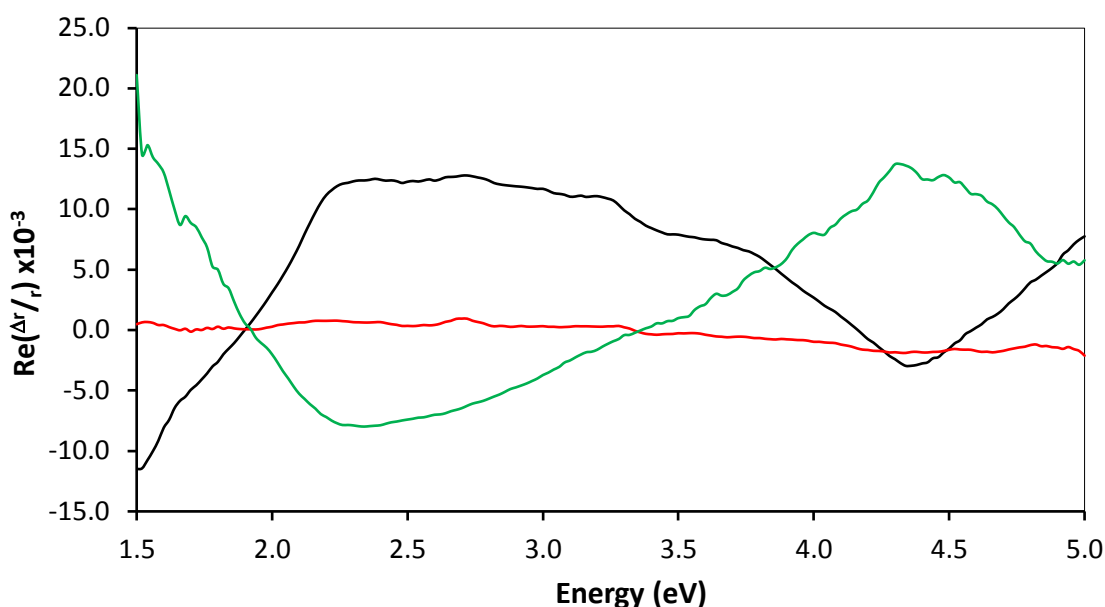


Figure 6.21: RA spectra of Cu(110) in 10 mM HCl at -0.35 V showing the angular variation at  $90^\circ$  (black line),  $45^\circ$  (red line) and  $0^\circ$  (green line).

## 6.8 Summary

This chapter has described the RAS investigations of a Cu(110) surface in a liquid environment. After describing the theory of the physical and electronic of the Cu(110) surface the experimental results in UHV have been discussed to get a thorough understanding of the surface, in particular transitions between surface states. These transitions have been studied using numerous techniques along with theoretical calculations although RAS has been used in UHV to monitor them under various conditions. This chapter has described in detail how RAS has been used to confirm the presence of these at the metal/liquid interface. Specifically the 2.20 eV peak observed in the RA spectra in a liquid environment has been assigned as a transition between surface states at the  $\bar{Y}$  point of the surface Brillouin zone. The chapter has also described the sensitivity of the surface states to contamination, in particular the presence of  $\text{Cl}^-$  atoms on the surface which can then be removed using electrochemistry. Furthermore the chapter has shown the results of azimuthal dependent RAS experiments which show the Cu(110) surface follows a

$\cos^2\theta$  and the dependence of the 2.20 eV feature on the polarisation of the incident light which further confirms the feature as a surface state.

## 6.9 References

- [1] Almond, N., *Ph. D. Thesis*. The University of Liverpool. (2008)
- [2] Ertl, G., *Surf. Sci.* **6** (1967) 208
- [3] Habraken, F. H. P. M. and Bootsma, G. A., *Surf. Sci.* **87** (1979) 333
- [4] Courths, R., Cord, B., Wern, H., Saalfeld, H. and Hüfner, S., *Solid. State. Commun.* **63** (1987) 619
- [5] Tsukahara, N., Noto, K., Ohara, M., Shiraki, S., Takagi, N., Takata, Y., Miyawaki, J., Taguchi, M., Chainani, A., Shin, S. and Kawai, M., *Phys. Rev. Lett.* **102** (2009) 167203
- [6] Spitzer, A. and Lüth, H., *Surf. Sci.* **118** (1982) 121
- [7] DiDo, R. A., Zehner, D. M. and Plummer, E. W., *J. Vac. Sci. Technol. A.* **2** (1984) 852
- [8] Jacob, W., Dose, V. and Goldmann, A., *Appl. Phys. A.* **41** (1986) 145
- [9] Chen, C. T. and Smith, N. V., *Phys. Rev. B.* **40** (1989) 7487
- [10] Tjeng, L. H., Meinders, M. B. J. and Sawatzky, G. A., *Surf. Sci.* **233** (1990) 163
- [11] Jacobsen, K. W. and Nørskov, J. K., *Phys. Rev. Lett.* **65** (1990) 1788
- [12] Zeppenfeld, P., Kern, K., David, R. and Comsa, G., *Phys. Rev. Lett.* **62** (1989) 63
- [13] Mochrie, S. G. J., *Phys. Rev. Lett.* **59** (1987) 304
- [14] Zeppenfeld, P., Kern, K., David, R., Kuhnke, K. and Comsa, G., *Phys. Rev. B.* **38** (1988) 12329
- [15] Dürr, H., Schneider, R. and Fauster, Th., *Phys. Rev. B.* **43** (1991) 12187

- [16] Häkkinen, H., Merikoski, J., Manninen, M., Timonen, J. and Kaski, K., *Phys. Rev. Lett.* **70** (1993) 2451
- [17] Kofman, R., Cheyssac, P. and Richard, J., *Surf. Sci.* **77** (1978) 537
- [18] Kresse, G. and Furthmüller, J., *Comp. Mater. Sci.* **6** (1996) 15
- [19] Kresse, G. and Hafner, J., *Phys. Rev. B.* **49** (1994) 14251
- [20] Marder, M. P., Condensed Matter Physics, Second Edition. (John Wiley & Sons Inc, Hoboken) 2010
- [21] Cord, B., Courths, R. and Wern, H., *Phys. Rev. B.* **31** (1985) 1164
- [22] Straube, P., Pforte, F., Michalke, T., Berge, K., Gerlach, A. and Goldmann, A., *Phys. Rev. B.* **61** (2000) 14072
- [23] Goldmann, A., Dose, V. and Borstel, G., *Phys. Rev. B.* **32** (1985) 1971
- [24] Bartynski, R. A., Gustafsson, T. and Soven, P., *Phys. Rev. B.* **31** (1985) 4745
- [25] Jiang, M. Y., Pajer, G. and Burstein, E., *Surf. Sci.* **242** (1991) 306
- [26] Bertel, E., *Surf. Sci.* **331-333** (1995) 1136
- [27] Weightman, P., Martin, D. S., Cole, R. J. and Farrell, T., *Rep. Prog. Phys.* **68** (2005) 1251
- [28] Hofmann, Ph., Rose, K. C., Fernandez, V., Bradshaw, A. M. and Richter, W., *Phys. Rev. Lett.* **75** (1995) 2039
- [29] Woll, J., Meister, G., Barjenbruch, U. and Goldmann, A., *Appl. Phys. A.* **60** (1995) 173
- [30] Martin, D. S., Maunder, A. and Weightman, P., *Phys. Rev. B.* **63** (2001) 115403
- [31] Martin, D. S., Cole, R. J. and Haq, S., *Phys. Rev. B.* **66** (2002) 155427

- [32] Sun, L. D., Hohage, M., Zeppenfeld, P. and Balderas-Navarro, R. E., *Surf. Sci.* **589** (2005) 153
- [33] Sun, L. D., Hohage, M., Zeppenfeld, P., Balderas-Navarro, R. E. and Hingerl, K., **527** (2003) L184
- [34] Monachesi, P., Palummo, M., Del Sole, R., Ahuja, R. and Eriksson, O., *Phys. Rev. B.* **64** (2001) 115421
- [35] Baumberger, F., Herrmann, Th., Kara, A., Stolbov, S., Esser, N., Rahman, T. S., Osterwalder, J., Richter, W. and Greber, T., *Phys. Rev. Lett.* **90** (2003) 177402
- [36] Ditlevsen, P. D., Stoltze, P. and Nørskov, J. K., *Phys. Rev. B.* **44** (1991) 13002
- [37] Tarriba, J. and Luis Mochán, W., *Phys. Rev. B* **46** (1992) 12902
- [38] Hansen, J. –K., Bremer, J. and Hunderi, O., *Surf. Sci.* **418** (1998) L58
- [39] Stahrenberg, K., Hermann, Th., Esser, N. and Richter, W., *Phys. Rev. B.* **61** (2000) 3043
- [40] Jacob, W., Dose, V., Kolac, U., Fauster, Th. and Goldmann, A., *Z. Phys. B – Condensed Matter.* **63** (1986) 459
- [41] Sun, L. D., Hohage, M., Zeppenfeld, P., Balderas-Navarro, R. E. and Hingerl, K., *Phys. Rev. Lett.* **90** (2003) 106104
- [42] Frederick, B. G., Cole, R. J., Power, J. R., Perry, C. C., Chen, Q., Richardson, N. V., Weightman, P., Verdozzi, C., Jennison, D. R., Schultz, A. and Sears, M. P., *Phys. Rev. B.* **58** (1998) 10883
- [43] Isted, G. E. and Martin, D. S., *Appl. Surf. Sci.* **252** (2005) 1883
- [44] Henderson, D. and Boda, D., *Phys. Chem. Chem. Phys.* **11** (2009) 3822

- [45] Taylor, C. D., Wasileski, S. A., Filhol, J. –S. and Neurock, M., *Phys. Rev. B.* **73** (2006) 165402
- [46] Kolb, D. M., Boeck, W., Ho, K. –M. and Liu, S. H., *Phys. Rev. Lett.* **47** (1981) 1921
- [47] Boeck, W. and Kolb, D. M., *Surf. Sci.* **118** (1982) 613
- [48] Franke, C., Piazza, G. and Kolb, D. M., *Electrochimica Acta.* **34** (1989) 67
- [49] Ho, K. –M., Fu, C. –L., Lui, S. H., Kolb, D. M. and Piazza, G., *J. Electroanal. Chem.* **150** (1983) 235
- [50] Mazine, V., Borensztein, Y., Cagnon, L. and Allongue, P., *phys. stat. sol. (a)* **175** (1999) 311
- [51] Sheridan, B., Martin, D. S., Power, J. R., Barrett, S. D., Smith, C. I., Lucas, C. A., Nichols, R. J. and Weightman, P., *Phys. Rev. Lett.* **85** (2000) 4618
- [52] Smith, C. I., Maunder, A. J., Lucas, C. A., Nichols, R. J. and Weightman, P., *J. Electrochem. Soc.* **150** (2003) E233
- [53] Mansley, C. P., Smith, C. I., Cuquerella, M. C., Farrell, T., Fernig, D. G., Edwards, C. and Weightman, P., *phys. stat. sol. (c)* **5** (2008) 2582
- [54] Weightman, P., Dolan, G. J., Smith, C. I., Cuquerella, M. C., Almond, N. J., Farrell, T., Fernig, D. G., Edwards, C. and Martin, D. S., *Phys. Rev. Lett.* **96** (2006) 086102
- [55] Foresti, M. L., Pezzatini, G. and Innocenti, M., *J. Electroanal. Chem.* **434** (1997) 191
- [56] Andersson, K., Ketteler, G., Bluhm, H., Yamamoto, S., Ogasawara, H., Pettersson, L. G. M., Salmeron, M. and Nilsson, A., *J. Phys. Chem. C.* **111** (2007) 14493

- [57] Obliers, B., Anastasescu, A., Broekmann, P. and Wandelt, K., *Surf. Sci.* **573** (2004) 47
- [58] Barritt, E. E., Smith, C. I., Martin, D. S., Gentz, K., Wandelt, K. and Weightman, P., *EPL*. **92** (2010) 57005
- [59] Gentz, K. and Wandelt, K., unpublished
- [60] Kotz, R. and Kolb, D. M., *Z. Phys.* **112** (1978) 69
- [61] Ho, K. -M., Harmon, B. N. and Liu, S. H., *Phys. Rev. Lett.* **44** (1980) 1531
- [62] Weightman, P., *Surf. Sci.* **602** (2008) 1729
- [63] Sun, L. D., Denk, R., Hohage, M. and Zeppenfeld, P., *Surf. Sci.* **602** (2008) L1
- [64] Mansley, C. P., Smith, C. I., Bowfield, A., Fernig, D. G., Edwards, C. and Weightman, P., *J. Chem. Phys.* **132** (2010) 214708



## **Chapter 7**

## **Conclusions**

## 7.1 Conclusions

Since this thesis contains three fairly individual chapters, the key findings of the research will be discussed individually for each chapter.

### 7.1.1 Conclusions on Si(110)

The chapter begins by discussing the physical and electronic structure of the Si(110) surface from studies reported from previous research before summarising ellipsometry measurements showing the complex dielectric function of the Si(110) surface. The peaks in the spectra can be attributed to transitions in the electronic structure of silicon. The dependence of the peak energy with increasing temperature was then discussed along with calculations for the temperature coefficients at the transitions.

The RA spectra for the  $Re\left(\frac{\Delta r}{r}\right)$  part of the Si(110) surface in air is then presented which shows two main features at the same energies for the peaks observed in ellipsometry measurements which have been attributed to transitions  $E_1$  and  $E_2$ , at 3.52 eV and 4.36 eV respectively. The dependence of the peak energy with increasing temperatures up to 623 K is then studied and the temperature coefficients calculated for  $E_1$  and  $E_2$ . These temperature coefficients for  $E_1$  and  $E_2$  show good agreement for the values shown using ellipsometry measurements.

The chapter then presents data for the  $Im\left(\frac{\Delta r}{r}\right)$  part of the RA spectra, which has a different profile to the  $Re\left(\frac{\Delta r}{r}\right)$  spectra. However, the features observed have similar energies to previous results and the temperature dependence of the peak energy show good agreement to transitions  $E_1$  and  $E_2$  at  $\sim 3.40$  eV and  $\sim 4.50$  eV respectively.

Finally the chapter discusses the complex surface dielectric function. Since both the  $Re\left(\frac{\Delta r}{r}\right)$  and  $Im\left(\frac{\Delta r}{r}\right)$  parts of the RA spectra have been measured, by using

previous data for the bulk complex dielectric function, it is possible to determine the complex surface dielectric function at various temperatures. The spectra can then be plotted for the real and imaginary parts of the function which again show features at similar energies to those observed previously. The temperature coefficients are then calculated and compared to those for the bulk dielectric function and for transitions  $E_1$  and  $E_2$  show good agreement.

### 7.1.2 Conclusions on Ag(110)

In a similar way to the previous section, this chapter begins by giving a brief historical overview of the current understanding of the properties of the Ag(110) surface. This focused particularly on the thermodynamics of the Ag(110) surface and the ability to predict the temperature at which the oxide will dissociate from the Ag(110) surface using Ellingham diagrams. This will aid the understanding of the results later on in the chapter. All experiments presented in this chapter are performed in air and therefore the temperature at which the oxide will dissociate is at  $\sim 380$  K.

Previous studies on the Ag(110) surface have been performed under UHV conditions and have focused on energies around the plasmon resonance energy at  $\sim 3.90$  eV. This is where the majority of the features observed have been present. There is a further feature at 1.70 eV in the RA spectra in UHV which has been attributed to a transition between surface states at the  $\bar{Y}$  point of the surface Brillouin zone although it has a much lower intensity than the features around 3.90 eV. At this energy, the azimuthal dependence of the Ag(110) surface also changes from a  $\cos 2\vartheta$  dependence to a  $\sin 4\vartheta$  dependence.

The chapter then presents data for the  $Re\left(\frac{\Delta r}{r}\right)$  part of the RA spectra at temperatures of 293 K and 623 K along with the spectra showing how the peak position changes with increasing temperature. Data is also presented when the Ag(110) surface is heated at different rates although this has been observed to have a negligible effect.

The  $Im\left(\frac{\Delta r}{r}\right)$  part of the RA spectra is also presented along with how the spectrum varies with temperature. Here, two distinct regions are present when observing how the peak energy behaves with increasing temperature. The first region is before the temperature at which the oxide will dissociate from the Ag(110) and the second region is after this temperature. The temperature gradient after the oxide dissociation temperature shows good agreement with the temperature gradients determined from the  $Re\left(\frac{\Delta r}{r}\right)$  part of the RA spectrum which could imply the  $Im\left(\frac{\Delta r}{r}\right)$  part of the RA spectrum is more sensitive to oxide coverage.

The chapter ends with a discussion on the azimuthal dependence of the  $Re\left(\frac{\Delta r}{r}\right)$  part of the RA spectra at  $\sim 3.90$  eV in air at 523 K. Although this research does not observe a  $\sin 4\theta$  dependence, there is a phase change of  $180^\circ$  at 3.86 eV which has also been observed in UHV.

### 7.1.3 Conclusions on Cu(110)

Again this chapter begins with a discussion on the previous experiments on the Cu(110) surface in UHV environments. This precedes a description of how RAS has been able to monitor transitions between surface states and a brief section showing how these transitions are extremely sensitive to contamination.

The RA profile of the Cu(110) surface is well understood in UHV and contains two main features, one at 2.10 eV which has been attributed to a transition between surface states at the  $\bar{Y}$  point of the surface Brillouin zone and a second at  $\sim 4.3$  eV which has been attributed to transitions around the L point of the Brillouin zone and is sensitive to surface morphology.

Results are then presented for the Cu(110)/liquid interface using  $H_2O$  and  $H_2SO_4$  solutions. These showed reasonable agreement with the RA spectra from previous results although the surface was not stable. The chapter then presents the RA profile when using a bromide based electrolyte which did not show good

agreement as it was found that the bromide ions adsorb too strongly to the Cu(110) surface and quench the transition between surface states. Therefore a chloride based electrolyte was used for the remainder of the research in this chapter.

Using electrochemistry, the adsorption and desorption of the chloride ions on the surface can be manipulated using different applied potentials. Therefore, there is a region between -0.55 V vs Ag/AgCl and -0.70 V vs Ag/AgCl where the chloride ions will not be adsorbed on the surface. In this potential range there is a peak at 2.20 eV in the RA spectra which possesses a similar line width to the peak attributed to the transition between surface states at the  $\bar{Y}$  point of the surface Brillouin zone. This peak is not observed at potentials outside this range showing that it is sensitive to surface contamination. Therefore, in this research the peak at 2.20 eV has been attributed to a transition between surface states showing that although surface states are highly sensitive to contamination, it is possible to observe them outside a UHV environment.

## 7.2 Future Work

Since this research presents data from three different materials, the scope for further work is wide ranging. In particular, continuing to present data for the  $Im\left(\frac{\Delta r}{r}\right)$  part of the RA spectra alongside the data for the  $Re\left(\frac{\Delta r}{r}\right)$  part of the RA spectra will help to develop the understanding of optical processes. It would also be interesting to try and simulate the RA data published in this thesis using the derivative model which has been used in previous experiments. Similarly to compare the RA spectrum produced to the 'derivative-like' lineshape and 'dielectric-function-like' lineshapes which have shown some comparisons between the real and imaginary parts of the RA spectrum

As discussed in chapter 5 one of the most obvious areas to progress would be to produce some XPS data for the Ag(110) surface around the temperature at which

the oxide dissociates from the surface. This would give conclusive evidence to the assumption that the thermodynamic behaviour of the system based around the Ellingham diagrams is correct which would strongly improve the research.

The investigations into the Cu(110)/liquid interface provided many challenges experimentally, such as the preparation of the Cu(110) surface. Preparing the Cu(110) surface in a UHV environment enabled a clean Cu(110) surface to be present. As shown in the LEED pattern in figure 7.1.

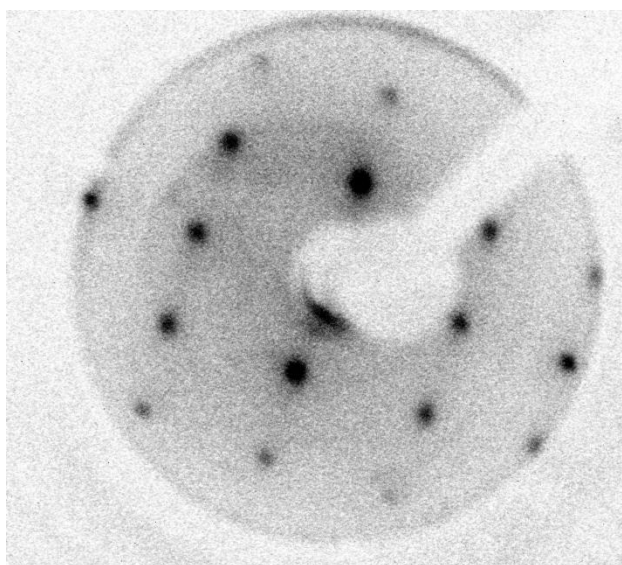


**Figure 7.4: LEED pattern of the Cu(110) surface in a UHV environment.**

Currently the UHV set up does not include a chamber in which the Cu(110) surface can be easily transferred into the electrochemical cell which meant the surface is electropolished before experiments take place. If the UHV chamber can be upgraded to include a chamber in which the crystal could be set up in the electrochemical cell and experiments could be performed immediately this could result in the peak observed at 2.20 eV increasing to an intensity more comparable to that observed from the 2.10 eV peak in UHV. This is due to the electropolishing technique causing terraces on the Cu(110) surface which, by removing the electropolishing technique, should not be present. This will result in a higher

number of transitions between the surface states which, as a consequence, would lead to an increase in the RA intensity at 2.20 eV.

# Publications

Evidence for the observation of surface states at the Cu(110)/electrolyte surface

E. E. Barritt, C. I. Smith, D. S. Martin, K. Gentz, K. Wandelt and P. Weightman, *EPL* **92** (2010) 57005

Optical response of the Cu(110)/electrolyte interface

E. E. Barritt, C. I. Smith, D. S. Martin, K. Gentz, K. Wandelt and P. Weightman, *J. Phys.: Conf. Ser.* **286** (2011) 012028